Faculdade de Engenharia da Universidade do Porto

Antenna Design for Integration into Active Devices Targeting 5G and Beyond

Hugo Miguel Guedes Pereira dos Santos

MAP-tele Doctoral Programme in Telecommunications

Supervisor: Henrique M. C. F. Salgado

Co-supervisor: Pedro Renato Tavares Pinho

July 30, 2020

Thesis Identification

Title:	Antennas for Integration on Devices Targeting 5G and Beyond
Keywords:	System-in-Package, 5G, IoT, Miniaturized Antennas, Sub-THz Antennas, mmWave Antennas.
Start:	October 2016
Expected duration:	3 years
Candidate Information:	
Name:	Hugo Miguel Guedes Pereira dos Santos
e-mail:	hugo.m.santos@inesctec.pt
Supervisor Information:	
Name:	Henrique M. C. F. Salgado Associate Professor, FEUP Senior Researcher, INESC TEC http://oet.inesctec.pt/
e-mail:	hsalgado@fe.up.pt
Co-supervisor information:	
Name:	Pedro Renato Tavares Pinho Assistant Professor, ISEL Senior Researcher, IT Aveiro https://www.it.pt/Members/Index/470
e-mail:	ptpinho@av.it.pt
Educational institution	Faculdade de Engenharia da Universidade do Porto
Host institution:	INESC TEC

Resumo

Os tamanhos típicos de antenas representam frações consideráveis do comprimento de onda a que estas operam. No caso de cornetas e agrupamentos de antenas as dimensões podem chegar a dezenas ou até centenas de comprimentos de onda. Este efeito leva a uma contrariedade perante a tendência natural de reduzir os tamanhos de componentes electrónicos, uma vez que a redução do tamanho dos elementos radiantes nem sempre acompanhou a redução dos dispositivos activos. A solução típica para inteconexão entre antenas e dispositivos activos passa por usar uma PCB, onde tipicamente se projeta a antena e se efetua as ligações aos ICs. No entanto, é imediato perceber que esta solução acarreta o uso de áreas maiores comparativamente ao caso em que as antenas fossem integradas directamente no encapsulamento dos ICs. Esta última solução permite reduzir custos reduzindo a área, mas também libertar espaço na PCB para novas funcionalidades associadas aos ICs.

O foco principal desta tese é desenvolver topologias de antenas para IoT (Bluetooth Low Energy), 5G NR (banda K), banda W e sub-THz, considerando a sua integração directa com os dispositivos activos através do encapsulamento, seja este em tecnologias compactas como eWLB ou em tecnologias mais volumosas como split-block. Estas topologias são desenvolvidas recorrendo a modelação numérica e simulações electromagnéticas 3D utilizando método dos momentos (MoM) e o método de elementos finitos (FEM). Adicionalmente validam-se também as antenas propostas fabricando-as e medindo em ambientes apropriados como câmaras anecoicas.

O trabalho desenvolvido nesta tese poderá potenciar novas abordagens nos mercados IoT, automóvel e de comunicações móveis, uma vez que a possibilidade de ter diferentes tecnologias integradas com passivos e as antenas é, hoje em dia, uma realidade.

Abstract

Antenna sizes are usually considerable fractions of their operating wavelength. In the case of horn antennas and arrays they can span for multiple wavelengths. Such leads to a noticeable mismatch between the natural trend of size reduction seen in the IC industry and the size of antennas. The typical solution is to interconnect integrated circuits and antennas in the PCB. Nonetheless, since larger area and volume usually implies higher costs, the effort of reducing antenna sizes to packaging size scale will be largely appreciated by consumer electronics companies.

The main focus of this PhD thesis is to develop antenna topologies for IoT (Bluetooth Low Energy), 5G NR (K-band), W-band and sub-THz, considering their integration with active devices in either small packages or large encapsulations such as split-block waveguides. Such development is carried out by resorting to numerical modelling and 3D electromagnetic simulations using method of moments (MoM) and Finite-Element Method (FEM). Additional validation is done by developing proper test setups and effectively measuring the antennas in reflection free environments such as anechoic chambers.

The work developed in this thesis can break new ground for IoT, automotive and mobile communications markets, since the possibility of having the antennas fully integrated with active devices in different packaging technologies is becoming a reality.

Acknowledgements

Hoping that no one is left behind, I would like to give special thanks to

> Professor Henrique Salgado for supervising this PhD and contributing with his excellent theoretical and experimental support.
>
> Professor Pedro Pinho for co-supervising this work and asking the difficult questions that made me think twice on the technical approaches I was following.
>
> all my family, specially to my parents Henrique and Aurora that have been my base of support and comfort my whole life.
>
> my best friend that I am lucky to also have as my wife Marina for being with me in the most difficult moments and giving me motivation to carry on.
>
> INESC TEC for providing the needed financial and technical resources.
>
> my friends Rui Maia and Bianca Silva for their friendship, good times and vacations that allowed me to rest my mind and keep pursuing my PhD.
>
> my INESC TEC and FEUP colleagues that somehow, either by their technical help or unique friendship, helped me achieving my objectives: Erick Lima, Francisco Pimenta, Henrique Rocha, Joana Tavares, Rafael Kraemer, Diogo Moreira, Bruno Correia, João Araújo, Luis Pessoa, Mário Lopes, Filipe Teixeira and Carlos Leocádio.
>
> the lab technicians from the Electrical Engineering Department Carlos Graf and Rui Fernandes for supporting my work with their friendship, availability and technical expertise.
>
> last but not least I would like to thank FCT for funding this PhD through the scolarship PD/BD/128197/2016.

Hugo Santos

"Invention is the most important product of man's creative brain. The ultimate purpose is the complete mastery of mind over the material world, the harnessing of human nature to human needs."

Nikola Tesla

Contents

List of Figures

List of Tables

Abbreviations

ADS	Advanced Design System
AUT	Antenna Under Test
BCB	Benzocyclobutene
BLE	Bluetooth Low energy
CBCPW	Conductor Backed Coplanar Waveguide
CNC	Computer Numeric Control
CPW	Coplanar Waveguide
EM	Electromagnetic
ESA	Electrically Small Antenna
FEM	Finite Element Method
FNBW	First-Null Beamwidth
FTBR	Front-to-Back Ratio
GO	Geometrical Optics
GSG	Ground-signal-ground
HFSS	High Frequency Structure Simulator
HPBW	Half-Power Beamwidth
IC	Integrated Circuit
IEEE	Institute of Electrical and Electronics Engineers
IoT	Internet-of-Things
ISM	Industrial, Scientific and Medical
LHCP	Left-Hand Circularly Polarized
LTCC	Low Temperature Co-fired Ceramic
MC	Mold Compound
MIMO	Multiple Input Multiple Output
MoM	Method of Moments
NR	New Radio
OOK	On-Off Keying
PCB	Printed Circuit Board
PI	Polyimide
PO	Physical Optics
PSO	Particle Swarm Optimizer
RDL	Redistribution Layer
RF	Radio Frequency
RHCP	Right-Hand Circularly Polarized
RTD	Resonant Tunnelling Diode
SiP	System-in-Package
SIW	Substrate Integrated Waveguide
SLL	Sidelobe Level

SoC	System-on-Chip
SOLT	Short Open Load Through
TEM	Transverse Electromagnetic
TE	Transverse Electric
TM	Transverse Magnetic
TRL	Through Reflect Line
UBM	Under-bump Metallization
UTD	Uniform Theory of Diffraction
VSWR	Voltage Standing Wave Ratio

Chapter 1

Introduction

1.1 Motivation

The increasing demand of fast, small and energy efficient devices has pushed the scientific community into providing solutions to the recurring problems of crossing the forth generation communication boundaries into future generations. Large scale integration and interconnectivity of electronic devices, such as system-in-package (SiP) has been the enabler of most technologies we know nowadays such as cell phones, wireless routers, radars, electro-optical transceivers, computer processors, mobile base-stations, among others [1–3]. However, antenna technology did not totally keep up with such integration and size reduction of most electronic devices.

Most of our well known communication devices such as Bluetooth and Wi-Fi operate at the 2.4 GHz ISM band. Since Bluetooth has been one of the most used technologies for IoT [4], it became a requirement to have Bluetooth devices as small as possible. Nonetheless a quarter wavelength at this frequency is approximately 30 mm, which is not suitable for integration with a small scale system-on-chip (SoC). Therefore, in this frequency band, very strong miniaturization efforts are needed to enable the integration of antennas with Bluetooth SoCs, since the antenna becomes a fraction of the wavelength. Some applications of this technology require that not only the radiating element is reduced, but also the ground-plane of the antenna.

In the European 5G the band n258 (commonly known as K-band) is one of the proposed frequency bands that range from 24.25 to 27.5 GHz [5]. In this band the integration of antennas and their driving integrated circuits (ICs) is of paramount importance. The size of the patch arrays altogether with their feeding and matching circuits are approximately of the same size as a typical package of approximately 10×10 mm [6, 7]. This is an advantage as no miniaturization efforts are needed to have an antenna array integrated in a package at these frequencies. However, the package height is limited and shall be kept to a minimum given the trend in mobile device body thickness shown in Fig. 1.1. Given the wide bandwidth needed for 5G K-band communications [8] and the fact that the bandwidth of patch antennas can be increased by using thicker substrates, this height limitation poses a serious challenge for the design of patch antennas in this technology.

At the lower part of the W-band ($75 - 79$ GHz) directive antennas such as series-fed patch

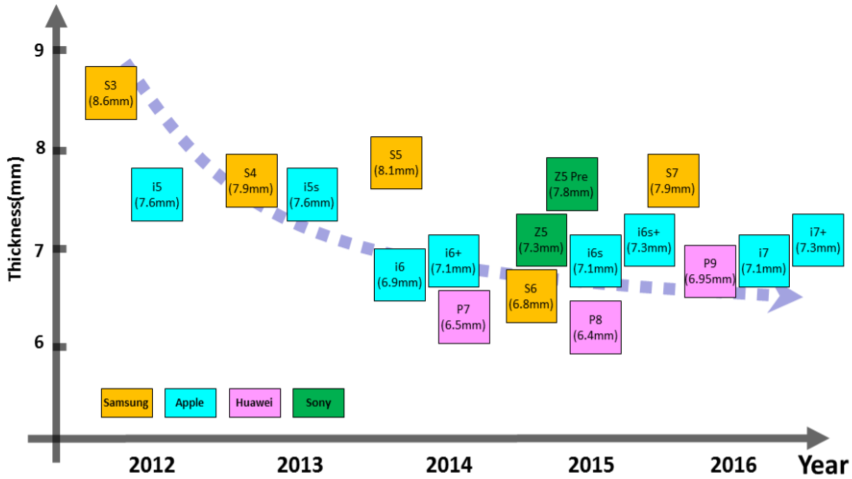

Figure 1.1: Body thickness of popular mobile phones in past 5 years, [3].

arrays can be designed in a compact size. Therefore, as it is the case of K-band antennas, no miniaturization efforts are needed. Furthermore, the package height ceases to be a limitation, as the frequency is high enough for fulfilling the bandwidth requirements of the most typical applications as in the case of automotive radar. Nonetheless, because of the higher frequency, other problems arise such as surface waves, radiation from transmission lines and increased coupling between antenna elements in the array [9]. Because of this, low cost single-layer designs require larger efforts to avoid increased sidelobes and efficiency losses.

G-band communications between 110 and 300 GHz have a high potential for beyond 5G candidates, given the bit rates in the order of tens of Gb/s they are able to provide with the most simple modulations. Albeit their capabilities to achieve high data throughputs, the efficiency of transmitter devices is still low. Additionally, given the high-frequency of operation, the antennas are typically designed on the chip itself to avoid additional parasitics and losses. As the substrates used for these ICs have high permittivities, this results in substrate modes that are guided when antennas are designed on top of them and contribute to a reduced radiation efficiency and deformations on the radiation pattern [10]. Another popular way is the direct integration of G-band devices with waveguide-fed antennas such as horns, when high directivity is required [11].

1.2 Work Objectives

Considering the issues and gaps in the state-of-the-art presented in the previous section, the high level objective is to develop antenna topologies that are able to circumvent the challenges of integration with active devices, namely:

- a S band miniaturized antenna for Bluetooth capable of being integrated in a system-in-package which has the dimensions of 12.6×7.5 mm

- a K band patch antenna for 5G NR capable of supporting polarization diversity with a package height not exceeding 1.5 mm

- a W band series fed antenna array for automotive radar operating in the range from 75 to 79 GHz with no beam squint

- a millimetre wave (300 GHz) on-chip monopole in indium phosphide substrate technology with air side radiation

- a high gaussicity horn antenna that covers the whole WR-3 frequency band

1.3 Author's Contributions

The main contributions of this PhD are summarized below:

- Miniaturization method for a Bluetooth Low Energy meander-line antenna based in the combination of three miniaturization techniques, namely: meander traces, inductive loading and magnetic coupling;

- A high isolation patch topology for European 5G NR communications in K-band (24.25 – 27.5 GHz), together with heuristic based matching networks and parasitic elements for bandwidth improvement;

- A differential feeding method to achieve zero beam squint in series-fed patch arrays;

- An on-chip antenna topology based on elliptical disk monopoles for mitigating substrate modes, radiation pattern perturbations and achieving air-side radiation at sub-THz frequencies;

- A spline-profile for split-block diagonal horn antennas capable of achieving broadband gaussicity, better SLL and XPD than conventional horns;

- A frequency and gain scalability and design methodology based on two closed-form expressions for the aforementioned spline-profiled horn;

- A physical optics based method for designing cost efficient anechoic chambers and determining their quiet zones at millimetre wave frequencies;

- An open waveguide based method for characterization of RF absorbers at millimetre wave frequencies, with complex waveguide flange geometries.

The following papers resulting from this thesis are either published, accepted, under review or in preparation for submission:

- Journals and Magazines:

- H. Santos, P. Pinho, R. P. Silva, M. Pinheiro and H. M. Salgado, "Meander-Line Monopole Antenna With Compact Ground-Plane for a Bluetooth System-In-Package", in *IEEE Antennas and Wireless Propagation Letters*. (Published);
- P. Pinho, H. M. Santos, H. M. Salgado, "Design of an Anechoic Chamber for W-Band and mmWave", in *MDPI Sensors*. (Under review);
- H. M. Santos, P. Pinho, H. M. Salgado "Zero Beam Squint Differential Series-Fed Array for Automotive Radar Applications on W Band", in *IEEE Transactions on Antennas and Propagation*. (Preparation for submission);

• Conferences:

- A. Martins et al.,"Low-Density Fan-Out SiP for Wearables and IoT with Heterogeneous Integration", *2018 International Wafer Level Packaging Conference (IWLPC)*, San Jose, CA, 2018, pp. 1-6. (Published);
- A. Martins et al., "Heterogeneous Integration Challenges Within Wafer Level Fan-Out SiP for Wearables and IoT", *2018 IEEE 68th Electronic Components and Technology Conference (ECTC)*, San Diego, CA, 2018, pp. 1485-1492. (Published);
- H. M. Santos, P. Pinho, H. M. Salgado, "Dual-Polarized Patch Antenna-in-Package with High Isolation for Ka-Band 5G Communications", *2019 International Microwave and Optoelectronics Conference (IMOC)*, Aveiro, 2019. (Accepted);
- H. M. Santos, L. M. Pessoa, P. Pinho, H. M. Salgado, "Elliptical Monopole Antenna on InP Substrate for Sub-THz RTD-based Oscillators", *2018 IEEE International Symposium on Antennas and Propagation & USNC/URSI National Radio Science Meeting*, Boston, MA, 2018, pp. 801-802. (Published);
- H. M. Santos et al., "Scalable High-Gaussicity Split-Block Diagonal Horn Antenna for Integration with Sub-THz Devices", *2019 49th European Microwave Conference (EuMC)*, Paris, 2019. (Accepted).

• Others:

- Submitted patent request "Split-block Diagonal Horn Antenna and Manufacture Method Thereof"
- Registered software for the calculation of the geometry of a spline profiled split-block horn antenna for any frequency and gain

1.4 Document Structure

This PhD thesis is organized in nine chapters. This chapter presents the motivation, contributions and structure of this work, chapter 2 provides the fundamentals on antennas needed for the comprehension of this thesis. Chapter 3 shows the design methodology of a miniaturized Bluetooth Low Energy antenna-in-package, using a combination of three miniaturization techniques.

In chapter 4 a dual-polarized patch antenna with high isolation for 5G NR communications in K-band is shown, where an novel matching topology is shown along with parasitic elements on the antenna. In chapter 5 a zero beam squint series-fed array is shown, using a differential feeding of the array itself to improve pattern stability. Chapter 6 shows the design of an elliptical monopole on-chip antenna in indium phosphide, where air-side radiation is obtained by substrate and antenna shaping. In chapter 7 a spline-profiled horn is described where high gaussicities are obtained in the full WR-3 bandwidth. A scalability analysis and design methodology for these horns is also presented. Chapter 8 describes the design of an anechoic chamber for millimetre wave using physical optics. A method for dielectric characterisation is also described. Finally, in chapter 9 the final conclusions and future work guidelines are presented.

Chapter 2

Antenna Fundamentals

2.1 Introduction

An antenna element is a transducer that converts electrical energy in free-space electromagnetic waves and vice-versa. As any other transducer, it is possible to define certain parameters such as directivity, efficiency, among others. In this section a general basis is given for understanding the antenna concepts that will follow in the next chapters. The concepts and rationales presented in this section closely follow the work of Balanis, in which the fundamental parameters of antennas are addressed [12].

2.2 Radiation Mechanism

Radiation may take place from a single-wire, a pair of wires or a wire in proximity with ground, which can be seen as two wires if one resorts to image theory. According to Balanis, radiation occurs when charged particles are accelerated, meaning that a DC current through an infinite uniform wire will not radiate, because the speed of the electrons is kept constant [12, p. 9].

For a very thin wire with infinite conductivity and surface current I, we can write

$$\frac{\mathrm{d}I}{\mathrm{d}t} = q\frac{\mathrm{d}v}{\mathrm{d}t} \tag{2.1}$$

where q is the unit charge and v is the charge velocity. From equation (2.1) one understands that to obtain a time varying current, thus radiation, one only has to provide a velocity shift in the wire. Such can be accomplished by curving a wire, introducing an abrupt bend, resorting to a discontinuity in its diameter, placing it in proximity with ground or truncating it, as shown in Fig. 2.1. Additionally, as long as there is a time varying current, one can achieve radiation even if the wire is uniform, which is a favourable outcome for antenna designers. In general, where charges are accelerated, radiation occurs. This means that one only has to potentiate and exploit this phenomenon in order to get the most possible radiation out of a conducting structure.

In a two wire system, where opposite current flows exist, a transverse electromagnetic (TEM) wave will also exist between them. As the wires are curved and fringing fields start to develop,

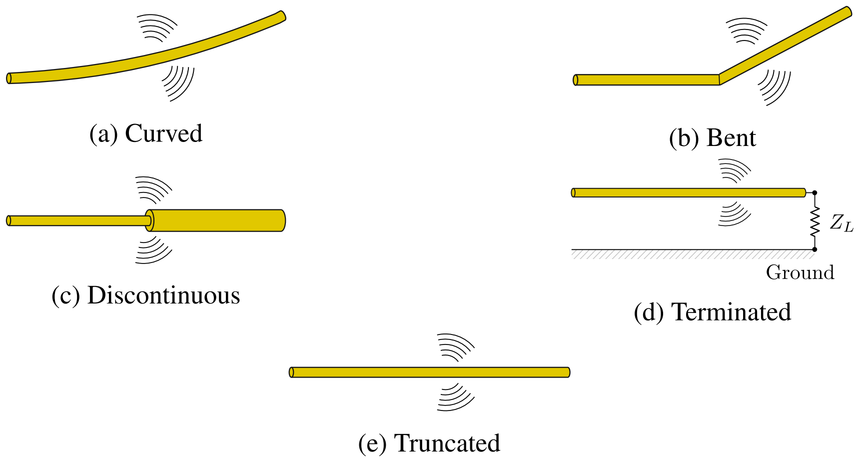

Figure 2.1: Wire radiation configurations [12, p. 10]

radiation of spherical waves also starts to occur, as depicted in Fig. 2.2. In the extreme case where the wires are bent 90° up and down we get a dipole antenna.

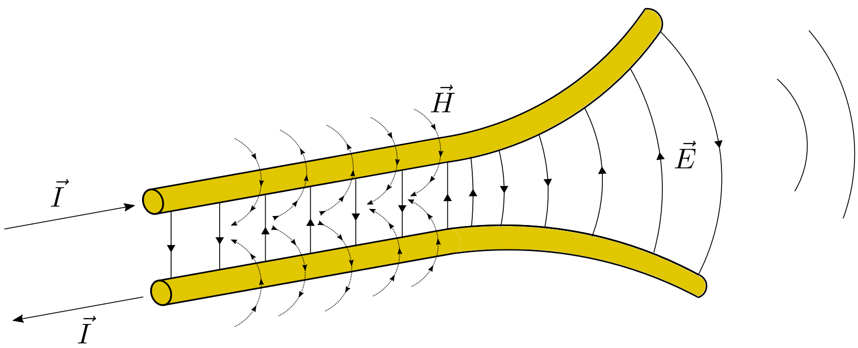

Figure 2.2: Two-wire radiating system

Other types of radiation mechanisms exist, like the one present in aperture antennas. In the simplest case, we can imagine an open waveguide in which, clearly, radiation will exist in the open end. The amount of radiation depends on the aperture of the waveguide end and we can look at this simple system as a discontinuity, because there is an abrupt change in the wave impedance from the inside of the waveguide to the free-space. This radiation mechanism is the basic principle of the well known horn antennas [12, p. 719].

In summary, getting a conductive structure to radiate is a rather simple task and one should take as much advantage of it as possible in order to obtain highly efficient antennas.

2.3 Figures-of-Merit

For successful antenna design, one has to comply with certain figures-of-merit that our antenna must fulfil. These are important characteristics that define how the antenna radiates, the bandwidth we have available to operate with it, how directive and efficient it is, as well as in which directions the E field is oriented. All of these allow the end-user designer of the antenna to have a very good knowledge on how it can be applied in real test-beds.

2.3.1 Radiation Pattern

As stated in the IEEE standard for definitions of terms for antennas [13], the radiation pattern of an antenna is defined as "The spatial distribution of a quantity that characterizes the electromagnetic field generated by an antenna". This quantity is usually described in spherical coordinates, which makes sense because of the spherical nature of the waves radiated by an antenna.

A wide span of other definitions can be derived from the radiation pattern representation such as the half-power beamwidth (HPBW), the first-null beamwidth (FNBW), the sidelobe level (SLL), the front-to-back ratio (FTBR), among others. The side-lobe level and the front-to-back ratio are particularly important parameters for directional antennas. The former relates the main beam amplitude to the highest side-lobe, which in practice expresses how immune the antenna is to the reception of radiation from undesired directions. It can also quantify how much radiation the antenna sends away from the main beam, since for a fully passive antenna, reciprocity applies. The front-to-back ratio relates the power radiated to the front (desired, main beam direction) to the power radiated to the back (undesired direction). For example, an antenna with an infinite reflector will have an infinitely large FTBR, which in practice is not realizable. Therefore, it is important to quantify this parameter to avoid unwanted interferences in the antenna system. A radiation pattern example of a directional antenna is shown in Fig. 2.3.

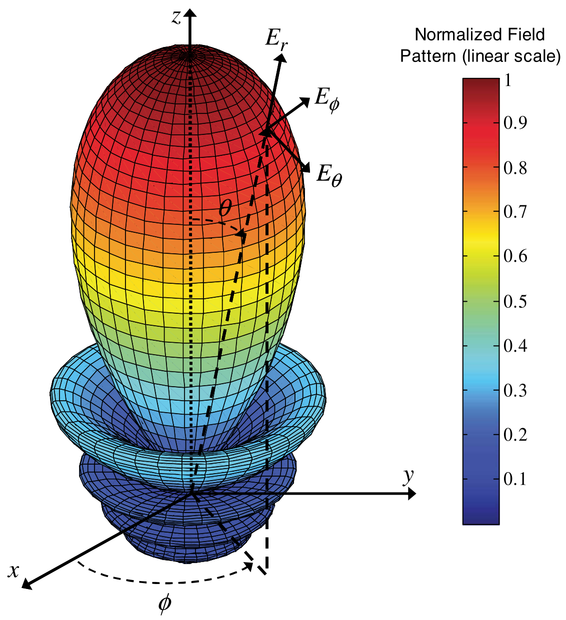

Figure 2.3: Radiation pattern example [12, p. 29]

Most of the time, 3D equipment for full characterization of antenna pattern is not available. For this reason and because it is time consuming to obtain such a full characterization, it is common to measure the radiation patterns on th so called E-plane and H-plane. These are 2D radiation measurements in two distinct orthogonal planes that allow one to extrapolate the 3D radiation characteristics of an antenna. In Fig. 2.4 it is possible to see a schematic representation of the fields in a dipole antenna, as well as the corresponding Poynting vector. For the H-plane radiation pattern, one would look at the gain in the xy plane, which is the one that contains the magnetic field. Following the same logic for the E-plane, we could measure the gain in any plane orthogonal to the xy. However it is usual to use the xz and the yz planes that correspond to $\phi = 0°$ and $\phi = 90°$, respectively. This type of measurement makes the assumption that the fields are exactly known as shown in Fig. 2.4, which is almost always the case.

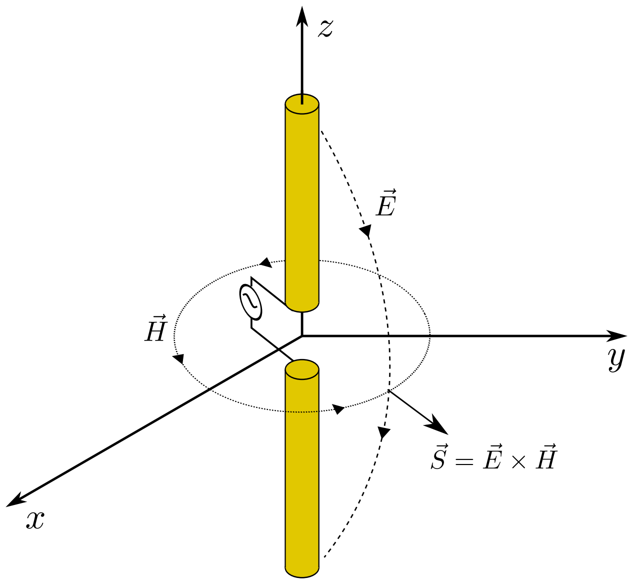

Figure 2.4: Schematic field representation of dipole antenna.

2.3.2 Radiation Power Density and Intensity

Radiation power density describes the power flux that traverses a particular area of the sphere around the antenna. For harmonically time-varying fields we can write the time average radiation power density (Poynting vector) as

$$\vec{W}_{rad} = \frac{1}{2}\Re\left[\vec{E} \times \vec{H}^*\right] \tag{2.2}$$

in which E and H represent the peak values of the electric and magnetic fields, respectively. Equation (2.2) may lead one to wonder about the significance of the imaginary part of the vector product $E \times H^*$. According to Balanis, it represents the reactive power density associated with the electromagnetic (EM) fields, which can be shown to be predominately real in the far-field region [12, p. 36]. If radiation takes place in a lossy medium, this stored power density is significantly increased and we can not speak about far-field, since in the infinity there will be no radiation as a consequence of losses. From equation (2.2) it is possible to obtain the total radiated power from an antenna by integrating through the entire area of the sphere, as follows

$$P_{rad} = \frac{1}{2} \oiint_S \Re\left[\vec{E} \times \vec{H}^*\right] \cdot \mathrm{d}s \tag{2.3}$$

The radiation intensity of an antenna expresses the power radiated per unit solid angle and is measured in W/sr. As it depends on the direction it is calculated, we can foresee its usefulness for calculating parameters such as the directivity and the radiation pattern of an antenna. Mathematically, this parameter can be defined in the far-field (no radial component of the electric field) as [12, p. 38],

$$U(\theta,\phi) \approx \frac{1}{2\eta}\left[|E_\theta(\theta,\phi)|^2 + |E_\phi(\theta,\phi)|^2\right] \tag{2.4}$$

where η is the characteristic impedance of the medium, E_θ and E_ϕ are the components of the electric field in θ and ϕ respectively. Equivalently we can define the radiation intensity as

$$U = r^2 W_{rad} \tag{2.5}$$

and calculate the total radiated power by making

$$P_{rad} = \oiint_\Omega U \mathrm{d}\Omega = \int_0^{2\pi}\int_0^{\pi} U(\theta,\phi)\sin(\theta)\,\mathrm{d}\theta\,\mathrm{d}\phi \tag{2.6}$$

in which $\mathrm{d}\Omega$ represents an infinitesimal portion of solid angle.

2.3.3 Bandwidth

As defined in the IEEE standard for definitions of terms for antennas, the bandwidth of an antenna is the "range of frequencies within which the performance of the antenna conforms to a specified standard with respect to some characteristic" [13]. According to Balanis, two types of bandwidth are typically defined: the impedance and the pattern bandwidths [12, p. 65]. These frequency ranges are expressed differently depending if we are dealing with broadband or narrowband antennas. They can be defined as a ratio of the upper-to-lower frequency or as a fractional bandwidth in percentage, accordingly. A broadband antenna example that has a satisfactory behaviour from 1 GHz to 12 GHz is said to have a 12 : 1 bandwidth, whereas a narrowband antenna that has a 100 MHz bandwidth at a centre frequency of 1 GHz has a fractional bandwidth of 10 %.

The impedance bandwidth of an antenna is usually described as the frequency range where the reflection coefficient, Γ, or the voltage standing wave ratio, VSWR, remain below a certain value. In most antennas, it can be seen that the restrictions in terms of reflection coefficient are $VSWR < 2$, $|\Gamma| < 0.3$ or equivalently $|\Gamma|_{\mathrm{dB}} < -10$. These are well known quantities from transmission line theory and are given as follows

$$\Gamma = \frac{Z_{in} - Z_0}{Z_{in} + Z_0} \tag{2.7}$$

where Z_{in} is the input impedance of the antenna and Z_0 the characteristic impedance of the transmission line that feeds the antenna. The VSWR can be related with the reflection coefficient using

$$VSWR = \frac{1+|\Gamma|}{1-|\Gamma|} \tag{2.8}$$

Furthermore, it is also usual to define antenna parameters in terms of scattering parameters. The S_{11} parameter is given to evaluate the impedance bandwidth of an antenna and it coincides with Γ, for one port antennas. Usually, its magnitude is given in dB by making

$$|S_{11}|_{\mathrm{dB}} = |\Gamma|_{\mathrm{dB}} = 20\log_{10}(|\Gamma|) \tag{2.9}$$

Pattern bandwidth can be seen as how stable the radiation pattern of the antenna is with frequency. In wideband antennas this is a critical parameter as a consequence of the extremely wide impedance bandwidths. Most of the time, this type of antennas presents a low reflection coefficient in a wide frequency range, but their radiation pattern might shift significantly through frequency. Pattern bandwidth can be seen as the frequency range where the far-field pattern remains within a pre-determined mask.

2.3.4 Directivity, Efficiency and Gain

The IEEE standard for definitions of terms for antennas states that the directivity of an antenna can be seen as "the ratio of the radiation intensity in a given direction from the antenna to the radiation intensity averaged over all directions" [13]. Equivalently, it can be said to be the ratio of the radiation intensity produced in a particular direction by the antenna to the radiation intensity produced as if it was an isotropic radiator. Putting such definition mathematically, it is easy to understand that

$$D(\theta,\phi) = \frac{U(\theta,\phi)}{P_{rad}/4\pi} = \frac{4\pi U(\theta,\phi)}{P_{rad}} \tag{2.10}$$

One can expect that, as in any other passive system, some losses can occur within the antenna system. These can be grouped in mismatch, conduction and dielectric losses [12, pp. 60-61]. Mismatch losses occur as a consequence of high reflection coefficients, which result in very little power accepted by the antenna that reflects most of it back to the source. Ohmic losses are related to the finite conductivity and the size of the conductors that constitute the antenna. Dielectric losses occur because of a residual conductivity in a dielectric material. Equivalently, these can be seen as the wasted energy by the polar molecules, that constitute a dielectric, to shift their position as the external applied field changes harmonically with time. In [12, pp. 60-61], Balanis quantifies the overall efficiency of an antenna as

$$e_0 = e_r \cdot e_c \cdot e_d \tag{2.11}$$

where e_r represents the mismatch efficiency, e_c the conduction efficiency and e_d the dielectric efficiency. According to IEEE standard for definitions of terms for antennas, the radiation efficiency is the “ratio of the total power radiated by an antenna to the net power accepted by the antenna from the connected transmitter” [13]. From this definition, by taking the circuit of Fig. 2.5 into account, we can write the radiation efficiency as

$$e_{rad} = \frac{P_{rad}}{P_{acpt}} = e_c \cdot e_d \tag{2.12}$$

which does not depend on the mismatch between the antenna and the transmitter, but only on the radiated power and dissipated power within the antenna, since $P_{acpt} = P_{rad} + P_{diss}$.

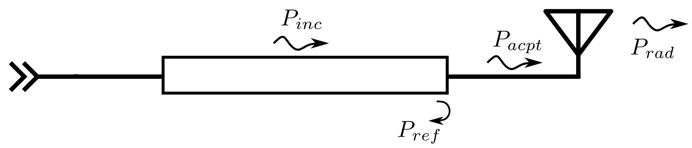

Figure 2.5: Circuit schematic of antenna system.

The gain of an antenna is defined in [13] as “ratio of the radiation intensity in a given direction to the radiation intensity that would be produced if the power accepted by the antenna were isotropically radiated”, which is very similar to the definition of directivity that was discussed earlier in this subsection. However, this definition relates to the accepted power and not the actual radiated power as it is the case with the directivity parameter. Since we know that $P_{rad} = e_{rad} \cdot P_{acpt}$, we can easily write the gain as

$$G(\theta,\phi) = \frac{4\pi U(\theta,\phi)}{P_{acpt}} = e_{rad} \cdot D(\theta,\phi) \tag{2.13}$$

Nonetheless, this definition of gain hides the full behaviour of the antenna. That is the case since no power will be accepted by the antenna if a full mismatch exists at its input, resulting in no radiation at all. For this reason realized gain is also defined in [13], where it is said that it is no more than the gain weighted by the mismatch loss. So, we can write the realized gain of an antenna as

$$G_{re}(\theta,\phi) = (1-|\Gamma|^2) \cdot \frac{4\pi U(\theta,\phi)}{P_{acpt}} = e_0 \cdot D(\theta,\phi) \tag{2.14}$$

where the factor $1-|\Gamma|^2 = e_r$ is the mismatch efficiency.

2.3.5 Polarization

In [12, pp. 66] Balanis quotes the definition of polarization of a wave radiated by an antenna as the "property of an electromagnetic wave describing the time-varying direction and relative magnitude of the electric-field vector; (...)". In other words it can be seen as the vector that is collinear with the electric field vector at any point of the far-field. This property can be divided in linear, circular or elliptical polarization.

Linearly polarized antennas are the most common because of their simplicity. However, linear polarization faces certain issues such as polarization mismatch. If the transmitting and receiving antennas are not perfectly aligned, polarization mismatch will degrade the power budget by a factor of $\cos(\psi)$, where ψ is the angle between the polarization of the two antennas.

In circular and elliptical polarizations, the E-field vector rotates as time goes by and these can be seen as the superposition of two linearly polarized outphased linear sources. One of the greatest advantages of this type of polarization is the fact that the power budget between two antennas is insensitive to misalignments of their axes. Another immediate advantage is that in line-of-sight communications when a wave with such polarization is reflected in a surface, its polarization shifts from right- to left-hand, or vice-versa. An antenna that radiates and receives right-hand circularly polarized waves (RHCP) is rather insensitive to left-hand circularly polarized waves (LHCP) waves, therefore reducing multipath interference on the communication system. One way to understand the polarization of a wave is by looking from its source to the infinity (in the direction of the Poynting vector) and if the E-field vector rotates clockwise we have RHCP, otherwise we have LHCP. In Fig. 2.6 an example of an RHCP wave is depicted.

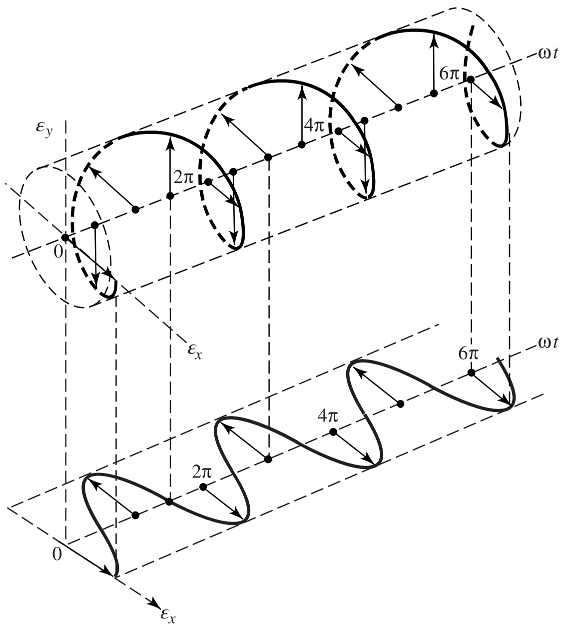

Figure 2.6: Circularly polarized wave example [12, pp. 67].

2.4 Antenna Arrays

In many applications, single element antennas are not capable of providing highly directive radiation patterns, much less reconfigurable steerable patterns. When designing antennas for base stations it is sometimes desirable that the radiation is stronger in certain directions and pattern nulls exist in others. This can reinforce signal strength from/to the desired devices and significantly reduce the reception/transmission to other devices capable of receiving the same signal.

The total field of an antenna array is obtained by the linear combination of the individual fields radiating from each unit cell. This allows the antenna designer to have the fields interfering constructively in certain directions and destructively in others [12, pp. 285]. It also gives additional flexibility controlling the magnitude of sidelobes, overall peak gain and in the case of digital or hybrid beamforming multiple simultaneous beams.

2.4.1 Two-Element Array

The simplest form of antenna array is a combination of just two unit cell antennas as shown in Fig. 2.7. For simplicity one can just assume them to be infinitesimal dipoles whose field is well known.

As stated before, the total field is simply a linear combination of each of the fields radiated by each cell, which considering Fig. 2.7a is given as

$$\vec{E}_t = \vec{E}_1 + \vec{E}_2 = \hat{a}_\theta j\eta \frac{kI_0 l}{4\pi} \left\{ \frac{e^{-j[kr_1-(\beta/2)]}}{r_1} \cos\theta_1 + \frac{e^{-j[kr_2+(\beta/2)]}}{r_2} \cos\theta_2 \right\} \tag{2.15}$$

where $k = 2\pi/\lambda$, I_0 is the excitation current of each antenna and β the phase offset between the excitations of each antenna [12, pp. 286]. Since in the far field assumption, the distance of observation is much greater than the distance between the antennas, the amplitude of each of these fields, which depends on the distance r, is approximately the same. That is $r_1 \approx r_2 \approx r$ and $\theta_1 \approx \theta_2 \approx \theta$. However, because of the fact that slight distance changes can yield significant phase differences between the two radiators, the phase difference can not be neglected, when calculating the total resultant electric field. Considering the aforementioned approximations illustrated in Fig. 2.7b, the total field at the far-field region of a two element array can be written as

$$\vec{E}_t = \hat{a}_\theta j\eta \frac{kI_0 l}{4\pi} \cos\theta \left\{ 2\cos\left[\frac{1}{2}(kd\cos\theta + \beta)\right]\right\} \tag{2.16}$$

which is simply the field of one radiator by itself, multiplied by a factor, called the array factor.

This result allows one to conclude that to obtain the total radiation pattern of an array all one has to do is to simply multiply the array factor by the pattern of the radiator that serves as the unit cell of our array. An important consideration, however, is the fact that this conclusion neglects mutual coupling between the two antennas which changes their radiated fields.

2.4.2 N-Element Linear Arrays

The previous two element case can now be extrapolated to account for the existence of N elements in the array, as simply the summation of the several field contributions of the several sources. In Fig. 2.8 a schematic representation of an N-element uniform linear array is shown. Considering β

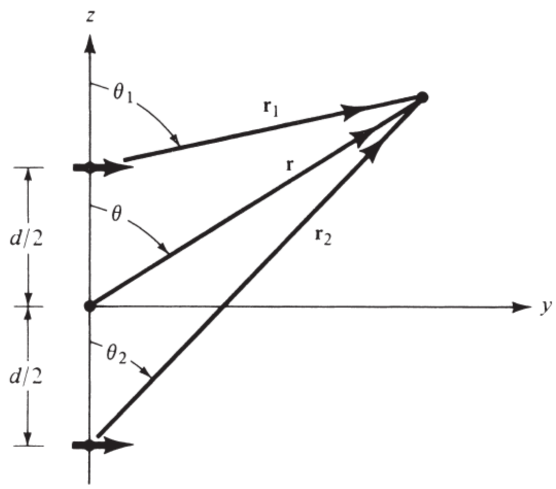

(a) Without approximations.

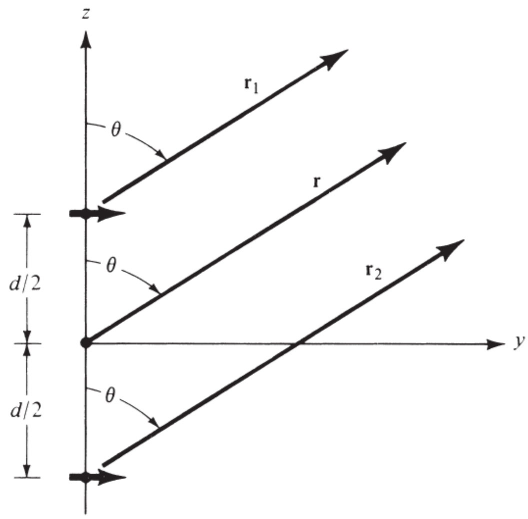

(b) With far-field approximations.

Figure 2.7: Two-element array along Z-axis [12, pp. 287].

to be a progressive phase shift between each antenna, one can write the array factor, for the case where the distances between antennas is kept constant and equal to d, as

$$AF = 1 + e^{j(kd\cos\theta+\beta)} + e^{j2(kd\cos\theta+\beta)} + \cdots + e^{j(N-1)(kd\cos\theta+\beta)} \tag{2.17}$$

This equation is only valid under the assumptions it was derived, namely that the distance between the radiating elements is constant and no longer applies if the distance between each consecutively antenna is changed arbitrarily. Additionally, in the case of series feed arrays, the progressive phase shift β varies with frequency. This introduces a new phenomenon called beam squint in which the beam direction varies with frequency, because $beta$ varies with frequency. Furthermore, instead of using a progressive phase shift, for beam synthesis purposes it may be useful to have arbitrary phases and amplitudes for the excitation currents of each radiator. In this

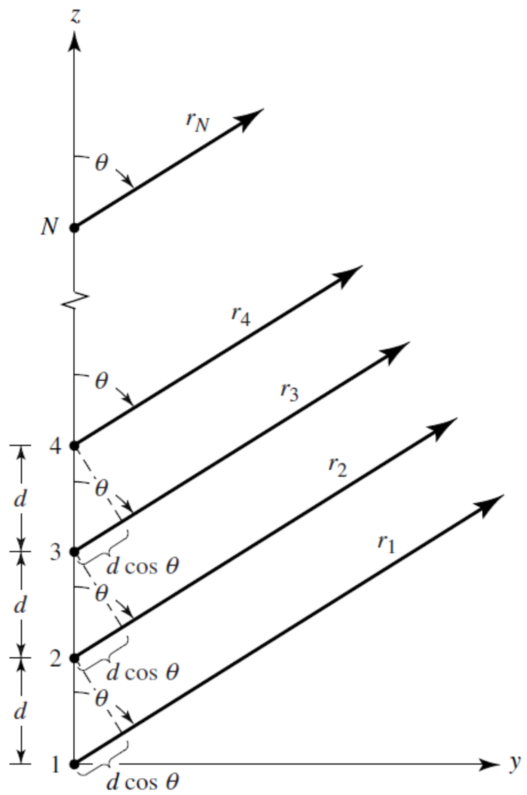

Figure 2.8: N-element linear uniform array [12, pp. 294].

case a more generic expression can be written

$$AF = \bar{a}_0 + \sum_{i=1}^{N-1} \left[\bar{a}_i e^{jk \sum_{j=1}^{i} [d_j] \cos\theta} \right] \tag{2.18}$$

in which the coefficients $\bar{a}_i$ represent the complex amplitude excitations of each antenna in the array.

2.4.3 Planar Arrays

Planar arrays are quite useful in antenna technology as they allow an extra degree of freedom for tuning parameters such as the sidelobe level for example [12, pp. 348]. Contrary to linear arrays, in planar arrays due to their geometrical arrangement, the main beam can be pointed to anywhere in space, resulting in a more flexible operation that has numerous advantages for radar and communication systems.

A planar array can be thought as a linear combination of M linear arrays with N elements each. Therefore the same rationale can be applied as in the previous subsections, in which neglecting mutual coupling one can simply sum the contributions of each individual element. Considering Fig. 2.9, according to Balanis we can write the array factor of a uniformly spaced planar array, given the sub-array rationale, as

$$AF = \sum_{n=1}^{N} I_{1n} \left[\sum_{m=1}^{M} I_{m1} e^{j(m-1)(kd_x \sin\theta\cos\phi+\beta_x)} \right] e^{j(n-1)(kd_y \sin\theta\sin\phi+\beta_y)} \tag{2.19}$$

where I_{1n} and I_{m1} are the excitations of the sub-arrays. The distances d_x and d_y are the spacing on the x and y axes, respectively. β_x and β_y represent progressive phase shifts on the x and y sub-arrays.

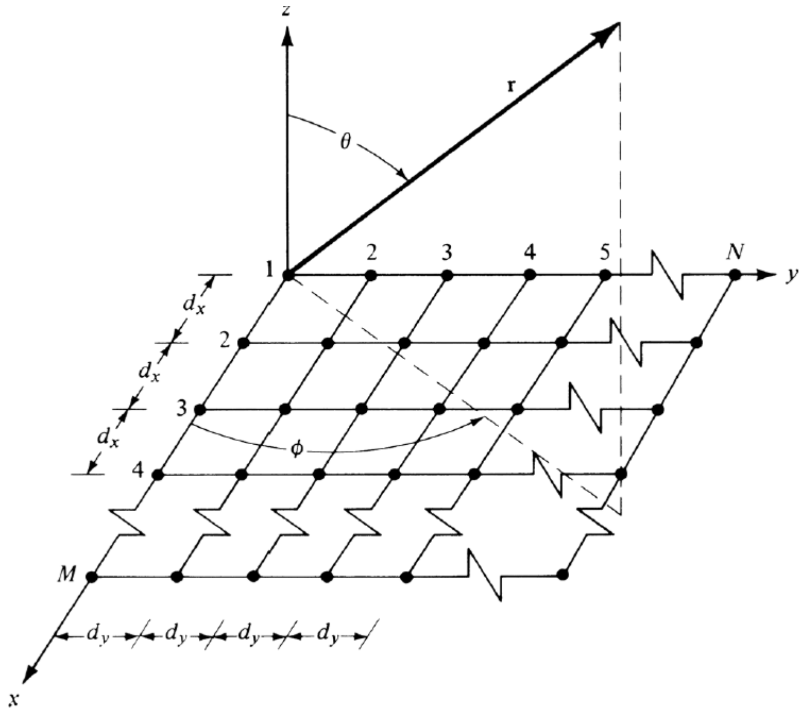

Figure 2.9: N by M elements planar array [12, pp. 294].

If arbitrary excitations of each element are possible, as it can be the case in hybrid or full digital beamforming, equation (2.19) should be changed accordingly and is rewritten as

$$AF = \bar{a}_{00} + \sum_{n=1}^{N-1} \sum_{m=1}^{M-1} \left[\bar{a}_{nm} e^{jk(\sum_{i=1}^{n}[d_i]\sin\theta\cos\phi + \sum_{i=1}^{m}[d_i]\sin\theta\sin\phi)} \right] \tag{2.20}$$

2.5 Summary

In this chapter a review on the key concepts needed for the realization and understanding of this thesis was presented. The fundamental figures-of-merit related to antenna design were also deeply analysed, as they will be the main characterization parameters of the antennas developed in this work.

Chapter 3

Meander-Line Antenna for a BLE System-In-Package

3.1 Introduction

Bluetooth Low Energy has been gaining ground as a choice for IoT devices [4]. However, given the frequency allocation of this technology ($2.4 - 2.48\,\text{GHz}$), in some applications the size of the devices can be larger than what would be desired. This is mostly because the dimensions of the ground plane are usually much larger than the dimensions of the radiating element. When considering integration of the antenna in the package, the ground-plane also has to be reduced to a minimum which results in other problems such as being the plane part of the antenna element. In this chapter the miniaturization of a radiating element and its ground-plane to enable package integration is presented.

3.2 Electrically Small Antennas

Electrically small antennas are radiating elements which are usually a small fraction of the operating wavelength, and therefore require special attention. They are usually employed in high-density miniaturized integrations at mostly low frequencies. In this section such antennas are given a particular focus where their properties and fundamental limitations are presented. The extensive work performed by Fujimoto on this subject is used as a background for this section [14].

3.2.1 Definition

At the end of 1947 Wheeler defined a boundary for an antenna to be considered electrically small. According to his work, an electrically small antenna is treated as such when its maximum dimension does not exceed the radian length [15]. Equivalently, if we can include the antenna inside a sphere of radius a, the radius should be such that it satisfies

$$a < \frac{\lambda}{2\pi} \Leftrightarrow ka < 1 \tag{3.1}$$

where λ denotes the free-space wavelength and k the wave number. If the antenna is composed of a radiating element and an infinite ground plane, then the sphere radius is defined so that half of sphere is set above the ground plane and fully wraps the element. These sphere definitions are shown in Fig. 3.1.

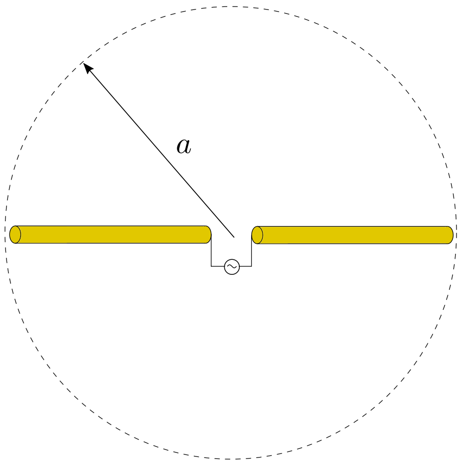

(a) Electrically small dipole.

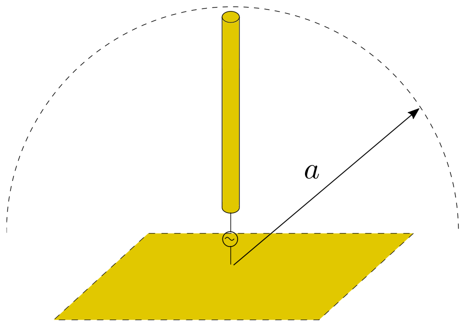

(b) Electrically small monopole.

Figure 3.1: Wheeler sphere representation for electrically small dipole (a) and monopole (b).

In his work, Wheeler also realized that an antenna with size limitations behaves approximately as a lossy lumped inductor or capacitor. From this reasoning he anticipated that inherent bandwidth limitations should rise from reducing the size of the antenna, which can be compensated at the expense of radiation efficiency. These concepts will be discussed further in the next sections.

3.2.2 Behaviour of Electrically Small Antennas

Due to their reduced size, the behaviour of electrically small antennas is specifically analysed in this section. Their input impedance is considered, as well as the radiation efficiency degradations that can take place as a consequence of losses. Additionally, the proximity of conductive materials, such as finite ground planes, near an ESA (electrically small antenna) is considered.

3.2.2.1 Input Impedance

Small antennas behave approximately as lumped elements, as foreseen by Wheeler in 1947. They usually present high reactances and moderate to low radiation resistances. The following analysis of the input impedance of electrically small antennas considers only losses due to radiation, therefore the real part of their input impedances effectively matches their radiation resistance. The conductor losses are taken into account in the next section.

According to Fujimoto [14, p. 12], the input impedance $Z_a = R_a + \mathrm{j}X_a$ of an electrically small dipole of total length $2a$ and wire diameter d is given by

$$R_a = 20(ka)^2 \tag{3.2}$$

$$X_a = -\frac{60\left[\ln\left(\frac{2a}{d}\right) - 3.39\right]}{ka} \tag{3.3}$$

For an electrically small loop antenna of radius a and wire diameter d, Fujimoto states that the input impedance can be given by

$$R_a = 20\pi^2(ka)^4 \tag{3.4}$$

$$X_a = \omega \cdot a \cdot \mu \cdot [\ln(8a/d) - 2] = (ka) \cdot c \cdot \mu \cdot [\ln(8a/d) - 2] \tag{3.5}$$

where c is the speed of light in the free space and μ the magnetic permeability.

From these two expressions it is possible to understand that, as expected, a small dipole will behave as a capacitor, whereas an electrically small loop behaves as an inductor. One can look at this behaviour if the circuit models are used for the first resonance of these two antennas. The resonance of the dipole is shown as a series RLC, while the first anti-resonance of the loop antenna can be modelled as a parallel RLC. At frequencies much lower than their first resonating mode (where the antennas are electrically small), in the series RLC the capacitive behaviour dominates, whereas in the shunt RLC the inductive behaviour prevails. In both cases it is possible to calculate the quality factor of the antennas using the well known expressions for the Q factor of inductors and capacitors. Doing so, one obtains

$$Q_{dipole} = \frac{|X_a|}{R_a} = \frac{60\left[\ln\left(\frac{2a}{d}\right) - 3.39\right]}{20(ka)^3} \tag{3.6}$$

and

$$Q_{loop} = \frac{|X_a|}{R_a} = \frac{c \cdot \mu \cdot [\ln(8a/d) - 2]}{20\pi^2(ka)^3} \tag{3.7}$$

from which it is clear that the Q factor of an ESA is proportional to $1/(ka)^3$. As stated before, these values assume that only radiation losses take place, which is very far from the real scenario.

Additionally we can see that limitations exist on the Q of an antenna as predicted by Wheeler, which will be discussed further in this section.

3.2.2.2 Radiation Efficiency

The radiation efficiency of electrically small antennas is much more sensitive than regular sized antennas because of the small radiation resistance that was seen to exist in this type of radiators. According to Fujimoto [14, p. 17], the radiation efficiency of an antenna can be given by

$$e_{rad} = \frac{R_{rad}}{R_{rad} + R_{loss}} \tag{3.8}$$

where R_{rad} and R_{loss} denote the resistances that model radiation and losses, respectively.

If we differentiate equation (3.8) with respect to R_{loss} we can understand how a shift in the losses has an impact on the radiation efficiency. Doing so, yields

$$\Delta e_{rad} = \frac{\mathrm{d}e_{rad}}{\mathrm{d}R_{loss}} \times \Delta R_{loss} = -\frac{R_{rad}}{(R_{rad} + R_{loss})^2} \times \Delta R_{loss} \tag{3.9}$$

If one evaluates the efficiency decrement in the case where no losses exist, *i.e.* $R_{loss} = 0$, we get

$$\Delta e_{rad} = -\frac{\Delta R_{loss}}{R_{rad}} \tag{3.10}$$

from which we see that having a lower R_{rad} results in a greater decrement in efficiency Δe_{rad} for the same increment in losses ΔR_{loss}. Therefore, minimizing losses of an ESA is of utmost importance for satisfactory radiation efficiency of the antenna.

3.2.2.3 Proximity of Conductive Materials

Generally, the performance of antennas is affected by the proximity of other materials, either insulating or conductive ones. Fujimoto gives a monopole placed on a ground plane as an example [14, pp. 20-21]. Usually, an infinite ground plane is assumed and the characteristics of the antenna can be determined assuming the existence of an image monopole, hence we can treat the antenna as a dipole. However, in practical scenarios the ground plane has a finite size. Therefore, this conductive plane may have currents that contribute to radiation, deviating its behaviour from the expected dipole performance.

Another example given by Fujimoto is ceramic-chip antennas, in which a high permittivity dielectric wraps the antenna. This results in much smaller physical dimensions of the radiating element. Nonetheless, such reduction in size comes at the expense of reduced efficiency as a consequence of the high permittivity that surrounds the antenna.

In an attempt to make antennas independent of their surroundings, some antennas have been designed with EBG (electromagnetic bandgap) materials around them. These are metallic engineered materials that can exhibit favourable properties for the radiation of the antenna in a certain frequency band. According to Fujimoto this technique has been widely used for miniaturizing antennas, mutual coupling reduction, as well as lowering their profile by placing monopoles and dipoles parallel to N-PEC surfaces.

3.2.3 Fundamental Limits

As it was previously discussed, Wheeler anticipated the existence of limitations in electrically small antennas. In the discussions about the input impedance of small antennas, we realized that their quality factor was proportional to $1/(ka)^3$, where a is the radius of the sphere that wraps the ESA.

In 1996, McLean advanced the state-of-the-art done in small antennas by establishing a fundamental limitation for the minimum possible quality factor of an ESA [16]. According to his work, the minimum quality factor of a small antenna is given as

$$Q_{min} = \frac{1}{(ka)^3} + \frac{1}{ka} \tag{3.11}$$

From equation (3.11), one can realize that by reducing the antenna size, the minimum possible quality factor will increase, thus the bandwidth of the antenna will decrease. Nonetheless, this equation assumes that all losses take place through radiation, meaning that we can reduce the minimum Q by introducing additional losses [17]. According to Best we can obtain the lower bound for the quality factor of an antenna by employing

$$Q_{min} = e_{rad} \cdot \left[\frac{1}{(ka)^3} + \frac{1}{ka}\right] \tag{3.12}$$

which is similar to McLean's expression, but accounts for possible non-radiative losses that occur in the antenna system. Typically, these losses are not desired as they will result in reduced gain which is a disadvantage.

According to Fujimoto [14, p. 33], the fractional impedance bandwidth of an electrically small antenna at a VSWR of $s:1$ is given by

$$FBW(\%) = 100 \times \frac{s-1}{Q_{min}\sqrt{s}} = 100 \times \frac{2|\Gamma|}{Q_{min}\sqrt{1-|\Gamma|^2}} \tag{3.13}$$

where Γ denotes the desired reflection coefficient for bandwidth determination. Once again, it is clear that reducing the size of the ESA, thus increasing the minimum Q will result in a smaller fractional bandwidth for a certain definition of VSWR or reflection coefficient.

3.3 Meander-Line Monopole Antenna in Package

Meander-line antennas have been studied for miniaturization purposes in various applications such as handset, RFID tags and IoT sensor antennas [18–21]. This type of miniaturization approach can produce electrically small antennas, since it supports a slow-wave mode by introducing an extra delay in the propagation time of an electromagnetic wave from the feed-point to the end of the antenna [14]. Nonetheless, this technique for the miniaturization of antennas is usually supported by bulky ground planes which can be incompatible with many IoT applications, such as Bluetooth, where the full antenna system size is desired to be as small as possible.

As a consequence of the reduced footprint of radiating elements needed for package integration, large ground planes are usually required on the hosting PCB. Finite ground-planes change the behaviour of the radiating element, as themselves take part in the radiation process [14,22,23]. If the size of the ground-plane is a large fraction of the wavelength, it can be used to extend the bandwidth of the radiating element. However, when the ground-plane size is very small, additional miniaturization efforts are needed and narrow bandwidths are obtained. Table 3.1 summarizes some literature examples of electrically small antennas, in which it is clear that the size of the ground plane is usually much larger than the radiating element.

Table 3.1: Summary of package-sized miniature antennas for BLE frequency band (2.4 GHz).

Reference	Radiating Element Size	Ground Size	Peak Gain
[24]	$12 \times 15 \times 3$ mm	70×100 mm	3.4 dBi
[25]	$10 \times 3 \times 3.5$ mm	100×44 mm	2.7 dBi
[26]	$8.5 \times 3 \times 3.25$ mm	40×30 mm	1.7 dBi
[27]	$8 \times 4 \times 1$ mm	18×30 mm	0.6 dBi
[28]	$8 \times 2 \times 0.5$ mm	22×15.5 mm	0.5 dBi
This Work	$7.5 \times 4 \times 1$ mm	8.6×7.5 mm	-8.7 dBi

3.3.1 Antenna Design

The requirement for the design of this BLE SiP antenna is that it can communicate at 100 m distance in free space with a transmitted power of 0 dBm. The receiver sensitivity is -96 dBm [29] and the receiving antenna is assumed to have a gain of 0 dBi, which results in the requirement for the meander-line antenna of a realised gain above -16 dBi. Furthermore, to avoid large mismatches between the antenna and the 50 Ω matched IC the reflection coefficient magnitude is required to be below -6 dB in the BLE frequency band spanning from 2.4 to 2.48 GHz.

3.3.1.1 Feasibility Study

The top-level layout of the circuit and antenna design areas are depicted in Fig. 3.2. The area denoted as BLE SiP is covered with ground plane and signal traces. Such size limitations are imposed by the SiP manufacturer. As seen in section 3.2, the ground plane enables us to calculate the theoretical boundaries of the antenna by just considering a half-sphere above it that wraps the radiating element. Doing so, one can obtain the radius of the half-sphere that wraps the antenna design area to the right of the ground plane as $a = \sqrt{(7.5/2)^2 + 4^2} = 5.48$ mm.

By resorting to equations (3.12) and (3.13) one can obtain the maximum possible -10 dB bandwidth ($|\Gamma| = 1/3$) at the centre frequency of 2.44 GHz as a function of the radiation efficiency. Such analysis is done and plotted in Fig. 3.3. It can be seen that the maximum theoretical

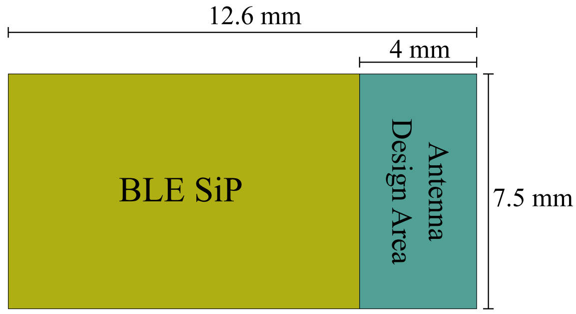

Figure 3.2: Top-level SiP layout with outlined antenna design and circuit areas.

bandwidth attainable is larger than the needed 80 MHz at the frequency of 2.44 GHz for a radiation efficiency smaller than 43 %.

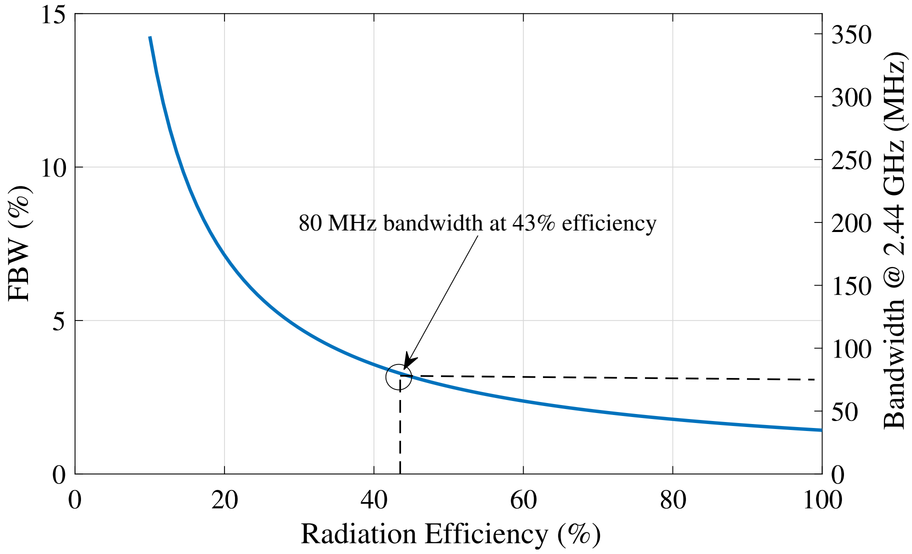

Figure 3.3: Analysis of maximum attainable bandwidth with varying radiation efficiency for $f_c = 2.44\,\mathrm{GHz}$ and sphere radius $a = 5.48\,\mathrm{mm}$.

Since the available ground plane is finite and much smaller than the typical sizes seen in Table 3.1, considerable deviations from the presented theoretical limitations are expected.

3.3.1.2 Meander-Line Analysis

Endo *et al.* proposed a combination of shorted parallel two wire transmission lines and a straight wire element to model a full meander dipole antenna [30]. Equivalently, they state that their model can be seen as a linear dipole with centre inductance loading. In 2009 Zhonghao revisited the same method for the analysis of meander lines [31]. Endo's work was closely followed and it was concluded that by equating the total self-inductance of a meandered dipole antenna to the self inductance of a half-wave dipole, the resonant wavelength, λ, of the former can be obtained by the transcendental equation

$$\frac{\mu_0 s}{2\pi} \cdot \left[\ln\left(\frac{4s}{b}\right) - 1\right] + m \cdot \frac{\mu_0 h}{\pi} \cdot \ln\left(\frac{2w}{b}\right) \cdot \left[1 + \frac{1}{3}(kh)^3\right] = \frac{\mu_0 \lambda}{4\pi}\left[\ln\left(\frac{2\lambda}{b}\right) - 1\right] \tag{3.14}$$

in which the parameters s, w, b and h represent the length of the antenna, the distance between the twin wires that form the transmission line, the diameter of the conductor and the length of the twin wire transmission line, respectively. These are shown in Fig. 3.4 for better understanding. The parameter m represents the number of meanders which, in the case of Fig. 3.4, is $m = 2$. As usual, μ_0 represents the magnetic permeability of vacuum. Endo also provided an analysis of the radiation efficiency of a meander-line dipole antenna. They concluded that the antenna size and radiation resistance reduction ratios are equal when comparing the antenna to an half-wave dipole resonant at the same frequency. Hence, we can write the radiation resistance of the meander-line dipole antenna as

$$R_{rad} = \frac{2sR_d}{\lambda} \tag{3.15}$$

and the loss resistance considering only the skin-effect is written as

$$R_{loss} = \frac{\rho}{\delta \pi b} \cdot (s + 2mh) \tag{3.16}$$

where $R_d = 73\,\Omega$ is the well known radiation resistance of an half-wave dipole, ρ the resistivity of the conductor and δ the skin depth. The term $(s+2mh)$ represents the total conductor length of the meander-line dipole. Having the radiation and loss resistances characterized, the radiation efficiency can be obtained by the well known expression

$$e_{rad} = \frac{R_{rad}}{R_{rad} + R_{loss}} \tag{3.17}$$

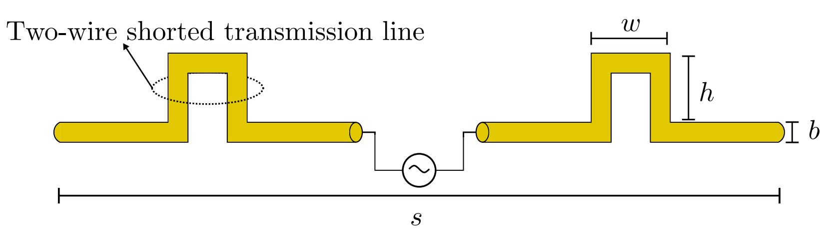

Figure 3.4: Meander line dipole parameters.

Furthermore, Endo advanced that his method can be applied to the case of flat conductors in planar technology if the proper equivalent wire diameter is used. The effective diameter b from a flat conductor with thickness t and width a, is then obtained from [12, pp. 506] as

$$b = 2 \cdot (0.25a + 0.353t) \tag{3.18}$$

Since the resonant frequencies of a half-wave dipole and a quarter-wave monopole are similar, the final conclusion is that the resonant frequency of a meander-line monopole can be obtained from equation (3.14) where b is calculated by means of (3.18). The radiation efficiencies of the dipole and monopole should also be the same, since the monopole has half the radiation resistance, half the length, and thus half the ohmic losses of the dipole.

To validate the theoretical predictions of Endo and Zhonghao, a meander-line antenna represented in Fig. 3.5 is simulated using finite element method (FEM) in HFSS, where the red circle denotes the antenna feedpoint. Its resonant frequency and efficiency are compared against the values obtained by Endo's model.

The stackup used for the simulation of the packaged meander-line antenna is shown in Fig. 3.6. The metal redistribution layers (RDx) and under-bump metallization (UBM) are composed of copper. The dielectric layers (DLx) are made of polyimide (PI) and MC stands for mold compound which is the material of this layer. The relative permittivities of MC and PI, at the frequency of 2.5 GHz, are 3.7 and 3.6, respectively. Their loss tangents at the same frequency are 0.005 for the MC and 0.04 for PI. The total size of the package is 12.6×7.5 mm.

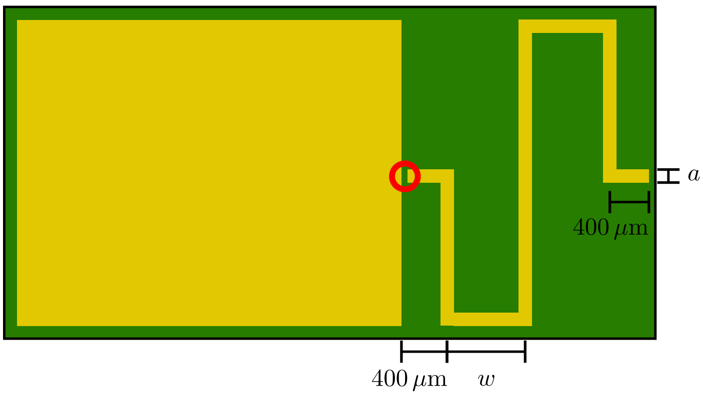

Figure 3.5: Simulation model variables: a is the trace width and w the meander width obtained by dividing the remaining length by the number of meanders.

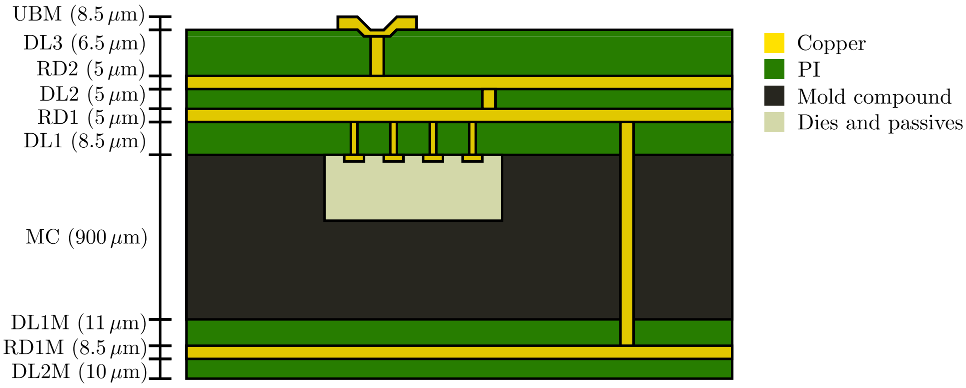

Figure 3.6: Package stackup and materials.

The resonant frequencies, f_0, of the antennas are obtained in HFSS by searching the zero-crossing points of the imaginary part of the input impedance. The resulting resonant frequencies obtained by the aforementioned procedure are plotted in Fig. 3.7. The radiation efficiencies are evaluated at the resonant frequency of the antenna and are shown in Fig. 3.8. Since the transmission-line model of [30] is developed for usage in vacuum, a divergence is expected when compared to HFSS simulations since lossy dielectric materials are present around the antenna. The plot of Fig. 3.7 is obtained for an effective dielectric permittivity (ε_{eff}) of 1.9 of the transmission line formed by the adjacent meander arms. Nonetheless, for the case of six or eight meanders the agreement deteriorates. This may be due to the fact that other geometries of the meander-line result in a different effective permittivity that differs from $\varepsilon_{eff} = 1.9$.

From Fig. 3.7 it can be seen that a good agreement between the theoretical model and the HFSS simulation exists when up to four meanders are used. In addition if we also consider the radiation efficiency in Fig. 3.8, it can be seen that four meanders offer a good trade-off between radiation efficiency and resonant frequency of the antenna. This geometry is the starting point for the approach described in the next section.

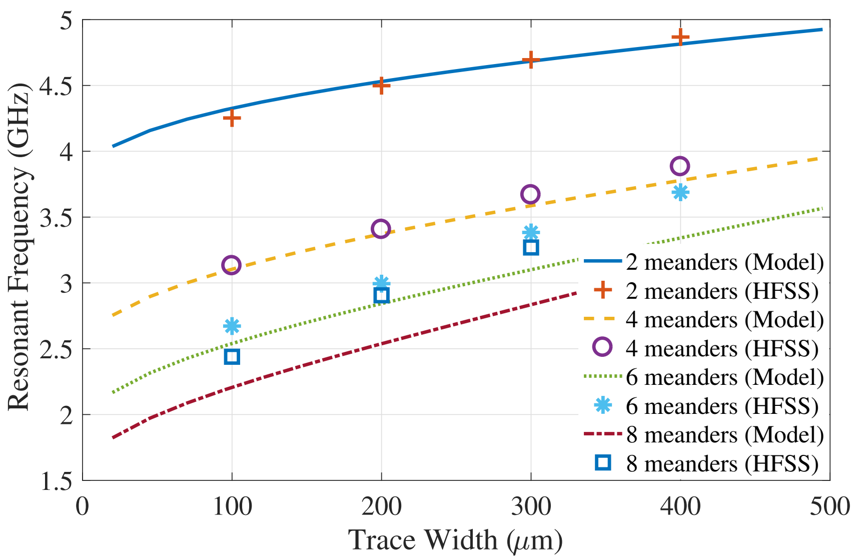

Figure 3.7: Comparison of the resonant frequencies of the studied meander-line antennas as given by the transmission line model and the HFSS simulations.

3.3.1.3 Inductively Loaded Meander-Line

Given the choice of four meanders, a trace width of 100 µm results in an efficiency of 50 %, corresponding to a resonant frequency of 3 GHz. Hence, additional tuning procedures are needed and these are discussed in this section.

The inductive loading technique has been extensively explored in literature and shown to significantly reduce the size of antennas [32–34]. Specifically, if an inductor is placed in one of the meander arms, the desired resonant frequency of 2.44 GHz can be obtained. Furthermore, matching the input of the radiating element to 50 Ω is of utmost importance, since it is known that electrically-small antennas usually show a low input resistance. A common method for improving

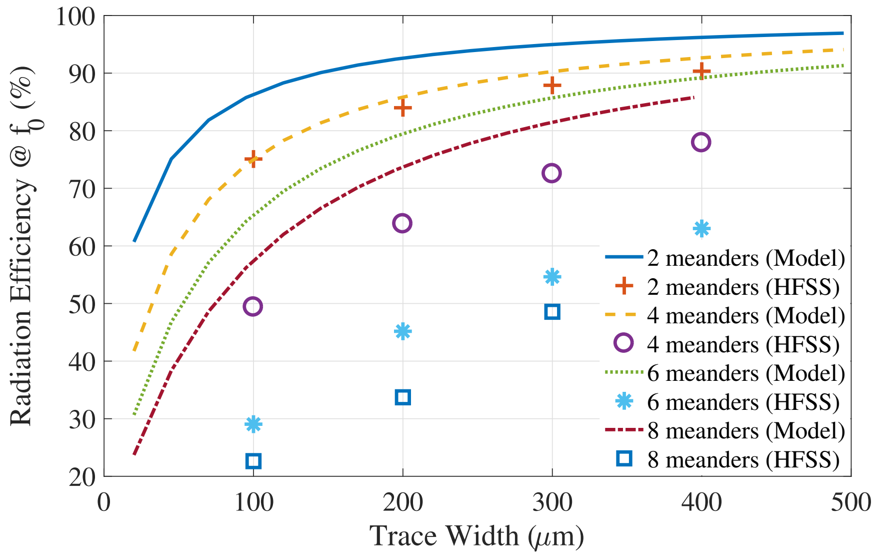

Figure 3.8: Comparison of the radiation efficiencies of the studied meander-line antennas as given by both the transmission line model and HFSS simulations.

matching when low input resistances are present is the usage of inductive coupling, which acts as an impedance transformer [35–37].

To design the antenna based on this methodology, the setup of Fig. 3.9 was assembled in HFSS. The ground plane is composed of two planes in RD1 and RD2 metal layers, connected with vias. The meander line monopole is designed in RD2 layer and shorted to ground at what would be its feeding point. It is driven by the coupling of magnetic field created by the loop in RD1. The inductor itself may be a chip inductance and placed in the mold compound or designed in the available metallization layers. In this instance, an impedance layer is set in HFSS to model the tuning inductance and reduce simulation time. The corresponding inductor is later designed in RD1 and RD2 metal layers for the final layout.

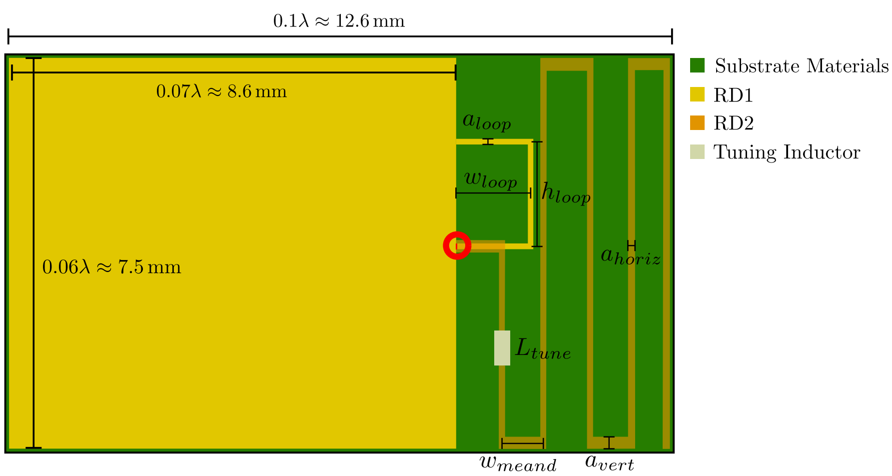

Figure 3.9: Simulation model of the meandered antenna illustrating the tuning loop.

In Table 3.2 the design variables, their initial and final values after the tuning process are given. The non-radiative arms, which form the twin conductor transmission lines discussed before, are initially chosen to be narrower than the radiative arms to reduce the need for large tuning inductance, *i.e.* more self inductance from the meander-line. On the contrary, the radiative arms are chosen to be slightly wider, in order to reduce loss resistance and improve efficiency. The objective of the tuning process in HFSS is to obtain 50 Ω input impedance at the highest possible realized gain. This process is made by running a gradient based optimizer on the initial values shown in Table 3.2.

Table 3.2: Initial and final design variables after tuning process in HFSS.

Design Variable	Initial Value	Final Value
a_{loop}	100 µm	100 µm
w_{loop}	1500 µm	1400 µm
h_{loop}	2000 µm	1950 µm
a_{horiz}	50 µm	37.5 µm
a_{vert}	250 µm	235 µm
w_{meand}	800 µm	800 µm
L_{tune}	1.5 nH	2.4 nH

In Fig. 3.10 the results of the tuning process of the inductor are shown. It can be seen that the resonant frequency can be easily adjusted by varying the inductance value. Furthermore, it can be seen that the required −6 dB bandwidth is fulfilled when $L_{tune} = 2.4$ nH. With an ideal inductance, the simulated peak efficiency of the antenna is $e_{rad} = 15.9$ %. The current distribution of the antenna is shown in Fig. 3.11, where the radiating currents in the ground plane can be seen.

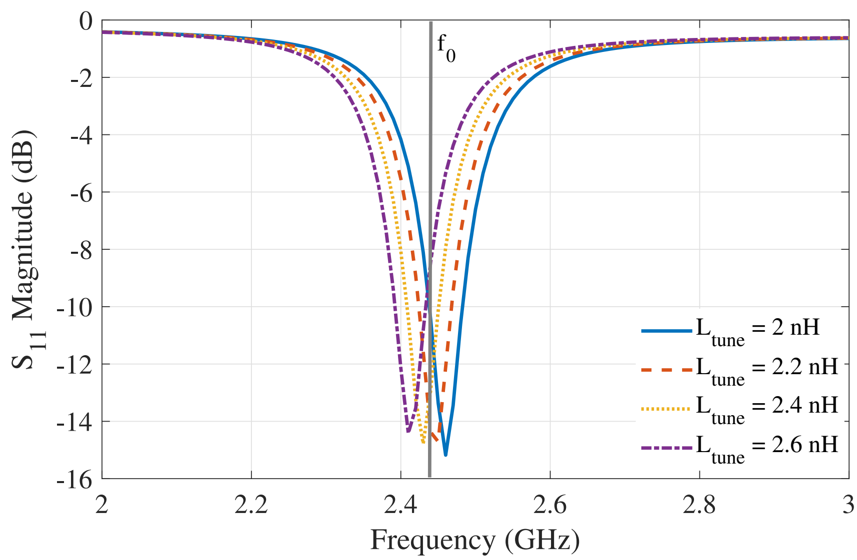

Figure 3.10: Simulated results of the S_{11} comparing varying inductances, L_{tune}.

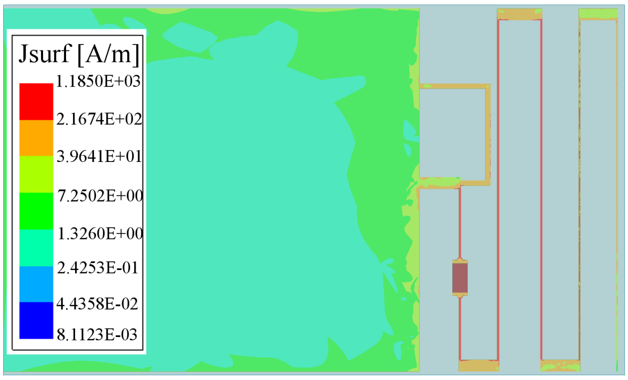

Figure 3.11: Simulated antenna current distribution.

The -10 dB bandwidth of approximately 80 MHz observed in Fig. 3.10 can be seen to be lower than the one derived in 3.3.1.1, shown in Fig. 3.3. This discrepancy can be justified by the reduced ground plane, which greatly increases the antenna Q and reduces the radiation efficiency. Such can be understood by the equivalent model represented in Fig. 3.12, where the capacitor of the series RLC circuit models the distributed capacitance between the antenna and the ground plane. This capacitor increases when the ground plane is larger. This results in a reduction of the quality factor of the resonant circuit, since we know that $Q = \sqrt{L/(CR^2)}$ for a series RLC at its resonant frequency. The equivalent circuit values are $L_{loop} = 8$ nH, $L_{ant} = 5.03$ nH, $k = 0.3158$, $C_{ant} = 934.5$ fF and $R_{ant} = 1.9\,\Omega$ can be obtained through tuning methods in ADS. These values give a good agreement as seen in Figs. 3.13 and 3.14, where the S_{11} magnitude and phase are shown for both the HFSS simulation and the equivalent circuit. A divergence can be seen at frequencies higher than the first resonance due to the fact that the second resonant mode of the meander-line antenna is not modelled in the circuit.

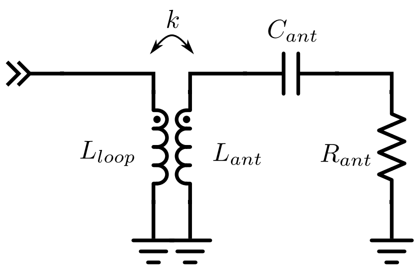

Figure 3.12: Inductively coupled meander-line antenna equivalent circuit.

3.3.2 Experimental Evaluation

To validate our design and simulation approach, the antennas are manufactured and measured. In their fabrication, the multiple dies that compose the Bluetooth system-inpackage were already embedded in the package. Both the input reflection coefficient and radiation pattern were measured.

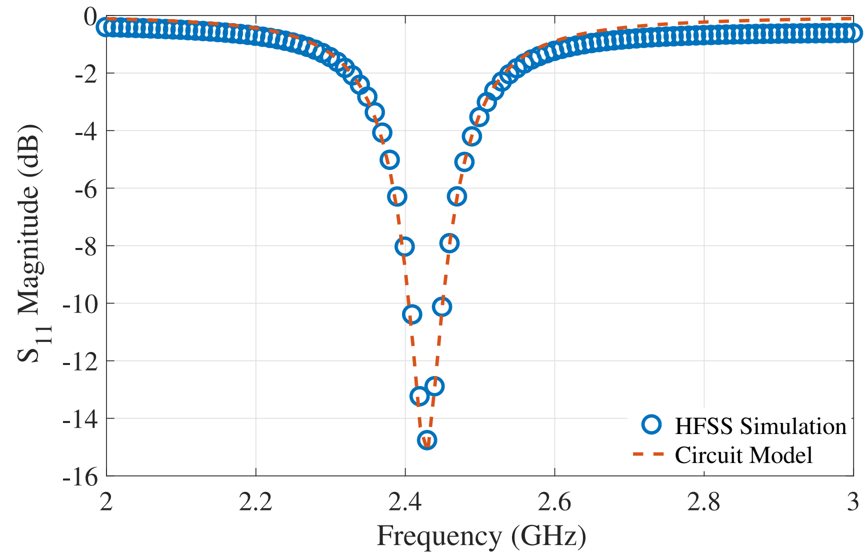

Figure 3.13: S_{11} magnitude comparison between equivalent circuit model and HFSS simulation.

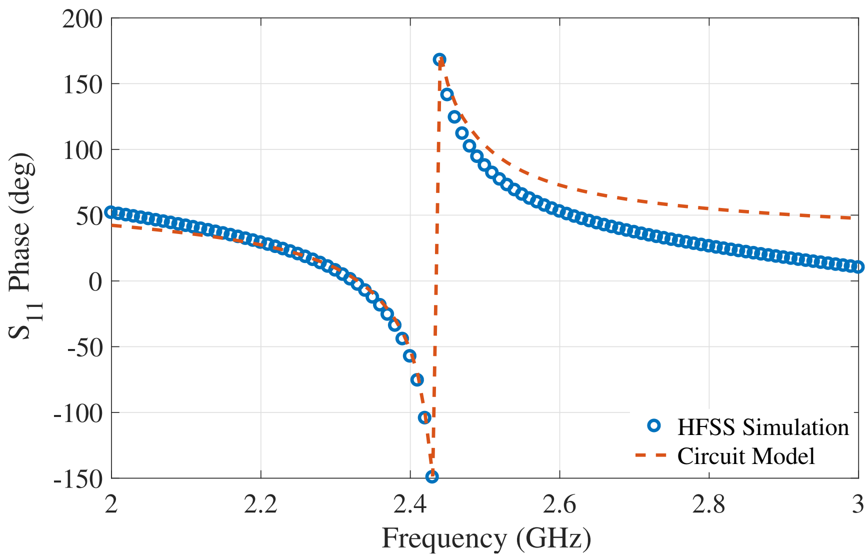

Figure 3.14: S_{11} phase comparison between equivalent circuit model and HFSS simulation.

3.3.2.1 Input Reflection Coefficient Measurement

In order to measure the input reflection coefficient of the antenna, the setup of Fig. 3.15 is assembled, where a miniature anechoic chamber composed of flat absorbers can be seen. A close-up of the PicoProbe ground-signal probe (10-50/30-125-W-2-R-800 micron) near the antenna is also depicted in the measurement setup of Fig. 3.15. The probe was previously calibrated using a PicoProbe CS-11 SOLT calibration kit. In the sample under test, the Bluetooth chip is disconnected from the antenna, so that the antenna can be analysed standalone. For the measurement an HP8753ES vector network analyser is used.

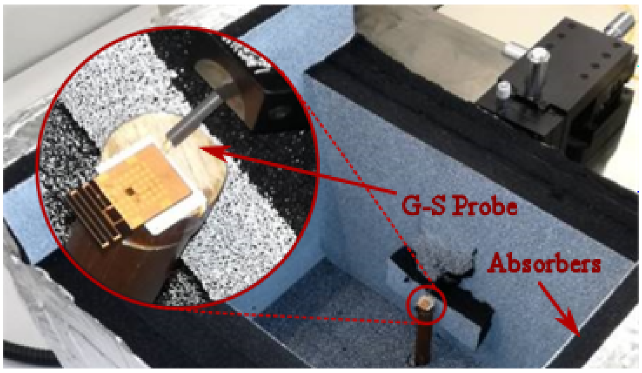

Figure 3.15: Measurement setup for obtaining the reflection coefficient.

Fig. 3.16 shows both the simulated and measured results comparing the S_{11}, from which a good agreement between the simulated and experimental results can be seen. The bandwidth measured experimentally is larger than the value estimated theoretically, which can be explained by the fact that the dies are present alongside the antenna on the package. Since most of them are made of doped silicon they introduce additional dielectric losses which decrease the Q factor and increase the bandwidth. The dies were not accounted for in simulation due to impractical simulation time. Another reason for the difference between the simulated and measured result is the additional ground provided by the coax G-S probe, which extends the ground plane of the antenna leading to higher radiation losses, which again contributes to an increased measured bandwidth.

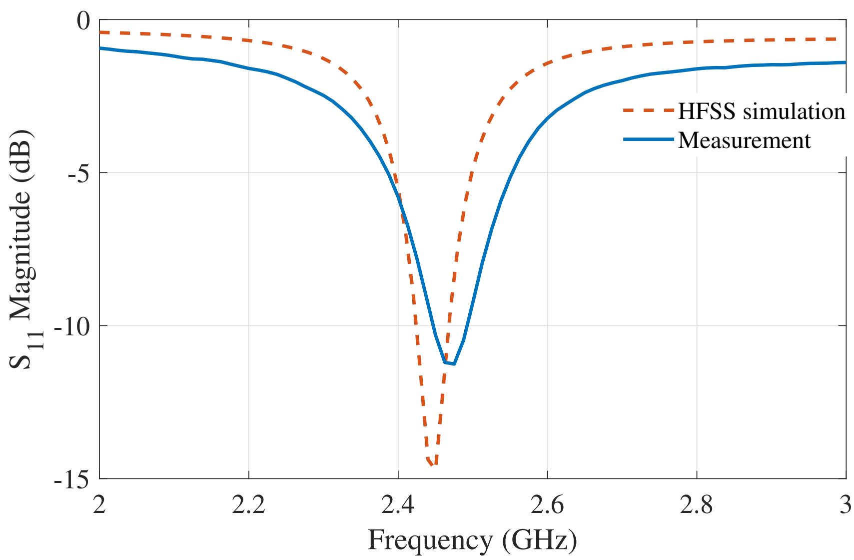

Figure 3.16: S_{11} magnitude comparison between HFSS simulation and measurement.

3.3.2.2 Radiation Pattern Measurement

Since using a probe station attached to an antenna is undesirable while it is being rotated, a different approach to measure the antenna has been used, as follows. A battery is connected to a fully functional system-in-package through a twisted pair to mitigate interferences. The sample is pre-programmed to transmit 0 dBm continuously at 2.42 GHz and placed in an antenna positioner in the anechoic chamber. In the other end of the chamber a calibrated antenna and cable are connected to a Keysight N9030A spectrum analyser. A schematic of the setup used to measure the radiation pattern is shown in Fig. 3.17. Fig. 3.18 shows the SiP placed in a support on the positioner inside the anechoic chamber ready for the measurement process. By knowing the distance between the antenna under test (AUT) and the calibrated antenna d, plus the gain of the latter G_{cal} and the loss on the coaxial cable connecting the calibrated antenna and spectrum analyser L_{coax}, the AUT gain is known by reading the power received on the spectrum analyser and applying

$$G_{AUT} = P_{rx} - P_{tx} - G_{cal} + L_{coax} - 20\log\left(\frac{\lambda}{4\pi d}\right) \tag{3.19}$$

which is based in Friis transmission equation [12, pp. 90]. In equation (3.19), P_{rx} denotes the power read in the spectrum analyser, P_{tx} the power at the AUT input provided by the Bluetooth IC and λ the free-space wavelength corresponding to the frequency at which the measurement is taken. Considering $d = 4.4\,\text{m}$, $G_{cal} = 9\,\text{dBi}$, $P_{tx} = 0\,\text{dBm}$, $L_{coax} = 12\,\text{dB}$ and $P_{rx} = -64.76\,\text{dBm}$ at the direction where peak gain occurs, the AUT peak gain can be calculated as $G_{AUT} \approx -8.7\,\text{dBi}$. However, it is important to note that an unquantifiable error exists because of the uncertainty on the output power delivered by the Bluetooth IC.

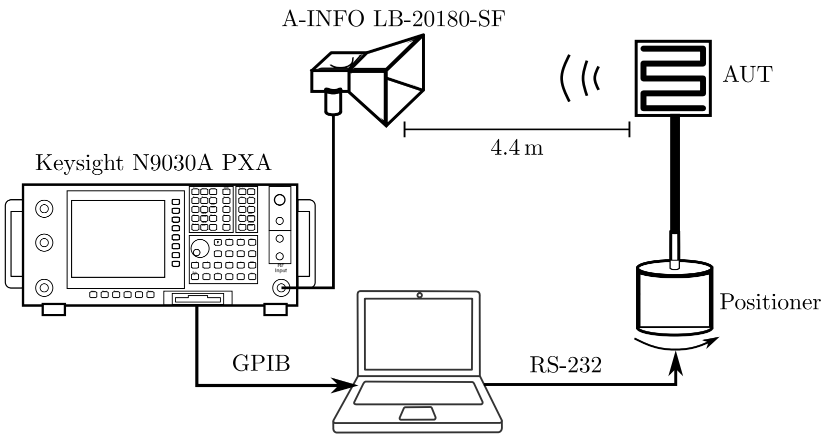

Figure 3.17: Schematic representation of the antenna measurement setup obtaining a radiation pattern.

The measured and simulated E-plane and H-Plane radiation patterns are shown in Figs. 3.19 and 3.20, respectively. A torus shaped pattern of a dipole is seen in the simulation result as expected due to the reduced ground plane. The peak realized gain obtained in HFSS simulation is circa −6 dBi. The measured radiation pattern deviates from simulation, which is attributed to the wires that connect from the package to the battery. The additional losses occur both due to the battery circuit and the doped silicon substrates in close proximity of the antenna. Such was verified by simulating the antenna with increased loss tangent in the region of the MC where these ICs lie plus the battery wires with 80 mm length. A radiation pattern deformation was verified as

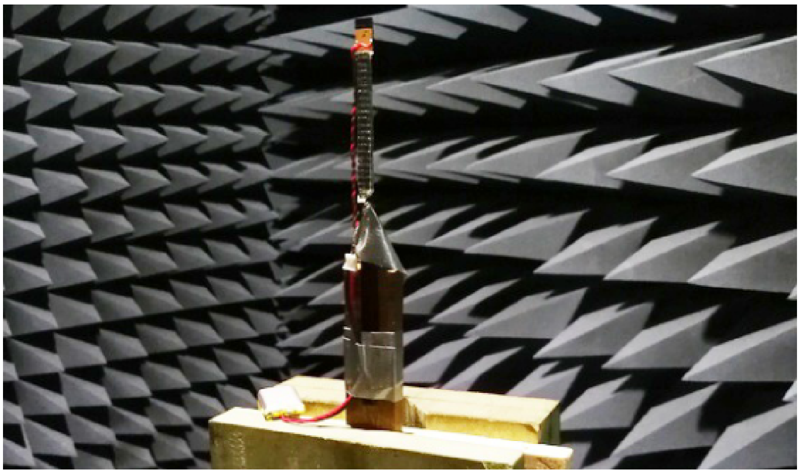

Figure 3.18: System-in-package connected to battery, transmitting continuous wave and placed on antenna positioner.

shown in Figs. 3.19 and 3.20 with the red trace. Nonetheless, the experimental results demonstrate and validate the design methodology, as the initial requirement is still met and when the battery connection wires are simulated the agreement improves.

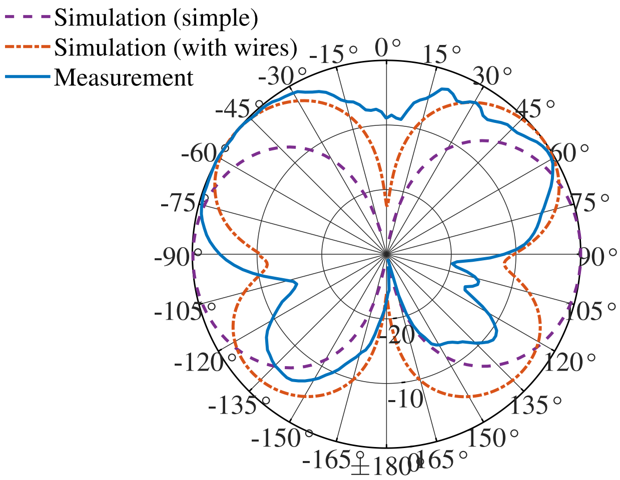

Figure 3.19: Normalized simulated and measured E-Plane radiation patterns at 2.42 GHz.

3.4 Summary

In this chapter a miniaturized inductively loaded meander-line monopole was implemented and a methodology successfully demonstrated for the design of an electrical small antenna with a *ka* factor of 0.5. The agreement between the measurements and the simulation results validated the proposed antenna. It was proven that the integration of antennas and integrated circuits in a single package is feasible for the frequency band used in Bluetooth Low Energy. Notwithstanding, the

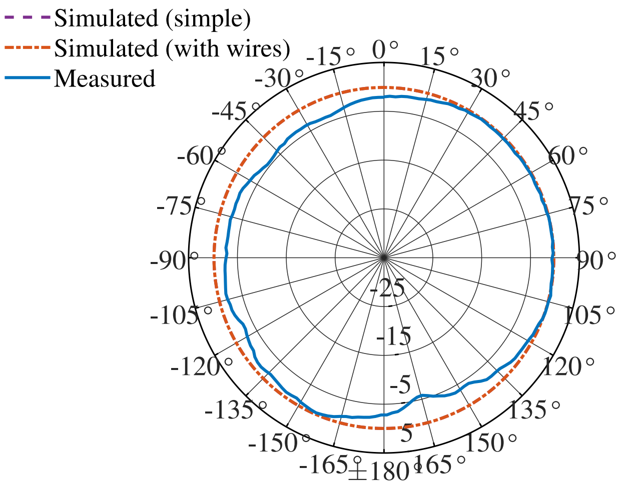

Figure 3.20: Normalized simulated and measured H-Plane radiation patterns at 2.42 GHz.

measured results reveal some discrepancies on the radiation pattern and additional losses. The source was identified to be the doped silicon substrates that are present inside the SiP, plus the external wires that are needed for power connection.

To mitigate the influence of the power supply connection wires, a bias-tee may be designed in the future to prevent RF common-mode signals from travelling on them and contributing to radiation. The ICs can be accounted for in a final simulation of the design, but the simulation time rises considerably. Therefore, it is still not feasible to tune such an antenna considering all the ICs present inside the package.

Chapter 4

Dual-Polarized Patch Antenna-in-Package for K-Band 5G Communications

4.1 Introduction

The european 5G communication band in the frequency range from 24.25 to 27.5 GHz is settled as the most adequate solution for limited coverage and high throughput scenarios [5]. Its usage drives the need for new antenna technologies capable of beamforming, polarization diversity and large bandwidths. Patch antennas are well known in the literature for their simple design, easy and cheap manufacturing. Additionally, they support multiple feeding techniques, some of which enhance their bandwidth. Furthermore, they are able to support orthogonal modes which allows the radiation of two polarizations with a single antenna. These features make the patch antenna the best candidate for a dual-polarized antenna which is cheap to fabricate and can have a relatively broad bandwidth, as is needed in 5G K-band communications. However, this type of antenna usually presents a narrow fractional bandwidth which is incompatible with the needed bandwidth for 5G K-band communications. In this chapter a solution with dual polarization and isolations on the order of 40 dB throughout the full bandwidth is shown. A differential feeding technique and a heuristic based design of a matching network are also presented.

4.2 Patch Antennas

Considering the equivalent transmission line model of a patch antenna, which considers it as an half-wave microstrip resonator shown in Fig. 4.1, one can calculate the antenna dimensions for a particular design frequency, given the substrate height h and dielectric constant ε_r. The patch is seen as a microstrip line whose width should be given as [12, pp. 791]

$$W = \frac{1}{2f_0\sqrt{\mu_0\varepsilon_0}}\sqrt{\frac{2}{\varepsilon_r+1}} \tag{4.1}$$

where f_0 denotes the desired resonant frequency. As this microstrip line is wide enough for radiation to occur and the substrate is thin enough for substrate modes and surface waves to be absent [12, pp. 789], one can calculate its effective dielectric constant as

$$\varepsilon_{reff} = \frac{\varepsilon_r+1}{2} + \frac{\varepsilon_r-1}{2}\left[1+12\frac{h}{W}\right]^{-1/2} \tag{4.2}$$

Given the effective dielectric constant of the microstrip line, the fringing field extension ΔL can be given as

$$\Delta L = 0.412\cdot h\frac{(\varepsilon_{reff}+0.3)(\frac{W}{h}+0.264)}{(\varepsilon_{reff}-0.258)(\frac{W}{h}+0.8)} \tag{4.3}$$

This allows us to calculate the actual patch length as

$$L = \frac{1}{2f_0\sqrt{\varepsilon_{reff}}\sqrt{\mu_0\varepsilon_0}} - 2\Delta L \tag{4.4}$$

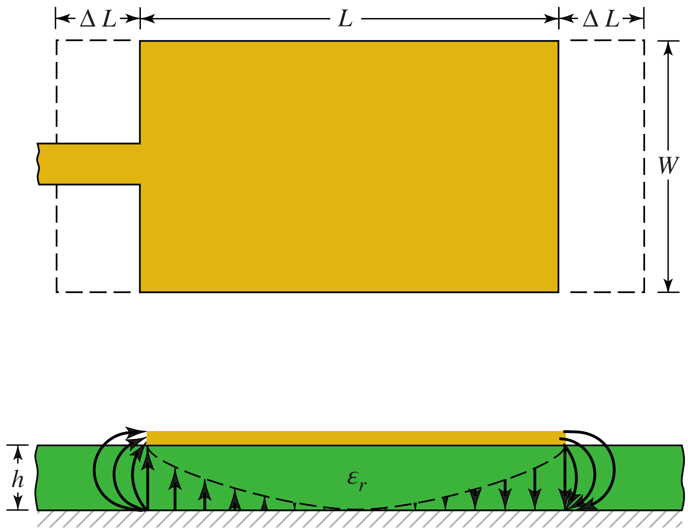

Figure 4.1: Fundamental mode half-wave microstrip resonator model of patch antenna [12, pp. 790].

This type of antennas can be fed in a variety of ways as shown in Fig. 4.2. In the case of microstrip and probe feeds, the feeding method is direct. However, due to the microstrip discontinuity and probe length, a stray inductance develops which can be hard to compensate in probe feed, mostly in thicker substrates. Slot feed can be seen as the coupling of two resonant systems, the slot and the patch antenna itself. This feeding method allows more degrees of freedom for

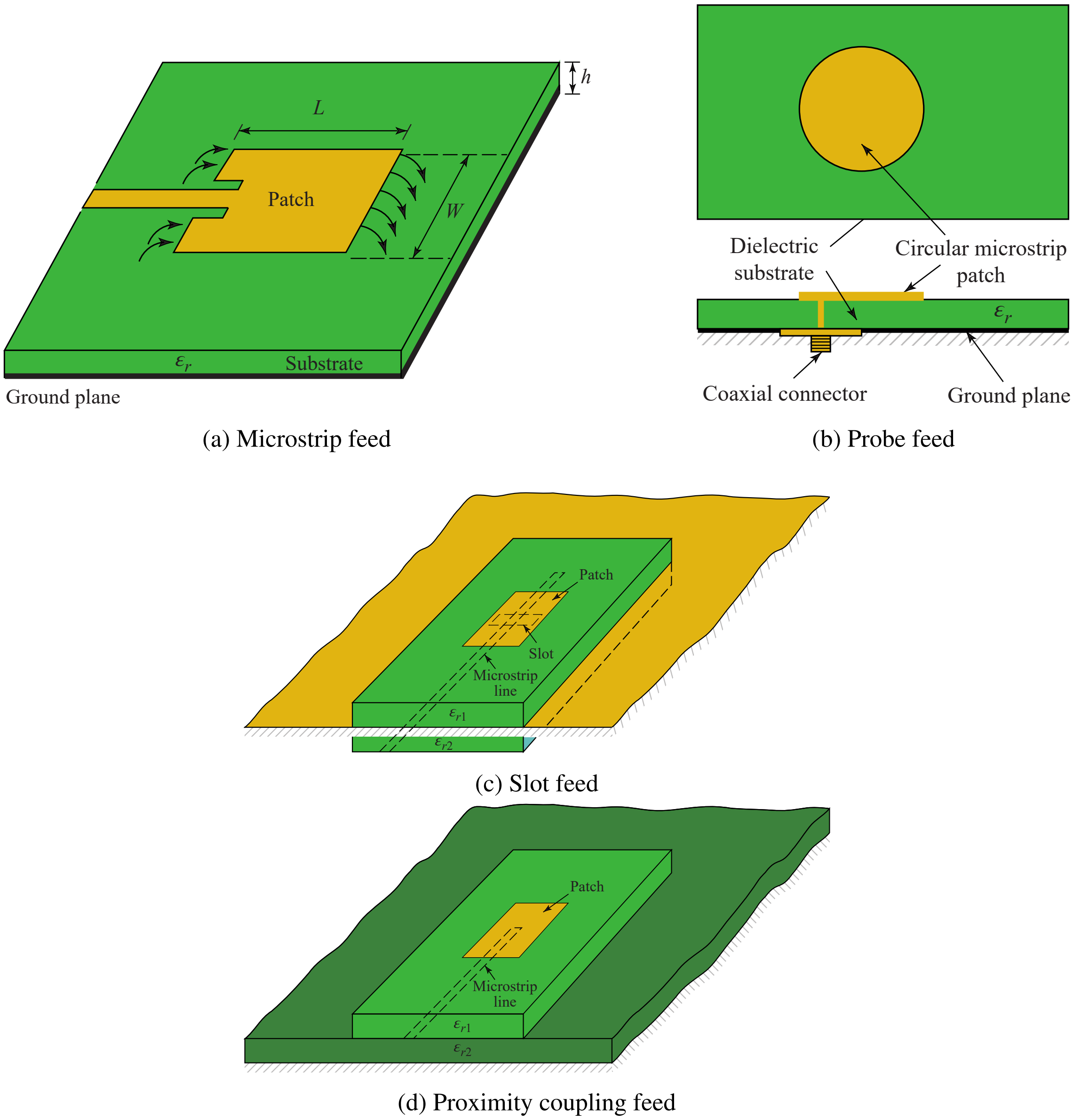

Figure 4.2: Feeding methods for patch antennas [12, pp. 786].

tuning and is able to provide wider bandwidths. However, if the slot size needs to be electrically large, backside radiation will start developing which distorts the patch radiation pattern and degrades the front-to-back ratio. Proximity coupling feed is also an indirect feeding method as slot feed. It can also be seen as the coupling of two resonant structures but instead of inductive coupling, they couple through capacitive means. Both these methods are able to provide wider impedance bandwidths but the final end result is the need for higher layer counts which increases fabrication costs.

4.3 Antenna Design

As stated in the previous section, patch antennas suffer from bandwidth limitations. The most common solution found in the state-of-the-art to overcome them is the usage of a stacked patch topology [7, 38], as seen in Fig. 4.4. However, such technique usually leads to higher order modes which will degrade radiation pattern stability throughout the band of operation [39, pp. 163]. Furthermore these higher order modes also compromise isolation in dually-polarized antennas. As it is discussed in [40], a different patch topology had to be used to improve isolation between polarizations.

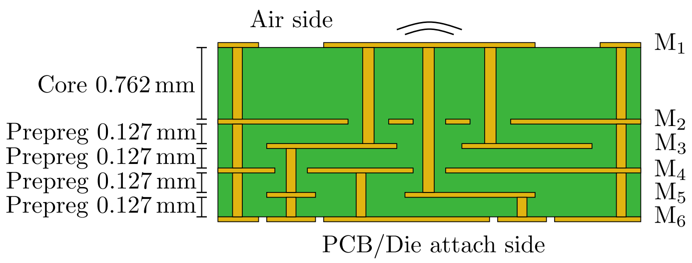

Figure 4.3: Antenna stackup.

To reduce the layer count and the manufacturing costs a probe-fed patch with parasitic elements in the same layer to improve its bandwidth, as reported in [41, pp. 110], is used. Furthermore, based on [42, 43], a differential feeding technique is utilized. By doing this, each mode is excited with two feeds with opposing phases, which cancel out higher order modes, reduce feed radiation and reinforce the fundamental degenerate modes TM_{010} and TM_{100} of the patch antenna. Ultimately, this improves isolation between polarizations and radiation pattern stability.

As dual polarization is desired in the patch antenna of this chapter, a modification to the calculation of the patch dimensions has to be made. Making $W = L$ results in a square patch which in turn makes the two orthogonal modes TM_{010} and TM_{100} to be degenerate, that is to have the same resonant frequency when considering the cavity model of the patch antenna. However, it also results in an equation with no analytical solutions, if we try to solve for the resonant frequency of the antenna. Therefore a numerical approach has to be used to determine the initial patch size. The antenna stackup for land-side die attach packaging is shown in Fig. 4.3, where a Rogers RO4350B ($\varepsilon_r = 3.48$) core was used with Rogers RO4450T prepreg ($\varepsilon_r = 3.35$). These substrates offer a good compromise between cost, moderate permittivity values and low losses ($\tan\delta \approx 0.004$). The metal layers are all composed of 17.5 µm thick copper. Since the patch has to be rotationally symmetric for both polarizations to have the same resonant frequency, we have $W = L$. The remaining calculation variables for obtaining the resonant frequency as a function of $W = L$ are $h = 0.762$ mm and $\varepsilon_r = 3.48$, since the patch is designed in M_1 layer, being M_2 the ground plane. To obtain the length and width of the rotationally symmetric patch $L = W$ a simple patch length was first calculated using the method described in 4.2. The result of such calculation can then be used as the initial guess of a Newton algorithm approach as described in [44]. The

Newton algorithm in this case was set to obtain the root of the objective function

$$f(L) = f_0 - \frac{1}{2(L+2\Delta L)\sqrt{\varepsilon_{reff}}\sqrt{\mu_0\varepsilon_0}} \tag{4.5}$$

where $f_0 = 26\,\text{GHz}$ is the desired resonant frequency. The values for ε_{reff} and ΔL can be obtained during the algorithm from equations (4.2) and (4.3), respectively by making $W = L$. Using this algorithm a resonant frequency of $f_0 = 26\,\text{GHz}$ was obtained for a patch size of $W = L \approx 2.75\,\text{mm}$.

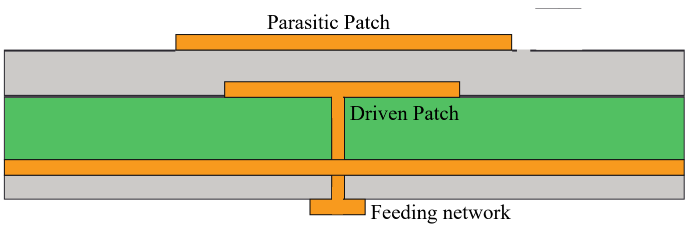

Figure 4.4: Example of parasitic patch antenna topology.

The patch and its parasitics for bandwidth enhancement are designed in M_1 metal layer, as shown in Fig. 4.5. The vertically polarized stream (port 1) is fed from M_3 and the horizontal (port 2) from M_5 metal layer. In each feeding network a lossless half-wavelength $50\,\Omega$ transmission line was connected between the two corresponding balanced ports to obtain the needed 180° phase shift for differential feeding. Another $50\,\Omega$ lossless line was connected to one of the balanced ports in each polarization, to evaluate the single-ended reflection coefficient. Considering the previously calculated patch size, it was set to $ps = 2.75\,\text{mm}$. As stated in [41, pp. 110], optimization is needed on determining the size of the parasitics and their distance to the driven patch, which should be kept $pg < 2.5h$. The design of [41, pp. 110] was scaled down for our patch size and used as an initial guess of a gradient based optimizer combined with the Method of Moments simulation in ADS. The objective was to maximize the bandwidth centred at 26 GHz in both ports. After optimization, the values of $ps = 2.75\,\text{mm}$ (patch size), $fo = 0.8\,\text{mm}$ (probe feed offset from patch centre), $pl = 1.7\,\text{mm}$ (parasitic length), $pw = 1.2\,\text{mm}$ (parasitic width), $pg = 0.1\,\text{mm}$ (parasitic gap) resulted in the plot of Fig. 4.6, where a low reflection coefficient at the centre frequency of 26 GHz, was obtained at both ports. However, a limited bandwidth of approximately 2.5 GHz can be verified, which falls short from the needed 3.25 GHz.

Because of the bandwidth limitation a matching network has to be designed. Since the transition from the antenna feeding networks to the PCB presents some parasitics, the matching network must be designed after such transition is modelled.

4.4 PCB-to-Package Transition

The transition between the hosting PCB and the antenna-in-package is designed as shown in the 3D model of Fig. 4.7. The transition is simply a connection between a microstrip on the host PCB and a stripline with via stitching on M_5 layer of the package. To connect to the feeding network

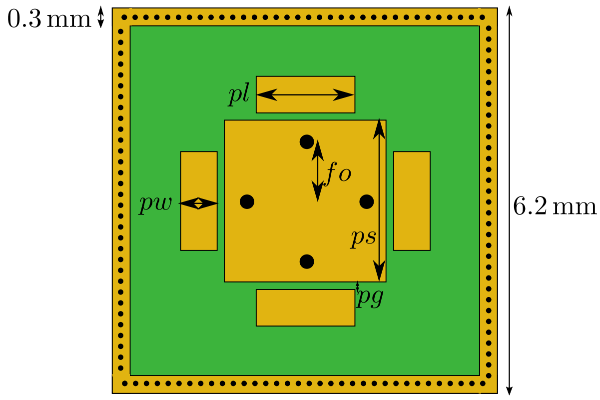

Figure 4.5: Antenna layout.

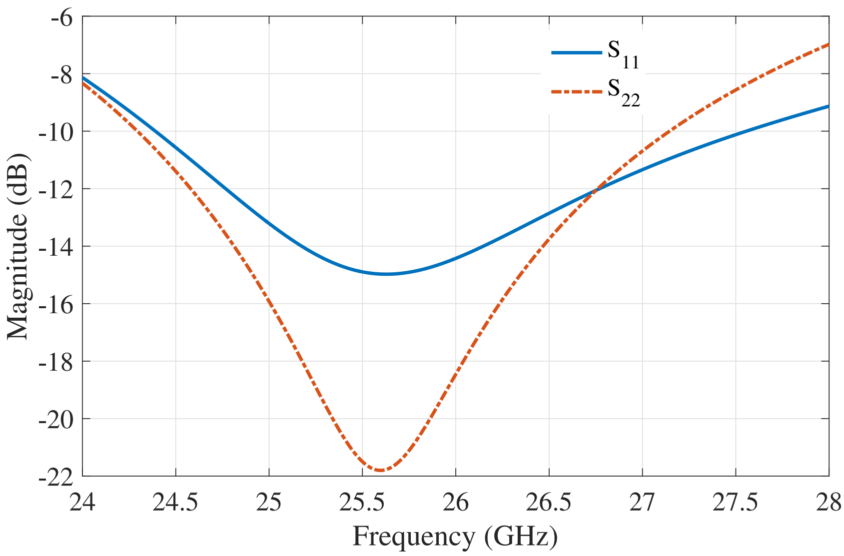

Figure 4.6: S_{11} and S_{22} magnitudes as a function of frequency for the patch antenna without matching network.

on M_3 an internal transition between M_5 and M_3 was required to be designed as well. Port 1 is placed in the microstrip on the PCB and port 2 in the stripline inside the package.

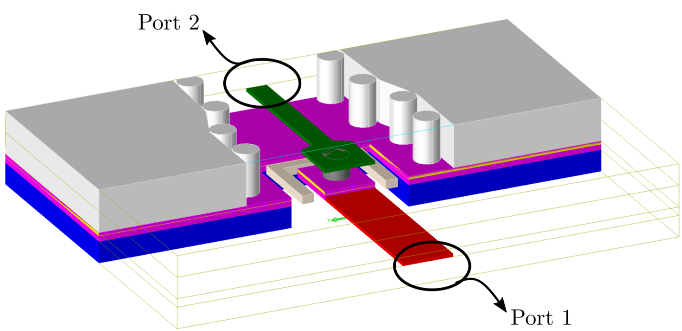

Figure 4.7: PCB to package transition.

According to [45, pp. 148], the microstrip dimensions for a certain impedance Z_0 can be obtained by calculating two factors A and B as

$$A = \frac{Z_0}{60}\sqrt{\frac{\varepsilon_r+1}{2}} + \frac{\varepsilon_r-1}{\varepsilon_r+1}\left(0.23 + \frac{0.11}{\varepsilon_r}\right) \tag{4.6}$$

and

$$B = \frac{377\pi}{2Z_0\sqrt{\varepsilon_r}} \tag{4.7}$$

which have to be plugged in

$$\frac{W}{d} = \begin{cases} \frac{8e^A}{e^{2A}-2} & \text{for } W/d > 2 \\ \frac{2}{\pi}\left[B - 1 - \ln(2B-1) + \frac{\varepsilon_r-1}{2\varepsilon_r}\left\{\ln(B-1) + 0.39 - \frac{0.61}{\varepsilon_r}\right\}\right] & \text{for } W/d < 2 \end{cases} \tag{4.8}$$

where W is the microstrip width and d the substrate height. To obtain the stripline width, according to [45, pp. 143], one can write

$$\frac{W}{b} = \begin{cases} x & \text{for } \sqrt{\varepsilon_r}Z_0 < 120 \\ 0.85 - \sqrt{0.6 - x} & \text{for } \sqrt{\varepsilon_r}Z_0 < 120 \end{cases} \tag{4.9}$$

where b is the substrate height, Z_0 the desired characteristic impedance and

$$x = \frac{30\pi}{\sqrt{\varepsilon_r z_0}} - 0.441 \tag{4.10}$$

These formulas for stripline assume that the transmission line is of zero thickness and that it sits in the exact centre of the two ground planes. The latter assumption can be considered as acceptable given the stackup of Fig. 4.3. However, since the stripline in the real cases has no zero thickness, its impedance was optimized in ADS Controlled Impedance Line Designer as shown in Fig. 4.8.

After FEM simulation in ADS, the S-parameters plotted in Figs. 4.9 and 4.10 were obtained where it can be seen that an acceptable return and insertion losses were obtained which leads to the conclusion that this as a valid transition.

4.5 Final Assembly

Due to the reduced bandwidth obtained in the modelling described in section 4.3, the patch antenna is re-optimized to achieve peak gain instead of maximizing impedance bandwidth, as matching networks will later be connected for each polarization. The resulting values for peak gain obtained after the gradient based optimizer are $ps = 2.83$ mm, $fo = 0.8$ mm, $pl = 1.7$ mm, $pw = 0.7$ mm, $pg = 0.1$ mm. Matching networks are later introduced to obtain $50\,\Omega$ input impedance at the package input.

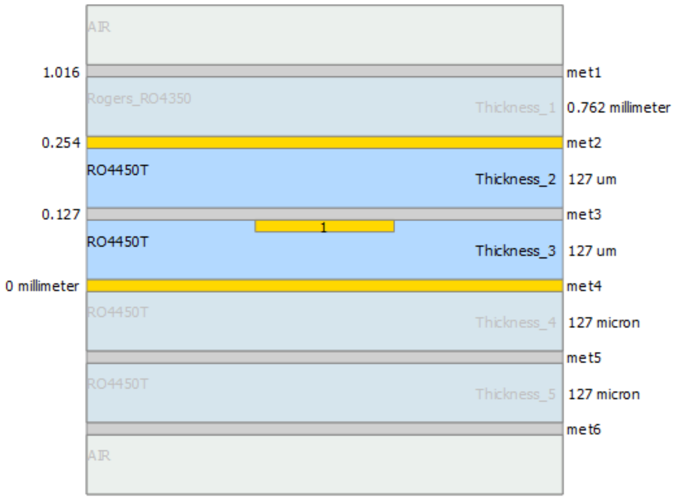

Figure 4.8: ADS Controlled Impedance Line Designer setup for obtaining stripline dimensions.

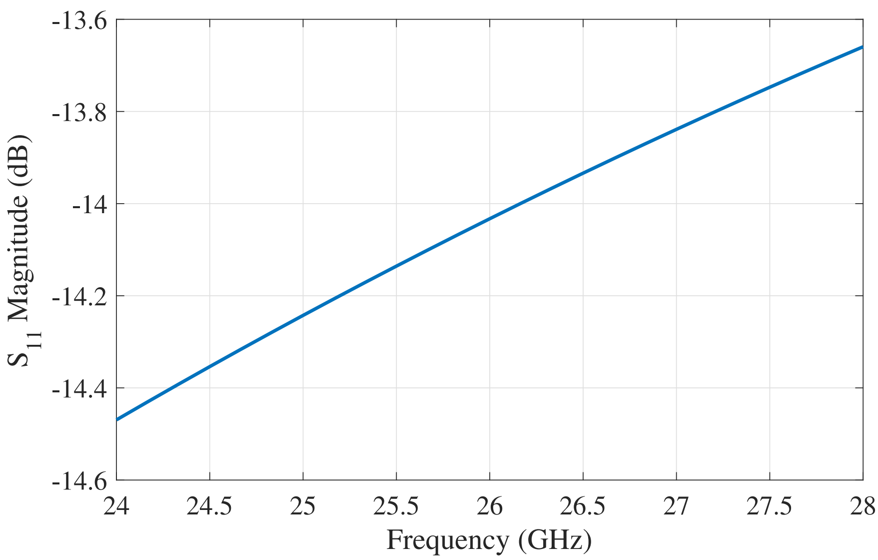

Figure 4.9: S_{11} magnitude as a function of frequency for the microstrip input of the PCB (port 1) to package stripline transition (port 2).

In [46] a method with a dual-frequency impedance transformer, composed of two arbitrary cascaded transmission lines, was reported to match complex impedances in a wide bandwidth. The proposed matching network circuit for the antenna is shown in Fig. 4.11, where two cascaded transmission lines and two reactance cancellation stubs can be seen. The values of the electrical parameters for both matching networks are obtained by resorting to a particle swarm optimizer (PSO) algorithm, because the method reported in [46] does not consider load impedance variation with frequency, therefore rendering analytical calculations useless for our case. The upper bound for the impedance of each transmission line is obtained by calculating the characteristic impedance of a stripline with the minimum trace width of 100 µm, for easier fabrication. This impedance was

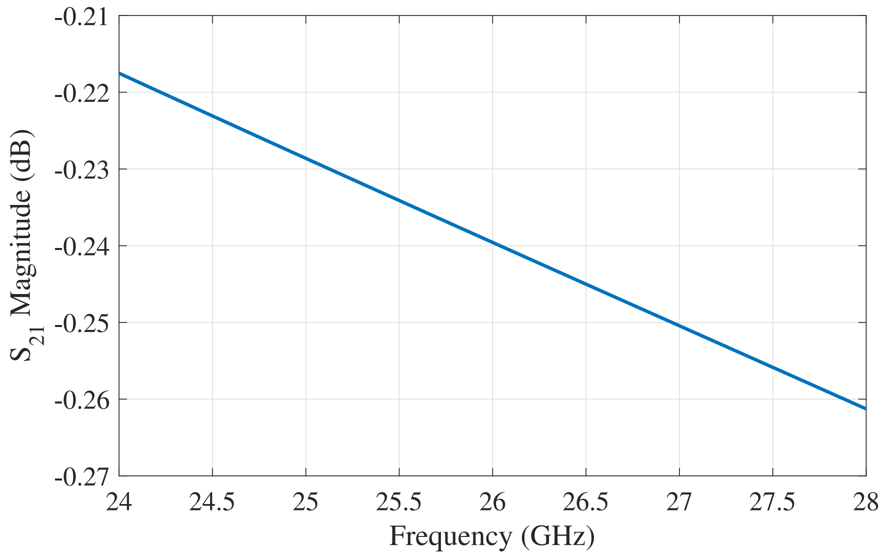

Figure 4.10: S_{21} magnitude as a function of frequency for the microstrip input of the PCB (port 1) to package stripline transition (port 2).

calculated using ADS Controlled Impedance Line Designer and the value obtained was $Z_{max} = 53.8\,\Omega$. The remaining PSO parameters are defined as recommended in [47], where the number of particles $N = 100$, the social and cognitive coefficients $c_1 = c_2 = 2$ and the inertia coefficient $w = 1$. The objective function is defined so that its value reduces as more simulation points for the magnitude of the S_{11} are below the $-10\,\text{dB}$. Mathematically, this can be described as summing all the points that lie above the $-10\,\text{dB}$ line and therefore are unmatched. The objective function can be normalized by dividing the sum of points above $-10\,\text{dB}$ and dividing by the total simulated points k. In mathematical terms we can write

$$OF = \frac{1}{k}\sum_{i=1}^{k} a_i \tag{4.11}$$

where i denotes the index of the simulation point corresponding to a simulation frequency within the considered span of 24.25 to 27.5 GHz and a_i is given as

$$a_i = \begin{cases} 0 & \text{for } |S_{11i}|_{\text{dB}} < -10 \\ 1 & \text{for } |S_{11i}|_{\text{dB}} \geq -10 \end{cases} \tag{4.12}$$

in which S_{11i} denotes the simulated reflection coefficient at frequency index i. After optimization the values for the transmission line electrical parameters are obtained as given in Table 4.1 for both the V-Pol and H-Pol inputs of the antenna. Despite the rotational symmetry of the antenna, the matching networks have to be different because of an added transition between M_3 and M_5 metal layers, which results in an asymmetric S-parameter matrix. This transition serves as a connection between M_3 layer and the package to PCB transition.

The final layout is presented in Fig. 4.12, where the values of Table 4.1 were mapped to

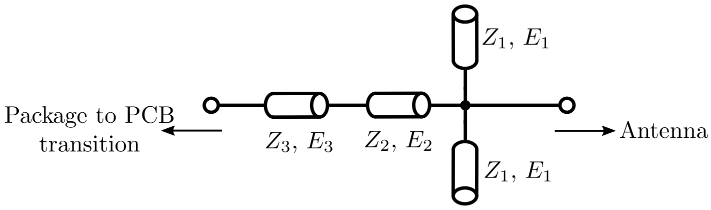

Figure 4.11: Matching network schematic.

Table 4.1: Matching network transmission line electrical parameters at the centre frequency of 26 GHz.

Polarization	Z_1	E_1	Z_2	E_2	Z_3	E_3
V-Pol	53.8 Ω	50°	53.8 Ω	0°	20.1 Ω	107°
H-Pol	53.8 Ω	58°	53.8 Ω	26.8°	16 Ω	43.4°

striplines, whose dimensions shown in Table 4.2 are calculated by resorting to equation (4.9) and ADS Controlled Impedance Line Designer. In this layout, the transition between metal layers M_3 and M_5 is also shown, as well as the package to PCB transition. A 3D representation of the model is shown in Fig. 4.13.

Table 4.2: Matching network transmission line physical dimensions at the centre frequency of 26 GHz.

Polarization	Z_1	E_1	Z_2	E_2	Z_3	E_3
V-Pol	53.8 Ω	50°	53.8 Ω	0°	20.1 Ω	107°
H-Pol	53.8 Ω	58°	53.8 Ω	26.8°	16 Ω	43.4°

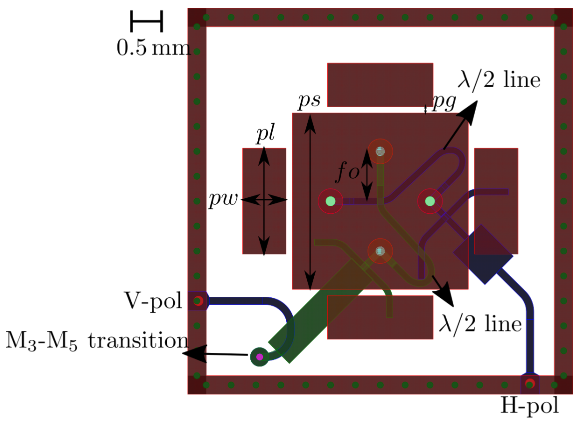

Figure 4.12: Final layout with feeding and matching networks, inter layer and PCB to package transitions (ground planes and grounding vias omitted).

The full system is simulated using ADS Momentum and the magnitude of the S-parameters on V-pol (port 1) and H-pol (port 2) ports when fed from a 50 Ω microstrip line on the host PCB, are shown in Fig. 4.14, where it can be seen that not only the reflection coefficient magnitude is

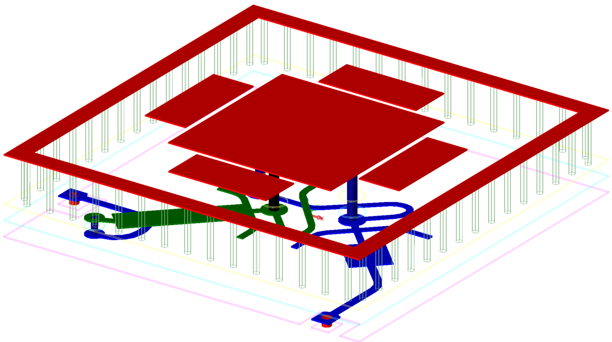

Figure 4.13: 3D model of full layout (ground planes and grounding vias omitted).

below -10 dB in both ports, but also the isolation is greater than 40 dB over the bandwidth of 24.25 GHz to 27.5 GHz. The E-Plane and H-Plane radiation patterns at 24.25, 26 and 27 GHz are shown in Figs. 4.15, 4.16 and 4.17, respectively. It can be seen that the radiation pattern suffers practically no change from the beginning to the end of the 5G K-band. Such is due to the differential feed topology which reinforces the fundamental TM_{100} and TM_{010} degenerate modes and cancels higher order modes resulting in a frequency stable radiation pattern. A radiation efficiency of approximately 60 % and a peak gain of 5 dBi were observed, in simulation, at both V-pol and H-pol ports.

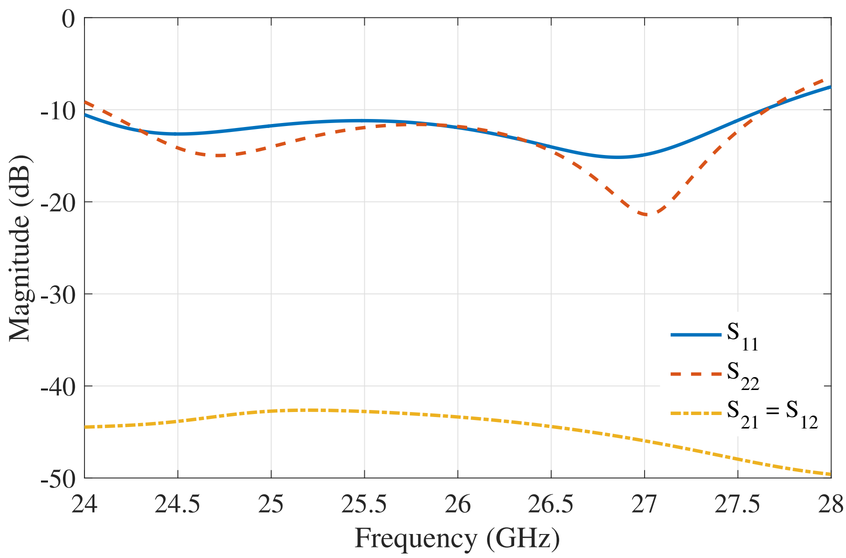

Figure 4.14: Simulated results for the magnitude of V-Pol (port 1) and H-Pol (port 2) S-parameters.

4.6 Summary

In this chapter a new topology of dual-polarized patch antenna-in-package was shown. The simulation results showed a high isolation greater than 40 dB between polarizations and a matched

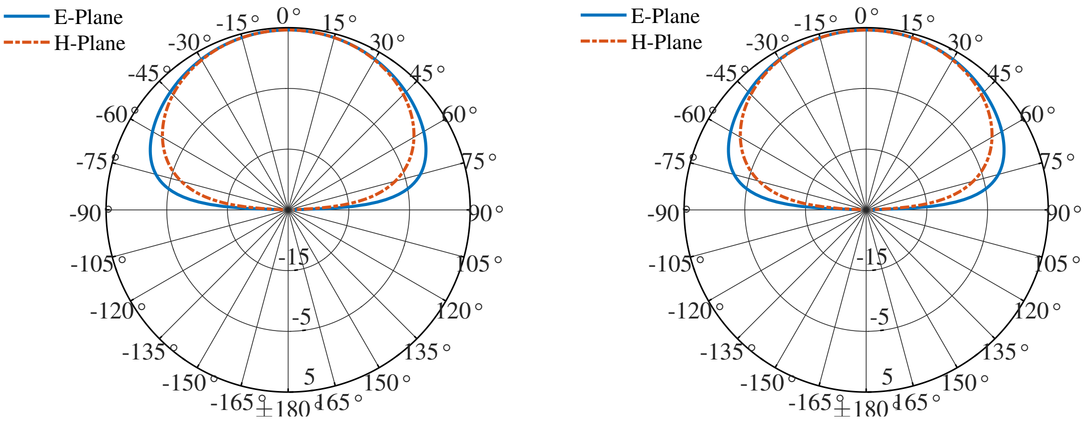

(a) (b)

Figure 4.15: Simulated V-pol (a) and H-pol (b) radiation patterns at 24.25 GHz.

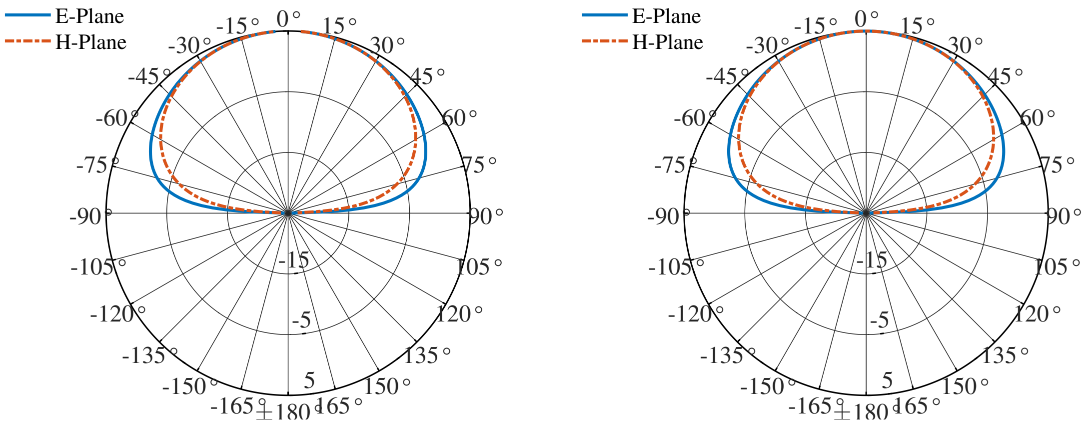

(a) (b)

Figure 4.16: Simulated V-pol (a) and H-pol (b) radiation patterns at 26 GHz.

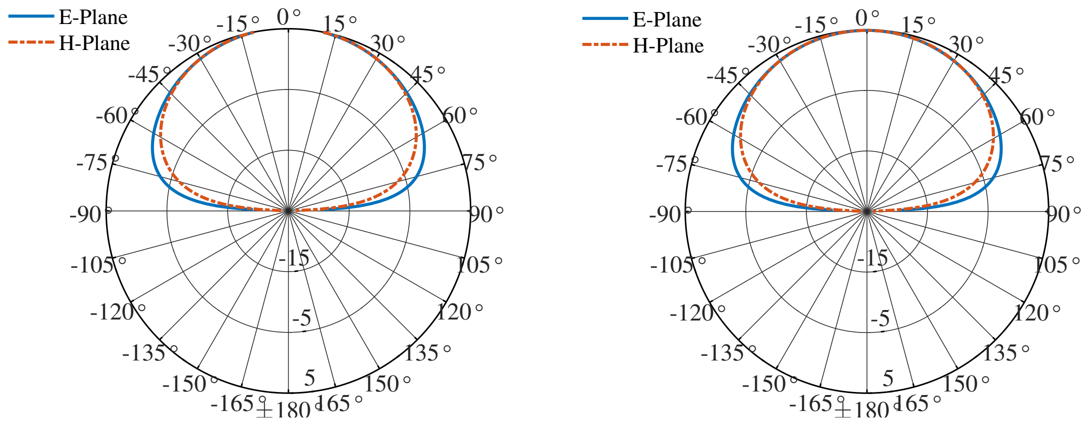

(a) (b)

Figure 4.17: Simulated V-pol (a) and H-pol (b) radiation patterns at 27.5 GHz.

impedance in both ports. Nonetheless, despite reducing the number of layers for the antenna, extra complexity is added in the matching process, which can also slightly increase fabrication costs. Furthermore, it was shown that with our design a frequency stable radiation pattern, from 24.25 GHz to 27.5 GHz, can be obtained, thanks to the differential feeding technique.

Chapter 5

Zero Beam Squint Differential Series-Fed Array for Automotive Radar on W-band

Series-fed patch arrays are the most common choice for usage in automotive applications to employ in Long Range Radars (LRR) and Medium Range Radars (MRR) [48–50], as shown in Fig. 5.1. Their usage lies on the fact that highly directive antennas can be obtained with relatively small size. Furthermore, the ease of fabrication of such antennas make them appealing for mass production for the automotive market. Nonetheless, due to the fact that the delay lines interconnecting the antenna elements have a frequency dependent phase shift, beam squint is natural on this type of antennas [51]. Additionally their sidelobe level is hard to control due to the radiation coming from the delay lines and the feeding network of the array [9].

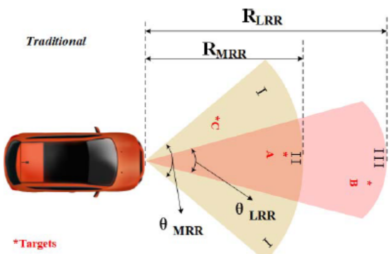

Figure 5.1: Automotive long range and medium range radars [50].

Beam squint can be solved by introducing a differential feed in which one side of the array is fed in phase and the other end with a 180° phase shift. This results in a boundary condition at the centre of the array which forces the beam to be symmetric, therefore eliminating beam squint [9]. However, the outphasing and feeding network is electrically large which introduces additional losses and has a significant impact on the sidelobe level of the antenna due to its radiation.

In this chapter, a new design method is proposed which employs an heuristic approach, based on a particle swarm optimizer (PSO) coupled with a deterministic gradient optimizer, to achieve a series feed array with a usable frequency range of $75-79\,\text{GHz}$. This approach allows one to neglect the effects of the radiation caused by the delay lines which impedes the usage of deterministic design methods. By using a PSO their radiation effects are automatically considered as the objective function is based on the radiation pattern. The design process of a differential feeding network in substrate integrated waveguide (SIW) to avoid stray radiation is also shown. Typical microstrip feeding networks can impair the sidelobe level of the isolated antenna due to higher order modes and surface wave radiation, but it is proven in this chapter that by using SIW instead the effects of the feeding network can be neglected. The final result is an antenna that can be operated in its full frequency range without significant changes in the radiation pattern, no beam squint, reduced sidelobe level and reflection coefficient magnitude smaller than $-12\,\text{dB}$. Table 5.1 provides a comparison between the work of this chapter and the state-of-the-art, showing that in fact our antenna is able to provide a much wider operating frequency span when compared with current designs. In some works of the state-of-the-art it was impossible to evaluate beam squint as the authors provide the radiation pattern for the centre frequency only due to the inherent narrowband behaviour of their antennas.

Table 5.1: Comparison between this work and the state-of-the-art.

Reference	No Beam Squint Frac. Bandwidth	Worst Sidelobe Level
[50]	$1.3\,\%$	$-12\,\text{dB}$
[51]	$--$	$\approx -5\,\text{dB}$
[9]	$5\,\%$	$\approx -7.5\,\text{dB}$
[52]	$--$	$-15\,\text{dB}$
This Work	$> 5.2\,\%$	$-12\,\text{dB}$

5.1 Active S-Parameters

Since an antenna array with differential feed is being designed, an analysis in terms of its active S-parameters can be useful for determining the reflection coefficients at each of its ports, considering that one port is fed in phase and the other out of phase.

To understand the concept, it makes sense to first define the S-parameters from the schematic of Fig. 5.2. According to Pozar [45, pp. 178], the scattering matrix is defined as

$$\begin{bmatrix} V_1^- \\ \vdots \\ V_N^- \end{bmatrix} = \begin{bmatrix} S_{11} & \cdots & S_{1N} \\ \vdots & \ddots & \vdots \\ S_{N1} & \cdots & S_{NN} \end{bmatrix} \begin{bmatrix} V_1^+ \\ \vdots \\ V_N^+ \end{bmatrix} \tag{5.1}$$

where V_i^- and V_i^+ represent the waves coming out and into port i, respectively. The coefficients S_{ij} establish a relation between them given by

$$S_{ij} = \left. \frac{V_i^-}{V_j^+} \right|_{V_k^+ = 0 \,\text{for}\, k \neq j} \tag{5.2}$$

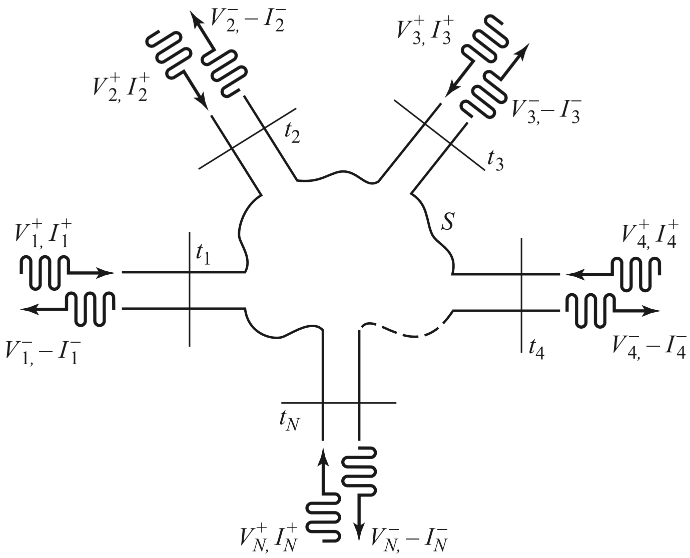

Figure 5.2: S-parameter schematic [45, pp. 174].

In the particular case of a two port network the signal flow graph shown in Fig. 5.3 can be used to understand active S-parameters. Because of the source V_2 placed on the second port, the reflection coefficient seen at port 1 by source V_1 will be different from simply S_{11} [53]. Considering V_1 the incident voltage at port 1, it is trivial to understand from the signal flow graph that $a_1 = V_1$ and $b_1 = a_1 S_{11} + a_2 S_{12}$. Furthermore, since V_2 is the incident voltage at port 2, we have $a_2 = V_2$. The active S_{11} is simply defined as the reflection coefficient seen at port 1 with the second source present, written as

$$S_{11a} = \frac{b_1}{a_1} = S_{11} + \frac{V_2}{V_1} S_{12} \tag{5.3}$$

which is equivalent to S_{11} if $V_2 = 0$. In the same way, the active S_{22} can be written as

$$S_{22a} = \frac{b_2}{a_2} = S_{22} + \frac{V_1}{V_2} S_{21} \tag{5.4}$$

The rationale presented here can be extended to multi-port networks in which the sum of all port contributions must be carried out to obtain the active reflection coefficient at a particular port [53].

In the case of a symmetrical two port network, we have $S_{11a} = S_{22a}$. If differential feeding is used, that is $V_2 = -V_1$ we have $S_{11a} = S_{22a} = S_{11} - S_{12} = S_{22} - S_{21}$. This allows one to design matching and feeding circuits using just one port instead of treating a more complex differential load.

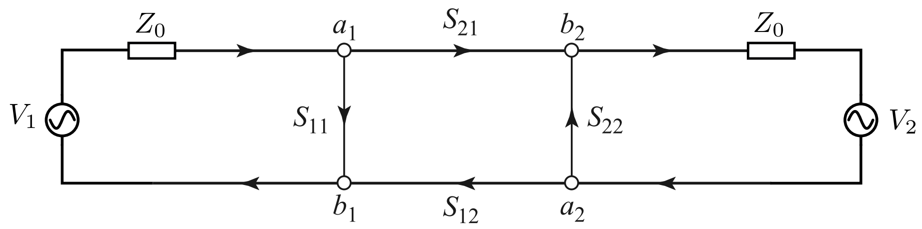

Figure 5.3: Signal flow graph two-port network schematic for obtaining active S-parameters.

5.2 Substrate Integrated Waveguide

A substrate integrated waveguide is a type of guided medium which is very similar to a rectangular metallic waveguide. It is composed of two metal layers on a substrate which are connected by vias. The two metal layers compose the E-wall and the vias the H-wall. However, since it supports no longitudinal currents because of its discontinuous H-wall made by vias, it is unable to support TM modes [54], being limited to TE mode propagation where vertical currents are allowed by the vias.

A schematic representation of a substrate integrated waveguide is shown in Fig. 5.4. Given the similarities of rectangular and substrate integrated waveguides, when TE modes are considered, we can calculate the waveguide dimensions by considering the desired operating frequency and the cutoff frequencies of TE_{10} and TE_{20}. For single mode operation, the operating frequency of 75 GHz must lie within the two cutoff frequencies of the fundamental and second mode. As such, for the operating frequency $f_0 = 75\,\text{GHz}$ to be exactly in the middle of the cutoff frequencies f_{c10} and f_{c20} of the first two modes, we can write

$$f_0 = \frac{f_{c10} + f_{c20}}{2} \tag{5.5}$$

where we know that

$$f_{c10} = \frac{c}{2a\sqrt{\varepsilon_r}} = \frac{f_{c20}}{2} \tag{5.6}$$

Considering the Rogers RO5880 substrate permittivity of $\varepsilon_r = 2.2$ one can combine equations (5.5) and (5.6) and obtain $a = w_{SIW} \approx 2\,\text{mm}$.

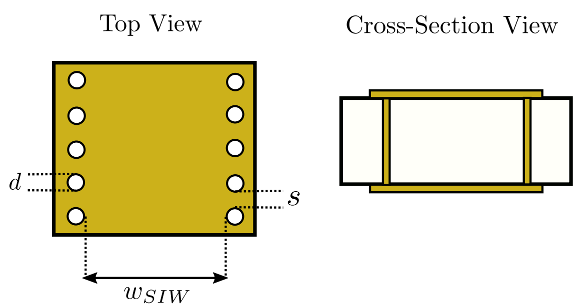

Figure 5.4: SIW schematic representation.

According to [54], to avoid radiation losses through the vias of the SIW, care must be taken on the chosen via spacing s and diameter d. The authors suggest, based on empirical criteria, that $s \leq 2d$ and $d \leq \lambda_g/5$, where

$$\lambda_g = \frac{2\pi}{\sqrt{\left(\frac{\omega\sqrt{\varepsilon_r}}{c}\right)^2 - \left(\frac{\pi}{a}\right)^2}} \tag{5.7}$$

is the guided wavelength at a frequency $\omega = 2\pi f$. Taking into account the higher operating frequency of 79 GHz of this design, we get $\lambda_g \approx 3.3$ mm. This results in the design limitations $d \leq 0.6$ mm and $s \leq 1.2$ mm. In this design $d = 0.15$ mm and $s = 0.2$ mm are used.

5.2.1 SIW to Microstrip Transition

A transition between a microstrip line and a SIW must be analysed, since both types of guided media will be present in the array. This is done following the recommendations and setting the initial dimensions as shown in [55], for the case of the E-band.

A layout representation of a SIW to microstrip transition is shown in Fig. 5.5. Since the authors of [55] have used a Rogers RO6002 substrate, the dimensions of the transition have to be further optimized, so that acceptable results are obtained for the Rogers RO5880 substrate. Performing a Quasi-Newton optimization made in HFSS, using the values given in [55] as an initial guess, values of $l1_w = 0.34$ mm, $l_{tapper} = 0.78$ mm, $w_{tapper} = 0.65$ mm and $w_{SIW} = 2$ mm yield the final. The goal of the optimization is defined to minimize the reflection coefficients at both the microstrip and SIW ports, but also to maximize the transmission coefficient between them. This procedure results in the S-parameters shown in Fig. 5.6, where port 1 is on the microstrip side and port 2 is on the SIW side.

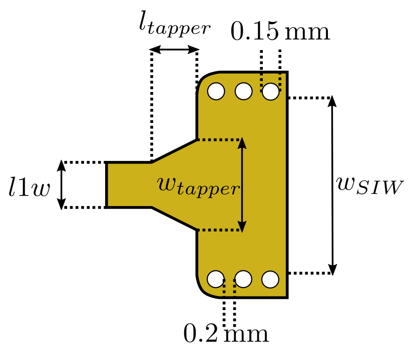

Figure 5.5: SIW to microstrip transition simulation model parameters.

It can be seen from Fig. 5.6 that an insertion loss of 0.2 dB and return losses higher than 20 dB are obtained with this transition, validating its usage.

5.2.2 SIW Power Divider

Since the signal to feed the antenna will come from a single SIW source, the signal has to be split into two equal halves, so that we can phase shift one of them by 180° to obtain differential feeding

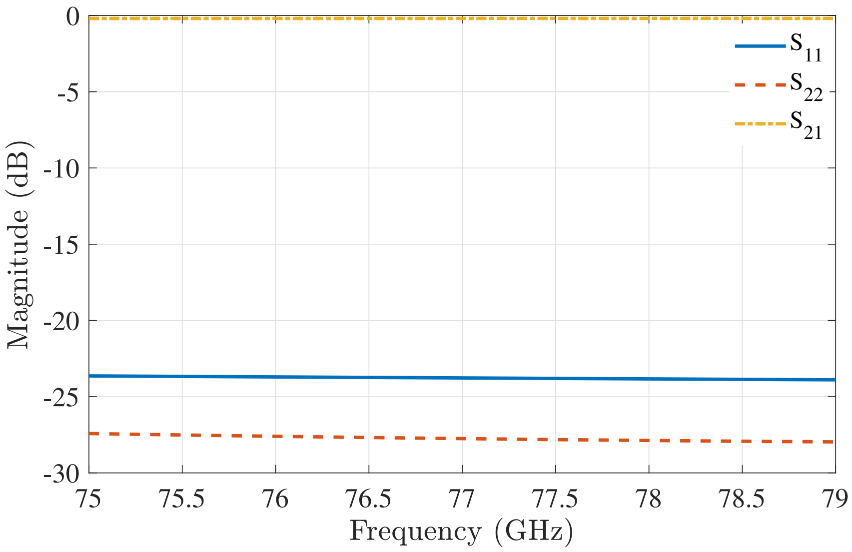

Figure 5.6: S-parameters of optimized microstrip to SIW transition.

of the series-fed patch array.

A SIW power divider was presented in [56]. We use a similar structure as shown in Fig. 5.7 where the final values that guarantee the best return loss and least insertion loss, after optimization, are $d_{fin} = 2.3\,\text{mm}$ and $l_{tapper} = 1.1\,\text{mm}$. The results are shown in Figs. 5.8 and 5.9. Port 1 is the common port and ports 2 and 3 are the output ports. The reflection coefficient on ports 2 and 3 are actually active S-parameters considering that each port is driven with equal phase and amplitude as will happen in the final design. They are obtained as shown in section 5.1.

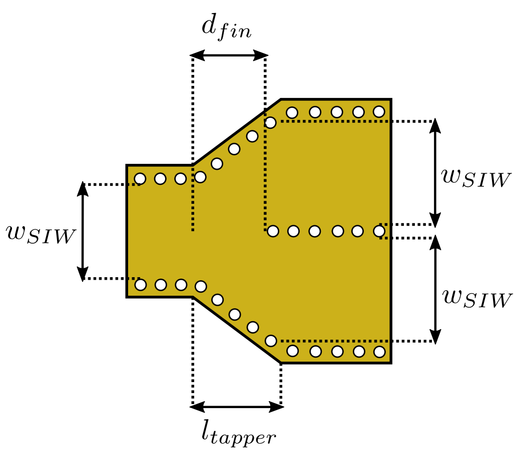

Figure 5.7: SIW power divider simulation model parameters.

Return losses higher than 24 dB and negligible amplitude imbalances are obtained which make this power divider suitable for usage in the feeding network of the series feed array.

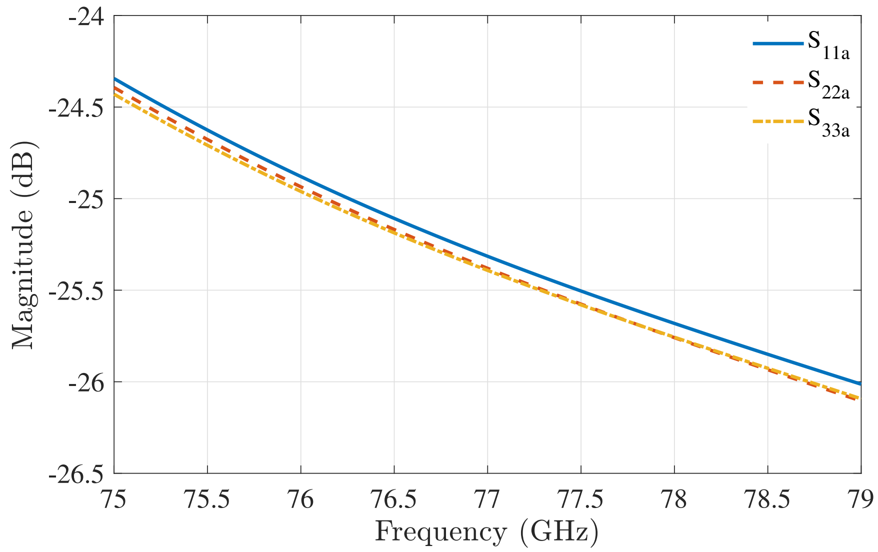

Figure 5.8: Active reflection coefficients at the divided signal ports 2 and 3.

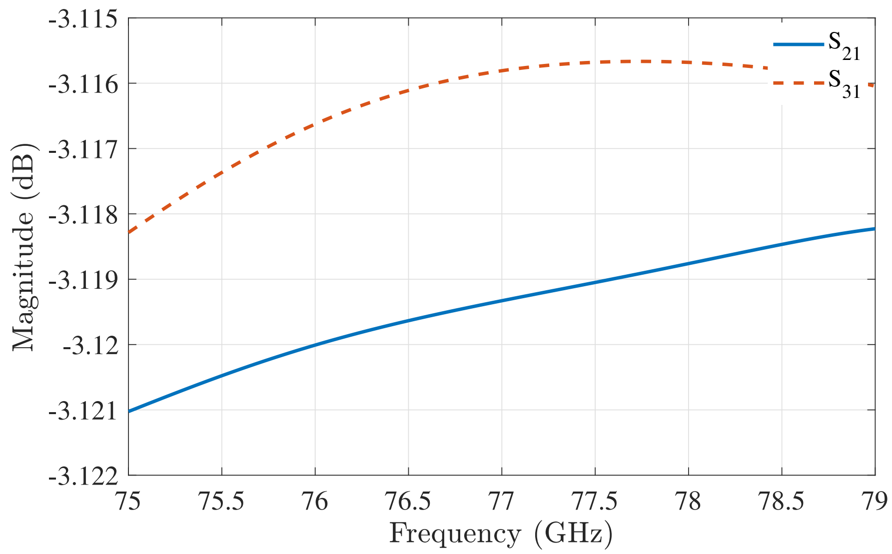

Figure 5.9: Transmission coefficients from common to coupled ports.

5.2.3 SIW Bends

For the signal to travel along the SIW feeding network, bends are needed for it to change direction as needed. However, SIW bends represent a discontinuity in the wave propagation, which can lead to reflected waves and power loss if not properly modelled and evaluated. They were extensively studied in [57], where it was concluded from numerical simulation results that careful via placement along the bend is crucial for optimized performance. Additionally, the bend radius plays a fundamental role on the signal propagation as it will make the discontinuity more or less abrupt depending on its value.

The layout representation of Fig. 5.10 shows the model used to evaluate the performance of the SIW bends. The bend radius R_{bend} is swept from 1 to 2.5 mm. The S_{11} magnitude as a function of bend radius is shown in Fig. 5.11 for 75, 77 and 79 GHz. It can be seen that $R_{bend} = 2$ mm offers the best overall return loss, and this is chosen as the value for the bends in our design.

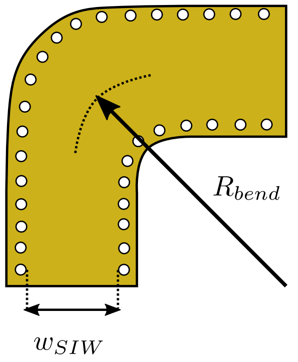

Figure 5.10: SIW bend simulation model parameters.

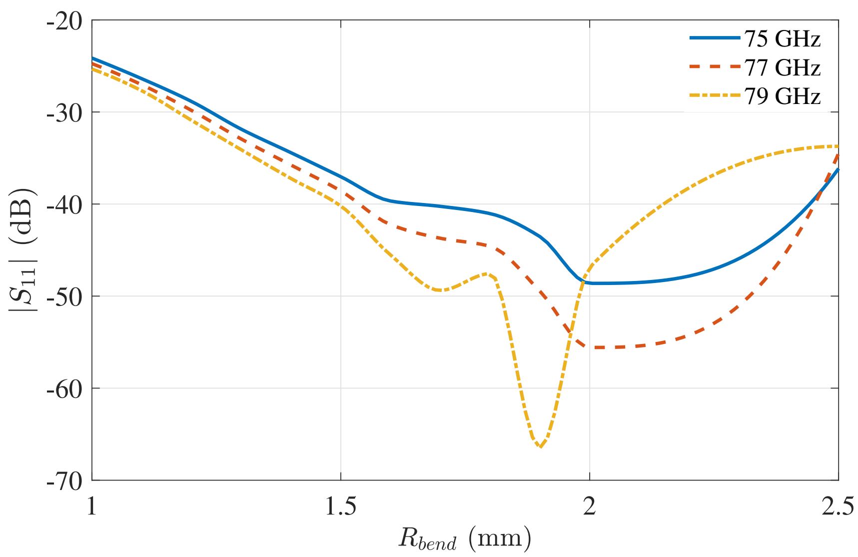

Figure 5.11: S_{11} parameter magnitudes for SIW bend as a function of bend radius at 75, 77 and 79 GHz.

5.3 Antenna Design

A series-fed patch array consists of multiple cascaded patch antennas connected with delay lines that introduce the necessary phasing for the desired radiation pattern, which can be calculated as described in section 2.4. Since each patch is approximately half-wavelength, each line should introduce 180° phase shift to achieve the goal of having a pattern with a peak in broadside direction ($+Z$) on the full operating bandwidth. Since the series-fed array is supposed to be fed differentially, a symmetry must exist on its structure.

5.3.1 Preliminary Design

The antenna is designed on a Rogers RO5880 substrate with a dielectric permittivity of $\varepsilon_r = 2.2$ and a loss tangent of $\tan\delta = 0.0009$. The metallization of the substrate is 17.5 µm copper. In Fig. 5.12 the simulation layout and its variables are shown. The simulation model is cut by its symmetry plane in the finite simulation method (FEM) in HFSS. Considering the in-phase signal is fed from the left and the outphased signal from the right of the antenna, since there is a geometrical symmetry on the array, in its centre the signals will meet and sum to zero, which will create a zero voltage, and thus no electric field. This is equivalent to considering just half the structure imposing an E-field symmetry boundary condition at the half plane. Wave ports are used at the edge of the substrate, so that the reflection coefficient is always normalized to the equivalent characteristic impedance of the microstrip line with a width of $l1_w$.

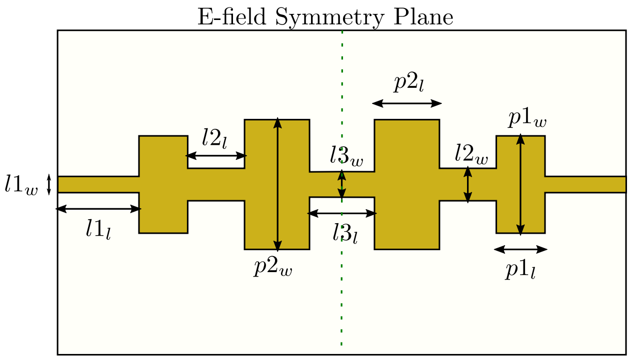

Figure 5.12: Simulation layout of four element series-fed array.

A PSO is used to determine the variable values that result in a reflection coefficient magnitude below −10 dB, a sidelobe level of −20 dB and a gain as high as possible. Therefore, the objective function is defined as

$$OF = -G_{peak} + |SLL - 20| + 0.7 \cdot |S_{11}| \tag{5.8}$$

where G_{peak} is the peak gain, SLL the sidelobe level and S_{11} the reflection coefficient at the antenna input. The PSO parameters are defined taking into account the recommendations of [47]. The cognitive coefficient is set as $c1 = 1.6$, the social coefficient $c2 = 1.6$ and the inertia coefficient $\omega = 0.35$. The optimization uses $N = 90$ particles for each iteration and the values of the variables shown in Fig. 5.12 are allowed to vary as shown in Table 5.2. These values are obtained by considering the minimum design rule for the line width $w \geq 100$ µm. They also consider the patch dimensions which can be obtained by taking into consideration the method described in section 4.2. Applying the patch design formulas one obtains for a nominal patch at 77 GHz a length $l = 1.1$ mm and a width $w = 1.5$ mm. Furthermore, the optimization parameter bounds consider the delay lines to be nominally a half wavelength at the centre frequency.

Table 5.2: PSO parameter bounds.

Parameter	Lower Bound	Upper Bound
$l1_l$	0.3 mm	1.8 mm
$l2_l$	0.3 mm	1.8 mm
$l3_l$	0.3 mm	1.8 mm
$l1_w$	0.1 mm	0.5 mm
$l2_w$	0.1 mm	0.5 mm
$l3_w$	0.1 mm	0.5 mm
$p1_l$	0.7 mm	1.7 mm
$p1_w$	1 mm	2.5 mm
$p2_l$	0.7 mm	1.7 mm
$p2_w$	1 mm	2.5 mm

Following the PSO, a Quasi-Newton optimization is run in HFSS to obtain a refined solution of the best guess provided by the PSO. This type of approach allows the PSO to make a wider search for the global minimum, due to the constant inertia coefficient, while still being able to obtain a refined solution based on the Quasi-Newton optimizer. After running the optimizer, the final values are $l1_l = 1.75$ mm, $l1_w = 0.34$ mm, $l2_l = 0.83$ mm, $l2_w = 0.48$ mm, $l3_l = 0.51$ mm, $l3_w = 0.12$ mm, $p1_l = 1.29$ mm, $p1_w = 1.86$ mm, $p2_l = 1.28$ mm, $p2_w = 2.36$ mm. The co-polarized E-plane radiation patterns are obtained and are shown in Fig. 5.13, for 75, 77 and 79 GHz, where it can be seen that the antenna exhibits peak gains near 13 dBi at the three frequencies. Furthermore, the sidelobe level is approximately -19 dB which is a good result for our optimization method. Additionally, the reflection coefficient magnitude is well below -10 dB as shown in Fig. 5.14.

5.3.2 Final Design with Feeding Network

The full assembly of the antenna and its feeding network is shown in Fig. 5.15. The bottom section of the feeding network is half guided wavelength larger than the top side, for the required 180° phase shift of the differential feeding to be obtained. The reference plane is also shown in the layout, where the effects of the edge-launch connector are not considered in simulation, since they will be de-embedded in the measurement procedure shown in the next section.

The simulated reflection coefficient magnitude at the reference plane shown in Fig. 5.15 is shown in Fig. 5.16 where it can be seen to be below -12 dB from 75 to 79 GHz. The E- and H-plane radiation patterns are shown in Figs. 5.17 and 5.18, respectively. A higher sidelobe level can be seen when compared to the result of Fig. 5.13. However, this degradation is expected as the full structure is simulated including the feeding network. The SIW to microstrip transitions also radiate and increase the sidelobe level of the antenna. Nonetheless, the pattern stability is still

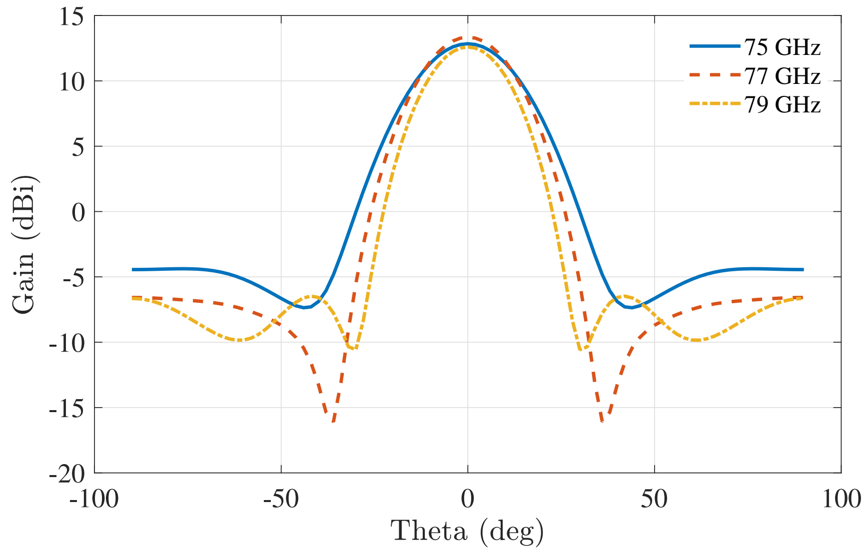

Figure 5.13: E-plane optimized radiation patterns at 75, 77 and 79 GHz.

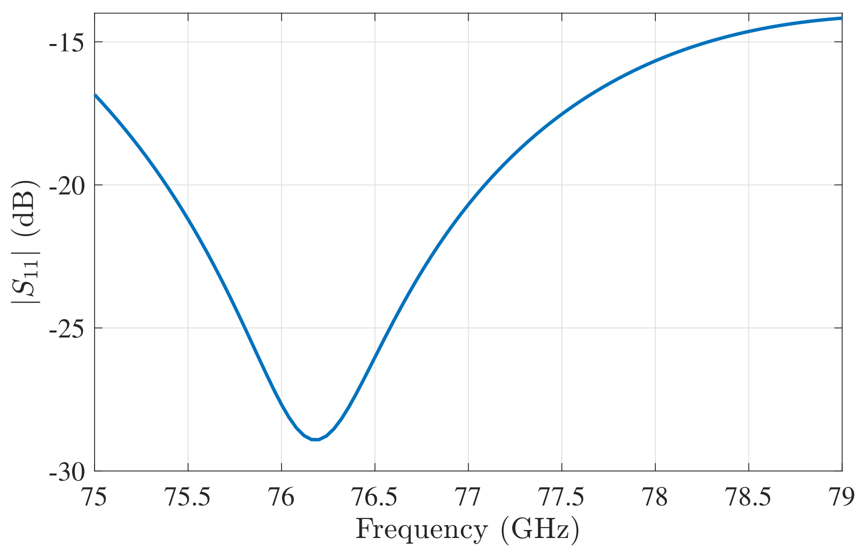

Figure 5.14: Reflection coefficient at antenna input after optimization.

assured as the patterns are very similar in the whole operating frequency of the antenna. This is a direct result of the differential feeding network with low amplitude and phase imbalances that result in a highly symmetrical and stable radiation pattern.

5.4 Experimental Evaluation

For experimental evaluation a method is needed to excite the SIW that goes to the antenna, the option was to use a detachable 1 mm end-launch connector, as shown in Fig. 5.15, to interface the VNA with the PCB.

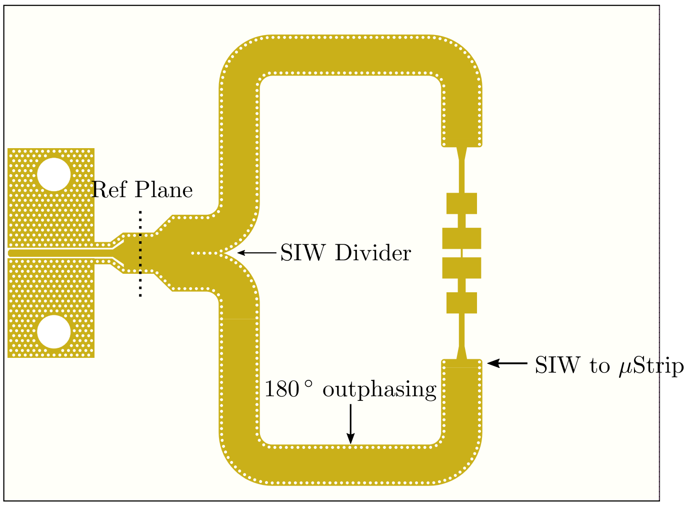

Figure 5.15: Simulation layout of four element series-fed array with feeding network.

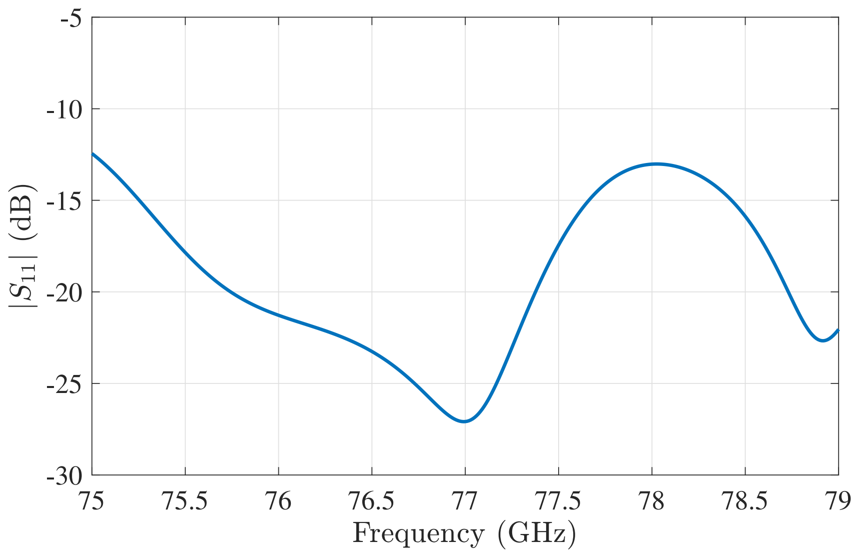

Figure 5.16: Simulated reflection coefficient magnitude of full antenna with feeding network.

The end-launch connector used to excite the PCB is the Southwest Microwave 2492-04A-6. The manufacturer advises a conductor-backed coplanar waveguide (CBCPW) to be used with their connector. The signal launch from the connector to the PCB needs to be optimized for the CBCPW line coming out of the connector into the PCB. The characteristic impedance of the CBCPW line is calculated according to [58, pp. 89], considering the parameters shown in Fig. 5.19, as

$$Z_0 = \frac{60\pi}{\sqrt{\varepsilon_{eff}}} \frac{1}{\frac{K(k)}{K(k')} + \frac{K(k_3)}{K(k_3')}} \tag{5.9}$$

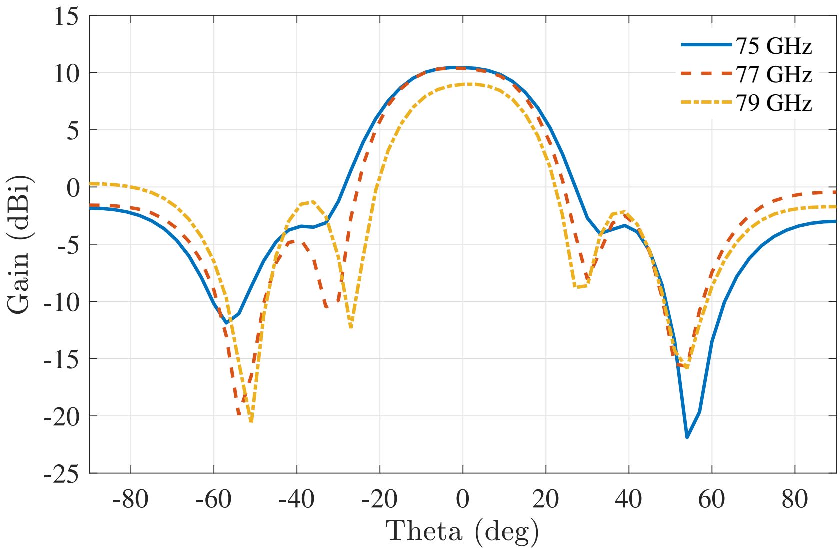

Figure 5.17: Simulated E-plane radiation patterns at 75, 77 and 79 GHz of the full antenna with feeding network.

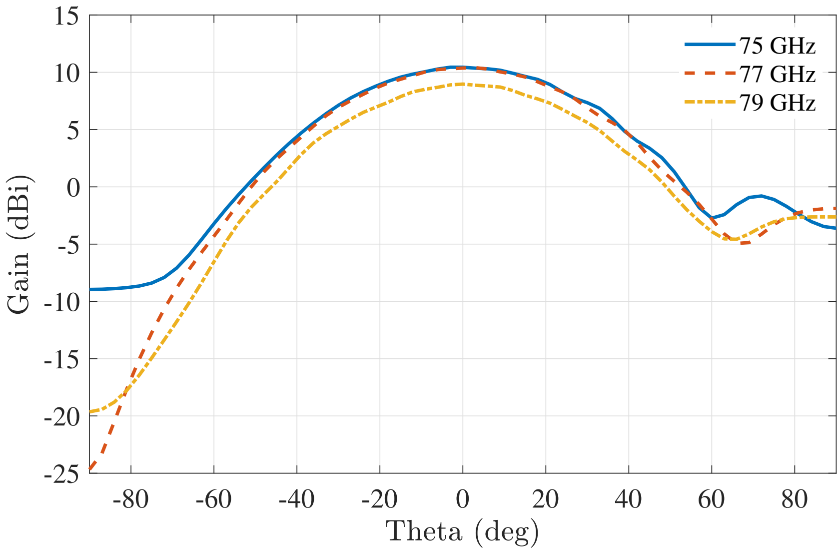

Figure 5.18: Simulated H-plane radiation patterns at 75, 77 and 79 GHz of the full antenna with feeding network.

where

$$
\begin{aligned}
k &= a/b \\
k_3 &= \tanh\left(\frac{\pi a}{2h}\right) / \tanh\left(\frac{\pi b}{2h}\right) \\
k' &= \sqrt{1-k^2} \\
k_3' &= \sqrt{1-k_3^2}
\end{aligned}
\tag{5.10}
$$

and $K(k)$ denotes the complete elliptical integral of the first kind. In the case of our transmission line, since the frequency is high, via stitching is needed to avoid ground resonances and radiation, which slightly alters the impedance calculated by the method of [58, pp. 89]. Therefore, a tuning of the dimensions has to be carried out in FEM simulations resulting in a CBCPW line whose dimensions are $h = 0.254$ mm, $2a = 0.45$ mm and $2b = 0.65$ mm.

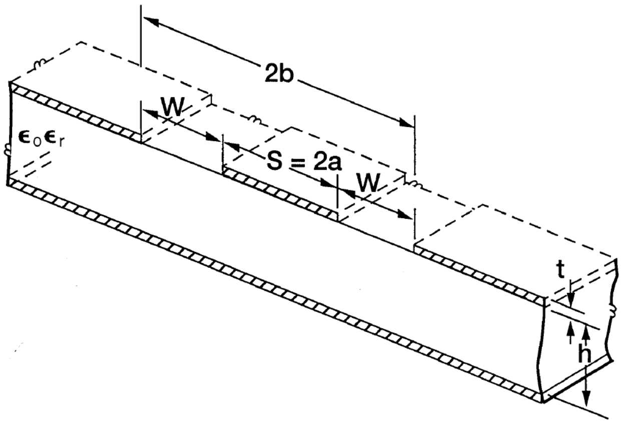

Figure 5.19: CBCPW parameter definitions [58, pp. 88].

The Southwest Microwave 2492-04A-6 connector is simulated using FEM in HFSS and attached to the CBCPW line as shown in Fig. 5.20. A tapper needs to be performed to improve return loss. The transmission and reflection coefficients are shown in Fig. 5.21 where an insertion loss below 0.4 dB and a return loss higher than 20 dB are obtained. Port 1 is the coaxial port and port 2 is the port placed on the CBCPW.

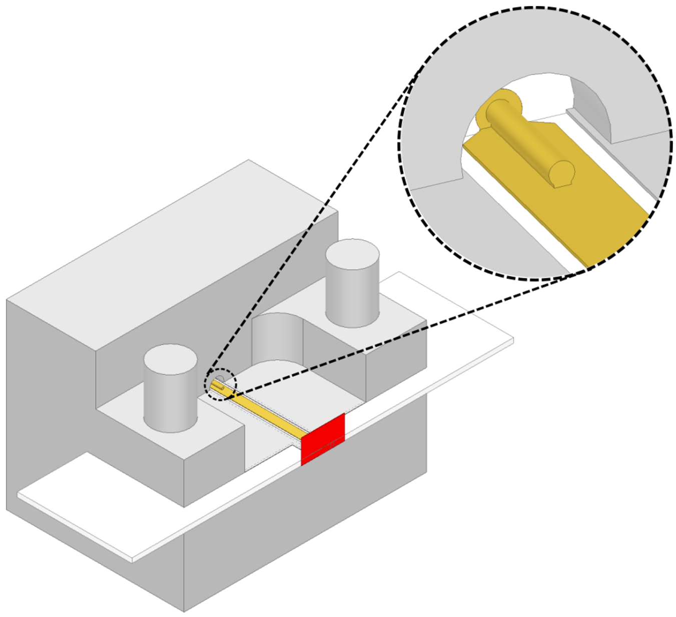

Figure 5.20: Simulation model of the end-launch 1 mm connector driving the CBCPW transmission line.

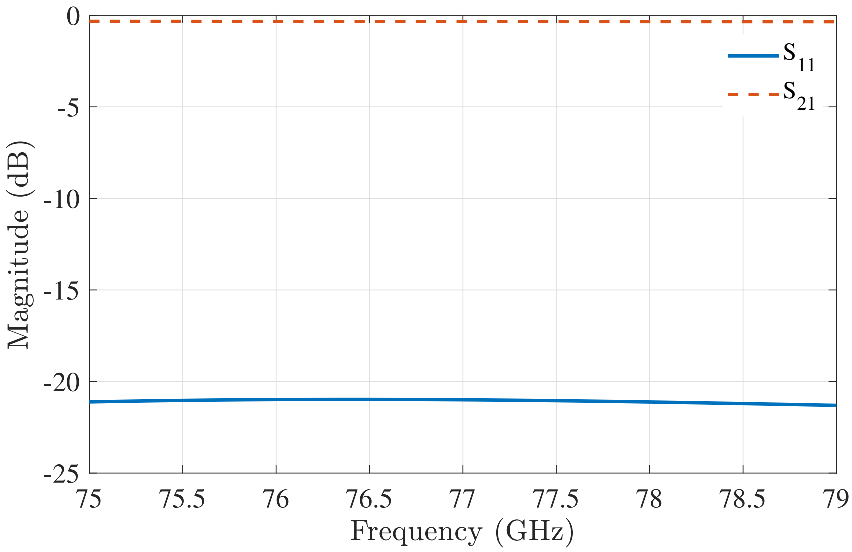

Figure 5.21: S_{11} and S_{21} of connector to CBCPW transition.

Since the feeding from the connector goes to a CBCPW transmission line, but the signal still needs to go to a SIW to be passed to the antenna, an additional transition is required A layout model of a CBCPW to SIW transition is designed as shown in Fig. 5.22, taking into account the work in [59]. For simulation purposes port 1 is placed in the CBCPW transmission line and port 2 in the SIW side. After optimization to achieve low insertion loss and high return loss on FEM simulation, the dimensions of the transition were obtained as $2a = 0.45\,\text{mm}$, $2b = 0.65\,\text{mm}$, $w_{inner} = 1.34\,\text{mm}$, $w_{outer} = 1.71\,\text{mm}$, $l_{tap} = 0.71\,\text{mm}$ and $w_{SIW} = 2\,\text{mm}$. This yields the reflection and transmission coefficients shown in Fig. 5.23 in which a return loss higher than 25 dB and an insertion loss lower than 0.3 dB are shown to be met.

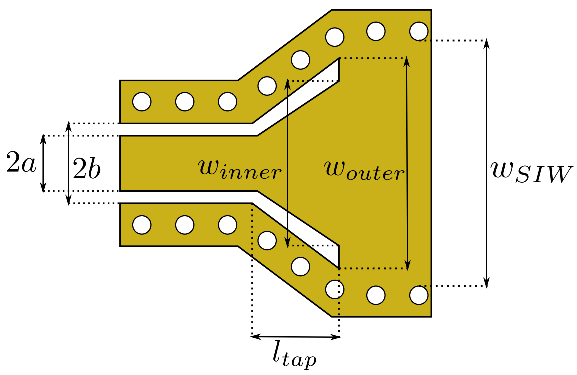

Figure 5.22: Model layout of CBCPW to SIW transition.

As discussed before, the reference plane must be shifted to the SIW, so that connection parasitics and systematic errors are calibrated out of the measurement process. Because load resistors have parasitics that at these frequencies result in poor matching, a Short-Open-Load-Through (SOLT) kit can not be designed. Furthermore, the connection of loads to the SIW is practically

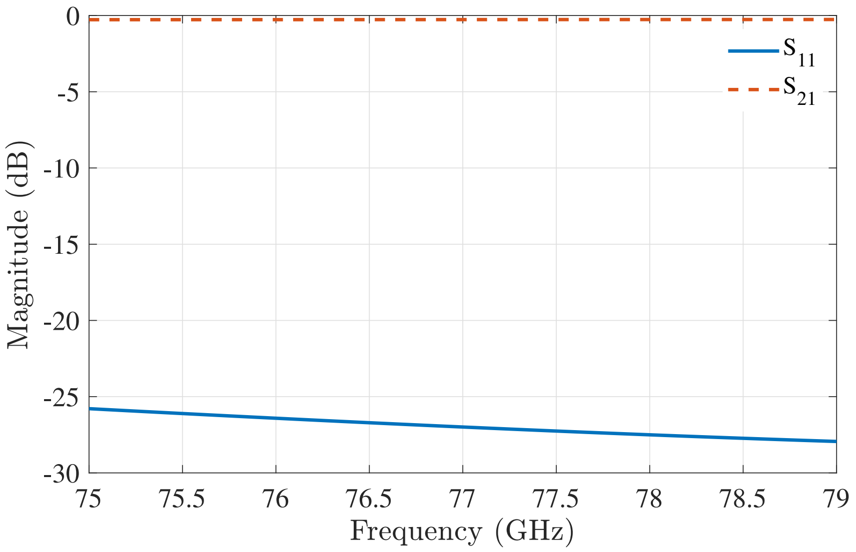

Figure 5.23: S_{11} and S_{21} of CBCPW to SIW transition.

infeasible unless more transitions are designed. Therefore the most suitable option is a Through-Reflect-Line calibration kit, in which only the line standard has to be precisely known. The through standard should be a simple zero length mating between the desired reference planes of each port. The reflect standard can be an open or a short. The line standard should be such that it is matched ($S_{11} = S_{22} = 0$) to the reference plane port impedances. Moreover, its transmission phase shall differ from the through standard by a magnitude of at least 20° up to 160° which introduces a bandwidth limitation [60, pp. 20]. A general rule-of-thumb is to set this standard to be $\lambda_g/4$ at the calibration kit centre frequency. Fig. 5.24 shows the TRL calibration kit designed for shifting the port reference planes to the SIW as desired.

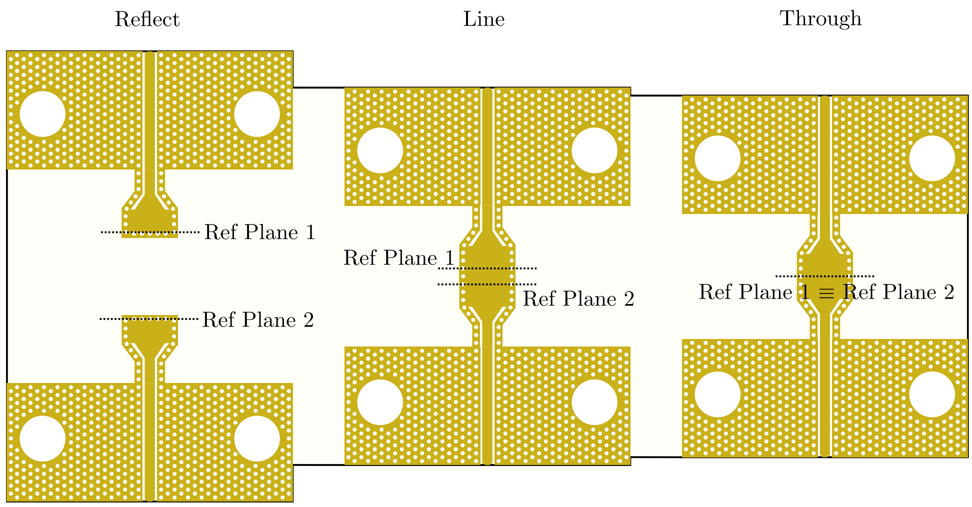

Figure 5.24: Illustration of TRL calibration kit board.

After careful design of the calibration kits, the boards were manufactured. The fabricated

PCBs are shown in Fig. 5.25. The measurements are taken in a Keysight PNA N5224B using the WR-10+ VDI frequency extension modules. After setting up the measurement equipment and calibrating systematic errors using the custom designed calibration kit, the antenna input reflection coefficient (S_{11}) shown in Fig. 5.26 is obtained. The results show an acceptable agreement in their shape. However, there are slight discrepancies at the middle of the band. These can be due to calibration errors. Additionally, since the board substrate is very thin (0.254 mm), these calibration errors are further aggravated due to the boards flexing during the standard measurement process. Nonetheless, given all the possible measurement errors, even neglecting possible fabrication tolerances, the antenna can be said to be validated.

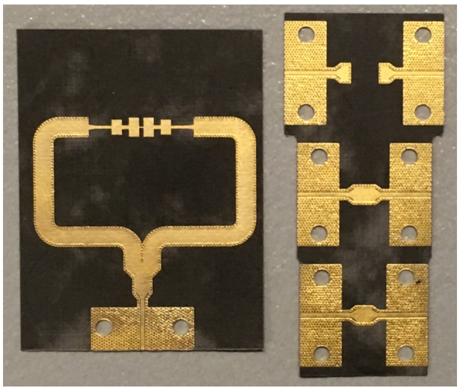

Figure 5.25: Fabricated antenna with feeding network (left) and TRL calibration kit (right).

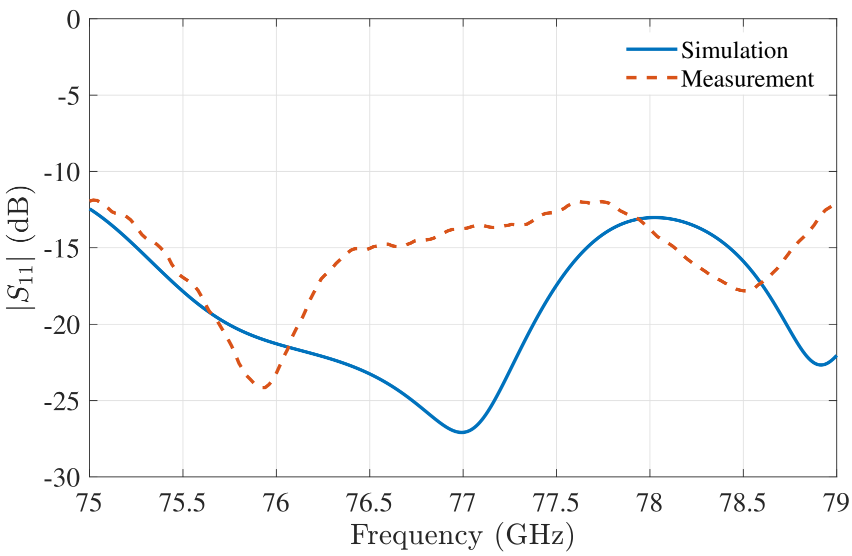

Figure 5.26: Measured and simulated reflection coefficient of antenna with feeding network.

5.5 Installed Antenna Performance

As shown in Fig. 5.1, this antenna is meant to be installed in vehicles to provide radar capabilities for collision detection and avoidance. However, it is known that installation of antennas in their final applications usually cause disturbances in both their input impedance and radiation pattern [61–63].

In [64] an hybrid MoM-PO approach was used to determine the radiation pattern changes and predict the performance of the installed antenna. Ansys Savant is capable of using PO and UTD to correctly predict the performance of electromagnetic waves in electrically large structures, where conventional full-wave methods would result in abnormally large memory and processing power requirements. The simulated radiation pattern can be used as the source antenna in the PO/UTD simulation in Ansys Savant to correctly predict its installed performance. The simulation model assembled in Ansys Savant, for an SUV, is shown in Fig. 5.27.

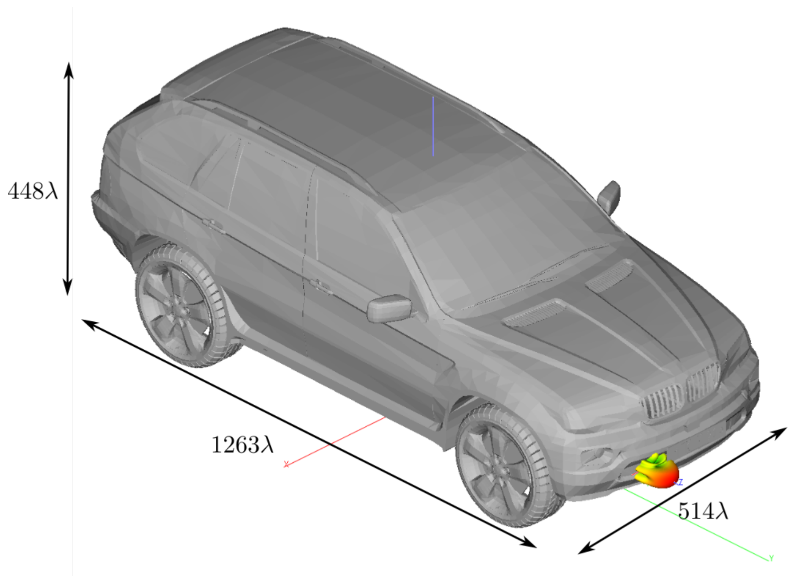

Figure 5.27: Simulation model of antenna installation on front bumper of SUV.

Running the PO/UTD simulation with the source set as the simulated radiation pattern of the antenna developed in this chapter, the radiations patterns in the E- and H-plane can be obtained. Figs. 5.28 and 5.29 show the E- and H-plane radiation patterns for both the antenna in free space and installed in the front bumper, at 77 GHz, as shown in Fig. 5.27. In these radiation patterns, significant ripple and increased sidelobes, mainly at large angles, can be observed. These two phenomena occur because of multiple reflections in both the license plate and in the front bumper and grids of the car. If the antenna was installed near curved shapes or knife edges, phenomena such as diffraction and creeping waves could occur which would lead to a degradation in the front-to-back ratio of the antenna. This PO/UTD simulation assessment proves the paramount importance of carefully analysing the antenna on its final installation environment to prevent unexpected results on the final application.

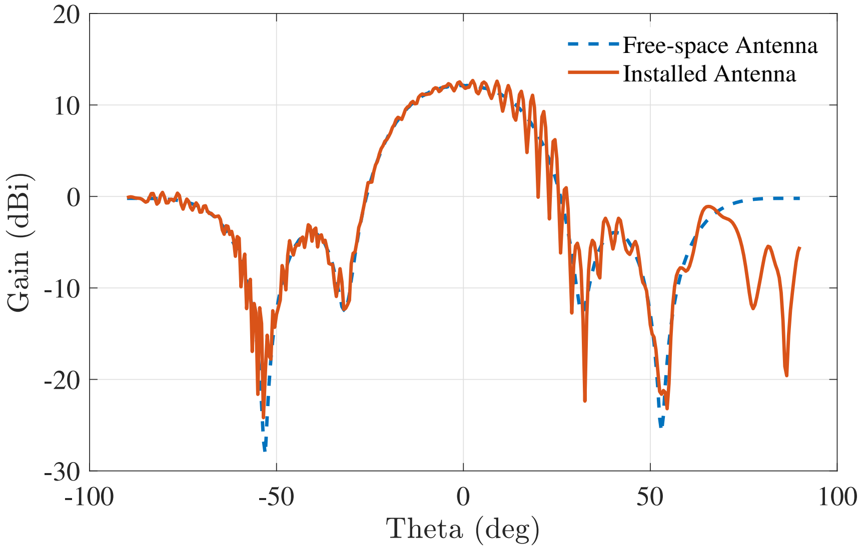

Figure 5.28: E-plane radiation pattern comparison at 77 GHz of free-space and installed antenna.

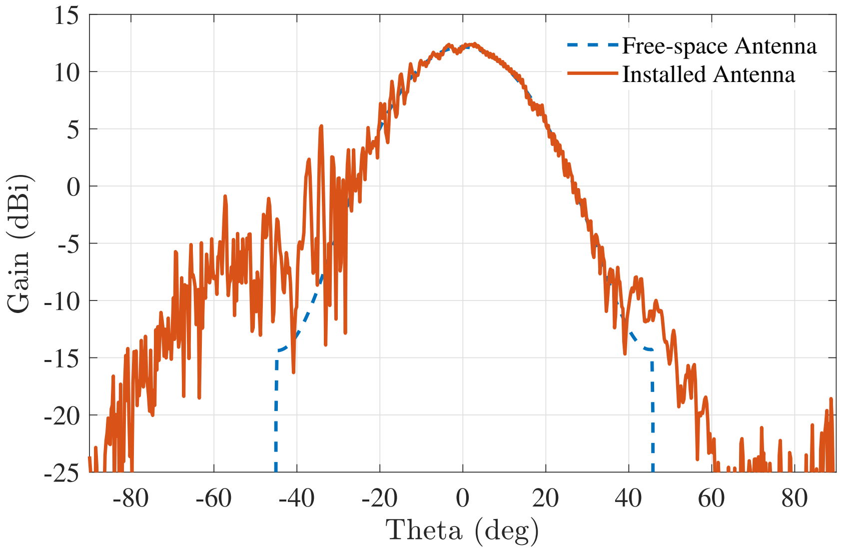

Figure 5.29: H-plane radiation pattern comparison at 77 GHz of free-space and installed antenna.

5.6 Summary

In this chapter a differentially-fed series fed patch array with zero beam squint was presented for automotive radar application on W-band ($75-79$ GHz). It was shown that by feeding a series patch array differentially, radiation patterns with no beam-squint can be obtained due to the symmetry which is reinforced by the feeding method. A boundary condition is imposed in the middle of the array by the differential feeding, enabling both wide impedance and pattern bandwidths. It was also observed that feeding networks play a crucial role in such arrays, as themselves can contribute to radiation and impair radiation pattern performance, if not carefully designed. A SIW feeding network was thoroughly analysed for this purpose. Reflection coefficient measurements were carried out to validate the design approach and simulation of the full array. An analysis of the installed antenna performance on the front bumper of a BMW X5 was made to show how the radiation pattern of the antenna may change in the final application. This antenna shows a rather new approach that can be further improved with more elements and integrated in smaller systems, such as Low Temperature Co-Fired Ceramic (LTCC) for example, to further reduce its size and cost.

Chapter 6

Elliptical Monopole Antenna on InP Substrate for Sub-THz RTD-based Oscillators

The RF and microwave frequency spectrum is nowadays more congested than ever. For that reason, large bandwidths can not be allocated at widely used low frequencies for high bitrate transmissions.

For in-room data distribution, point-to-point mobile communications backhaul and fixed-wireless access, V-band ($40-75$ GHz) and E-band ($60-90$ GHz) are already being used. Big chunks of spectrum are allocated and readily available at E-band spanning as wide as 9 GHz [65]. However, if very high data-rates are desired such as 100 Gbit/s, spectral efficiencies of approximately 10 bit/s/Hz have to be achieved. This requirement can, of course, be relaxed if much larger bandwidths are available.

In iBROW project, in whose scope the work that will follow was developed, an opportunity was identified at sub-THz frequency bands. Considering Fig. 6.1, several frequency bands with low atmospheric attenuation can be identified, namely at 250, 630 and 850 GHz. The largest portion of low attenuation bandwidth has a 120 GHz span centred at 250 GHz. Considering, once again, the 100 Gbit/s case, with such bandwidth the spectral efficiency requirement can be relaxed to approximately 1 bit/s/Hz, which is very easy to achieve.

For the physical layer, as extremely high frequencies are needed, resonant tunnelling diodes (RTDs) are one of the obvious choices. Figure 6.2 shows a diagram of the application concept conceived in the iBROW project. These devices operate as high frequency transmitters due to their negative differential resistance properties at specific bias points. If such negative resistance is coupled to a sub-THz resonator, oscillation is possible. Making the device transition between positive and negative differential resistance regions the oscillation can be stopped and resumed at will, leading to an OOK modulated signal.

However, due to the high frequencies involved antenna connection parasitics can significantly impair the transmitter system. Therefore an on-chip antenna solution, monolithically fabricated

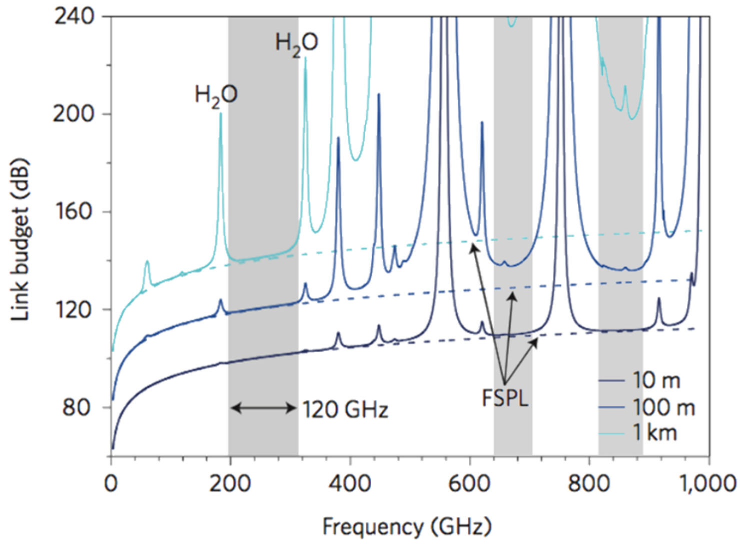

Figure 6.1: Free-space path loss and atmospheric attenuation at sub-THz frequencies.

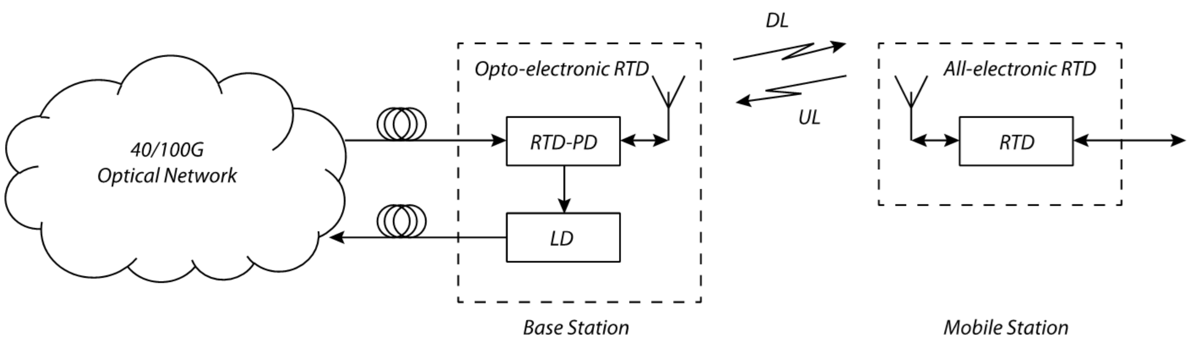

Figure 6.2: iBROW project concept.

in indium phosphide (InP) is proposed in this chapter, where two different monopole antennas are assessed. We later conclude that a simple quarter wave monopole does not meet the project requirements. Hence, a different solution based on an elliptical monopole with an exponentially tapered ground-plane is also investigated and validated through reflection coefficient measurements.

6.1 Sustrate Modes and Cavity Effect Analysis

Antennas fabricated on high permittivity materials typically suffer from reduced bandwidth and degraded efficiencies. At sub-THz frequencies the permittivity of InP was measured to be $\varepsilon_r = 12.33$ and the loss tangent $\tan\delta = 0.009$ [66]. Brown [67] stated that the ratio of radiation which goes in to the substrate and the one that escapes to free space is approximately $\varepsilon_r^{3/2}$. Additionally, he concluded that, if the frequency is within the sub-THz range, substrate modes appear which distort the radiation pattern of antennas and lead to a guided wave being reflected in the top and bottom interfaces.

The issues with antennas fabricated on thick high permittivity substrates were soon identified. In 1993, Brown proposed a photonic crystal for GaAs to circumvent substrate modes and enhance the air to substrate radiation ratio. Nonetheless, Brown's work requires a well established but expensive fabrication process. In 2015 Choi proposed a wire array design using three layers of benzocyclobutene (BCB) on top of an InP substrate, which yielded a simulated gain of 5 dBi with a peak radiation efficiency of 70 % [68]. Lee proposed a rectangular cavity antenna from which he attained a maximum radiation efficiency of 70% and a bandwidth of 41 GHz centred at 300 GHz [69]. In 2016 Choi designed a rectangular cavity antenna for operation at 280 GHz, albeit with a relatively low radiation efficiency of 52 % and an impedance bandwidth of 20 GHz [70].

Substrate modes were observed in [71], where their measured and simulated reflection coefficients exhibited sharp resonances. Furthermore, the simulated radiation patterns showed strong lobes and deformations. The authors realized from considering an electrically large substrate and geometrical optics, that a critical angle for rays emanating from the antenna existed, from which substrate modes would start to propagate. Considering the illustration of Fig. 6.3, the authors realized the critical angle is given in by

$$\theta_c = \sin^{-1}\left(\frac{1}{\sqrt{\varepsilon_r}}\right) \tag{6.1}$$

which plugging the relative electrical permittivity of indium phosphide results in a critical angle of $\theta_c \approx 16.4\,^\circ$. Such a low angle is a setback as a typical broadside radiating antenna such as the bowtie slot reported in [10, 71] will radiate most of its power at this angle of incidence, which will ultimately result in most of the power to propagate through the substrate because of total internal reflection.

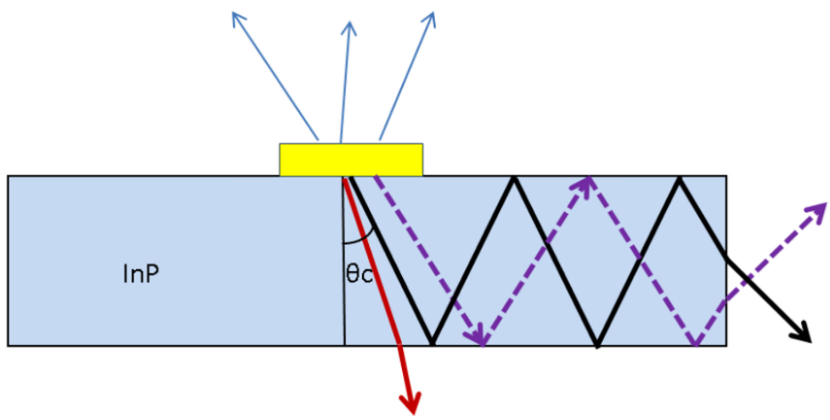

Figure 6.3: Illustration of substrate modes propagating in high permittivity thick substrates [71].

Since the permittivity difference between the substrate and the surrounding air is large, the reflectivity of the interface is large, therefore it will work similar to a cavity. As the substrate plays a crucial role in the antenna performance, its width, length and height have to be optimized alongside with the antenna geometry. This problem will become evident in the next section that assesses the performance of a quarter wave monopole.

6.2 CPW-fed Quarter Wave Monopole

The RTD connection to the antenna has to be made using a 20 µm trace, as fixed by the project partners that fabricated these devices. Since no connection can be made to the bottom side of the die a single layer transmission line needs to be used. Therefore, a suitable choice is a CPW line that matches the ground-signal-ground (GSG) connection of the RTD and measurement probes. Since the indium phosphide substrate thickness will be electrically large due to the available wafers, the CPW line impedance can be calculated from the schematic layout shown on Fig. 6.4 considering an infinitely thick substrate as

$$Z_0 = \frac{30\pi}{\sqrt{(\varepsilon_r + 1)/2}} \frac{K(k_0')}{K(k_0)} \tag{6.2}$$

where

$$\begin{aligned} k_0 &= \tfrac{S}{S+2W} \\ k_0' &= \sqrt{1 - k_0^2} \end{aligned} \tag{6.3}$$

and $K(k_0)$ is the complete elliptical integral of k_0. Knowing that for the RTD and probe connection we have $S = 20\,\mu\text{m}$, to obtain an impedance $Z_0 = 50\,\Omega$ a gap of $W = 14\,\mu\text{m}$ is calculated if a permittivity of $\varepsilon_r = 12.6$ is considered for indium phosphide.

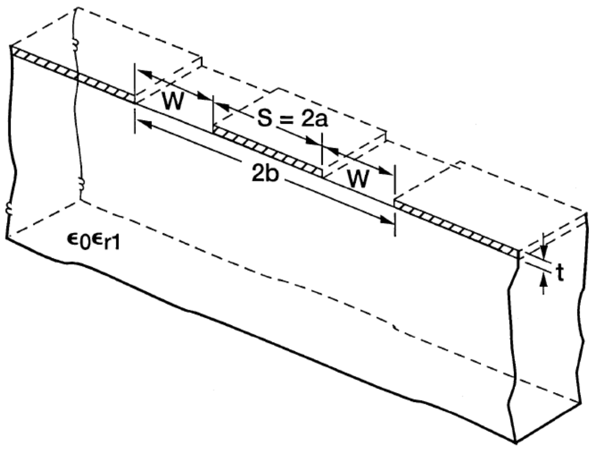

Figure 6.4: CPW parameter definitions on infinitely thick substrate [58, pp. 19].

Keeping the calculated CPW line dimensions, the monopole geometry is designed as shown in Fig. 6.5. The metallization is 400 nm gold. A 100 µm gap is needed from the edge of the substrate to the ground for RTD and GSG probe connections. Considering $\varepsilon_r = 12.6$ for the indium phosphide, a quarter wavelength is needed from the monopole to the infinite reflector plane on the bottom side of the die, so that air-side radiation can be obtained. At 300 GHz we have $h_1 = 70\,\mu\text{m}$ for quarter wavelength inside the substrate. However, as the wafer thinning process can only go as far as 100 µm a value of $h_1 = 100\,\mu\text{m}$ has to be fixed for the substrate height. Due to the thick substrate, it is valid to assume that the effective permittivity of the monopole is approximately $\varepsilon_{eff} = (\varepsilon_r + 1)/2 \approx 6.8$ [58]. Therefore, a monopole length of $l_{mono} \approx 100\,\mu\text{m}$ can be set as the initial value. The remaining initial values were set as $l_{gnd} = 100\,\mu\text{m}$, $w_{mono} = 20\,\mu\text{m}$ and $s_{gnd} = 10\,\mu\text{m}$. For the substrate size $l_{sub} = 250\,\mu\text{m}$ and $w_{sub} = 500\,\mu\text{m}$ were chosen.

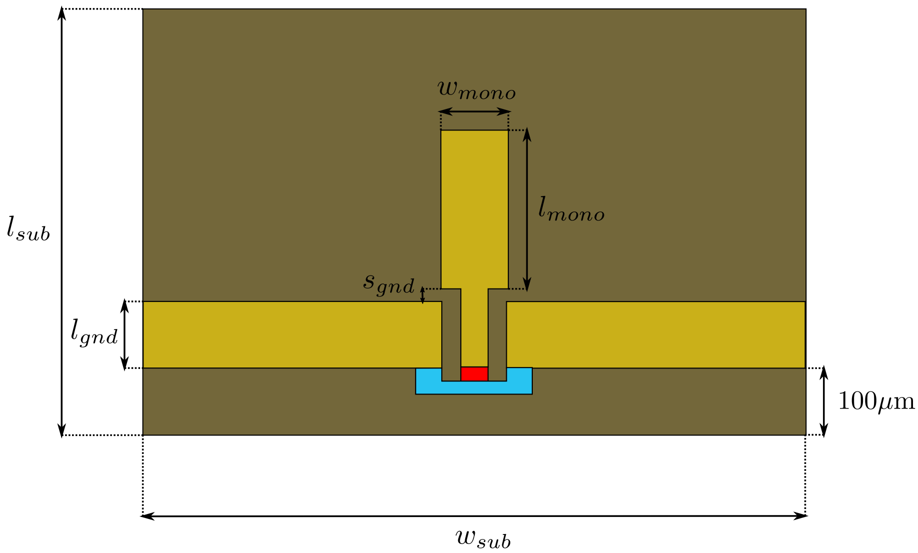

Figure 6.5: CPW-fed quarter wave monopole geometry.

The values described in the previous paragraph are used as initial guess of a Quasi-Newton optimizer in HFSS. The objective function is set to have a -10 dB impedance bandwidth of 20 GHz centred at 300 GHz. The final values after optimization are $l_{mono} = 140\,\mu\text{m}$, $w_{mono} = 50\,\mu\text{m}$, $l_{gnd} = 50\,\mu\text{m}$, $l_{sub} = 270\,\mu\text{m}$, $w_{sub} = 540\,\mu\text{m}$ and $s_{gnd} = 10\,\mu\text{m}$. The simulated electric field distribution inside the substrate is shown in Fig. 6.6 which shows the cavity effect. The reflection coefficient of the optimized antenna is shown in Fig. 6.7. The E- and H-plane patterns at 300 GHz are shown in Fig. 6.8. It can be seen that despite the low reflection coefficient and the wide bandwidth, there is considerable radiation in the antenna port direction. The peak gain of 8.6 dBi occurs at $\theta = -90°$ instead of the desired $\theta = 0°$ to obtain air side radiation. The simulated radiation efficiency at 30 GHz is approximately 95 %.

Due to the fact that radiation in the $+Z$ direction ($\theta = 0°$ pointing to the reader) could not be obtained with this topology, another geometry has to be analysed as described in the next section.

6.3 Elliptical Monopole with Exponential Ground-Plane Tapering

In 1992, Honda reasoned from the symmetry of the disk monopole that it should exhibit broadband omnidirectionality [72]. From this work onwards, planar topologies were proposed for low frequencies and omnidirectional ultra wideband (UWB) applications, where ground plane shaping was used for impedance matching [73]. For sub-THz frequencies Li suggested the usage of the circular monopole in a photonic transmitter where the high permittivity GaAs substrate beneath the antenna was removed [74].

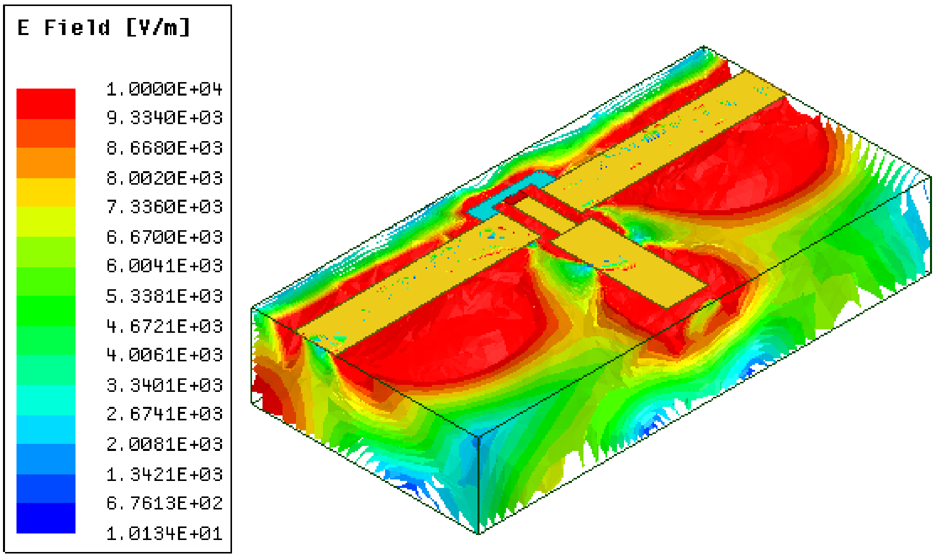

Figure 6.6: Simulated electric field distribution at 300 GHz inside InP substrate for quarter-wave monopole antenna.

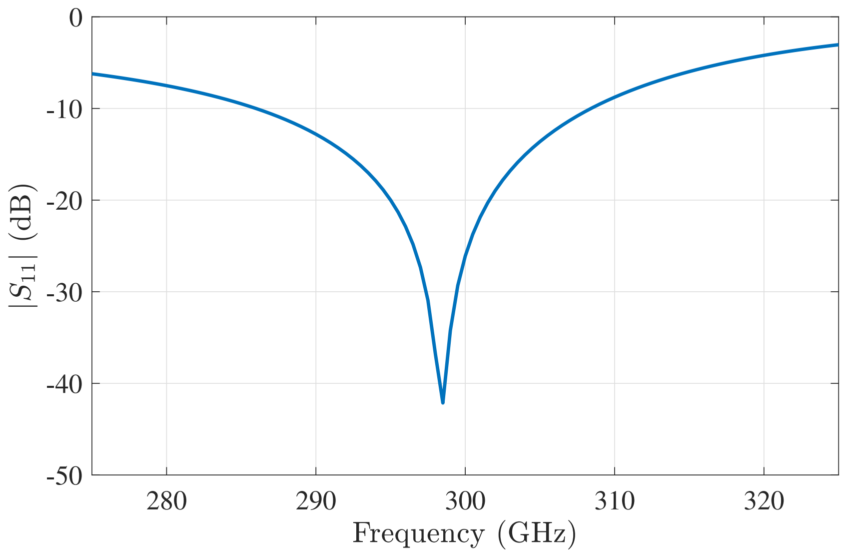

Figure 6.7: S_{11} magnitude as a function of frequency for optimized quarter-wave monopole antenna.

Given the work cited in the previous paragraph, the chosen geometry was a CPW-fed elliptical monopole with an exponential ground-plane tapering for attempting only broadside radiation. The antenna geometry is shown in Fig. 6.9. A 100 µm substrate is used as in the case of the quarter-wave monopole described in the previous section. The metallization is also composed of 400 nm gold. The exponential taper of the ground-plane is made according to the formula in Fig. 6.9,

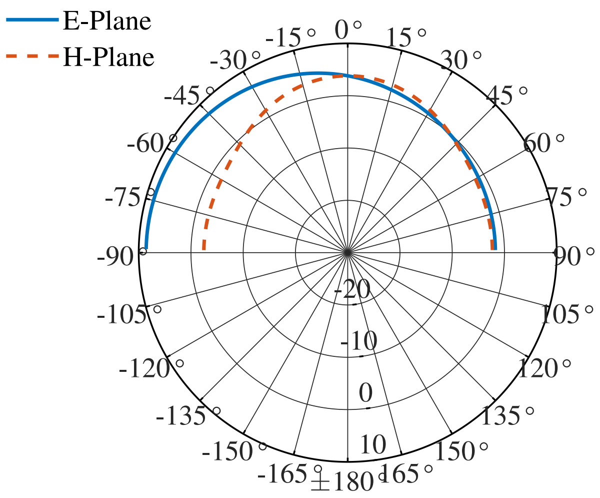

Figure 6.8: E and H-plane radiation patterns of optimized quarter-wave monopole antenna.

where the factors k and a are calculated by solving

$$\begin{cases} -g &= -ke^{a\cdot(S/2+W)} \\ -(g+h) &= -ke^{a\cdot(S/2+W+w)} \end{cases} \tag{6.4}$$

where S and W are the trace width and gap of the feeding CPW line, respectively.

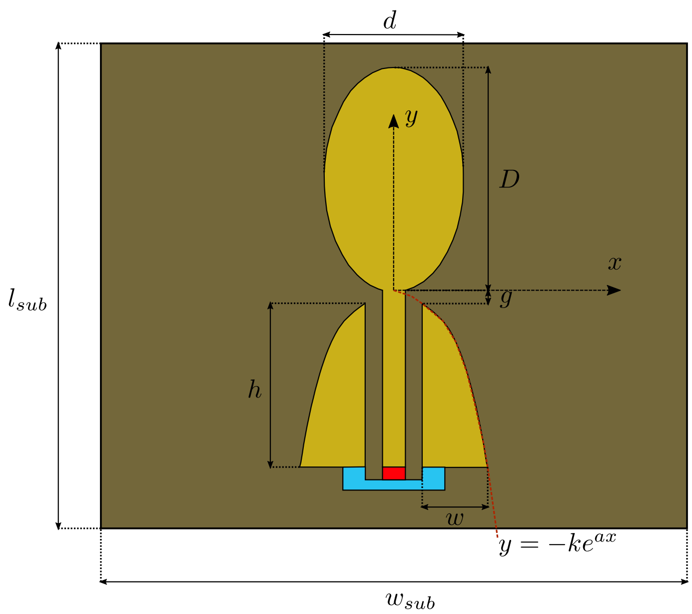

Figure 6.9: CPW-fed elliptical monopole geometry.

A trial and error approach is used and the different design variables are swept using FEM simulation so that their effect is understood. The elliptical disk major and minor diameters, D and d, greatly influence the resonant frequency of the antenna. The ground height h also has influence on the resonant frequency, as there are radiating currents in the outer part of the ground plane. The ground width w also influences the resonant frequency, however a lot less than the elliptical disk diameters. This happens because changing w effectively changes the exponential curve total length, influencing the radiating currents on the ground-plane which impacts the resonant frequency of the antenna. Remarkably, the elliptical disk diameters do not change the radiation pattern considerably, since the antenna retains its monopole behaviour. The ground plane height and width influence the backside radiation as larger values for these variables result in more backside radiation. Given the observed behaviour of the antenna when its design variables are changed, the process must focus on the optimization of the ground-plane h and w to obtain a radiation pattern with its peak gain as near as possible to $\theta = 0^\circ$, as desired for air-side radiation. Afterwards, D, d, l_{sub} and w_{sub} are optimized to achieve resonance at the desired centre frequency of 300 GHz. It is important to note that during the latter optimization process, the radiation pattern peak gain direction must also be included, as changing l_{sub} and w_{sub} slightly alters the radiation pattern of the antenna due to the aforementioned cavity effect.

After applying the method described in the previous paragraph, the final design variables are obtained as $D = 190\,\mu m$, $d = 120\,\mu m$, $g = 6\,\mu m$, $h = 137.5\,\mu m$, $w = 51\,\mu m$, $w_{sub} = 500\,\mu m$ and $l_{sub} = 400\,\mu m$. An antenna was fabricated according to these dimensions and the measured reflection coefficient was obtained using the setup shown in Fig. 6.10. These measurements were carried out by the project partners in the University of Glasgow. The simulated electric field distribution in the substrate cavity can be seen in Fig. 6.11. The measured and simulated reflection coefficients are shown in Fig. 6.12. There is a good agreement between the simulated and measured curves which validates the design. Moreover, the slight difference in resonant frequency between the simulation and measurement can be explained by the dicing process and InP permittivity, which were both seen to have a moderate influence in the resonant frequency of the antenna, when performing the trial and error approach described in the previous paragraph. The simulated E- and H-plane radiation patterns, at 300 GHz, are shown in Fig. 6.13. As it can be seen in the radiation pattern a peak gain of $G \approx 4.8$ dBi now occurs at a direction of $\theta = 11^\circ$ with this antenna. This is a significant improvement over the monopole antenna shown in the previous section. However, the gain is reduced by approximately 4 dB. Such must happen because the pattern of the elliptical monopole is much less directive, since the simulated radiation efficiency of the elliptical disk monopole is 95.3 %, which is similar to the quarter-wave monopole of the previous section.

6.4 Summary

In this chapter a successful implementation of an elliptical monopole in InP for sub-THz communications was shown. The good agreement between the measurements and the simulation results validated the proposed antenna, which was carefully designed to mitigate substrate modes and achieve air-side radiation. Nonetheless, variations on the InP permittivity and on the dimensions after fabrication shall be considered on future designs. Furthermore, the dicing process should be enhanced to avoid cracking in the edges that might degrade antenna performance.

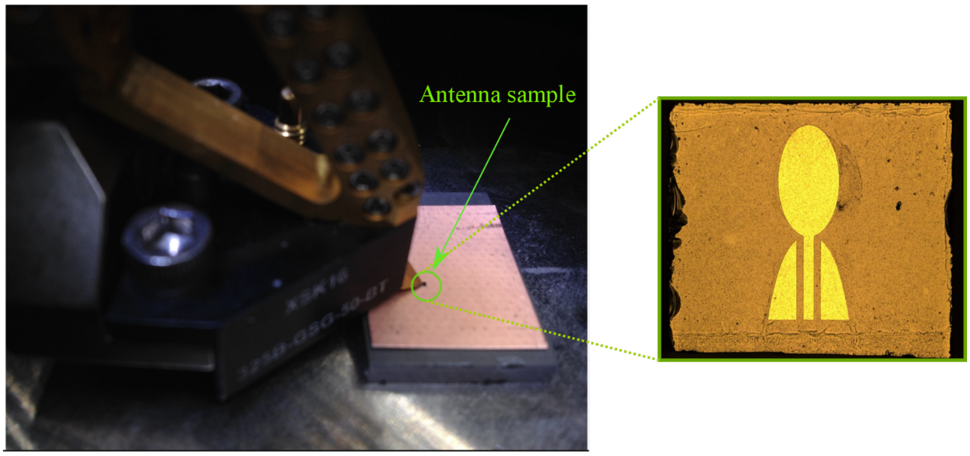

Figure 6.10: Measurement setup with probing station and reflector (left) and fabricated antenna sample (right).

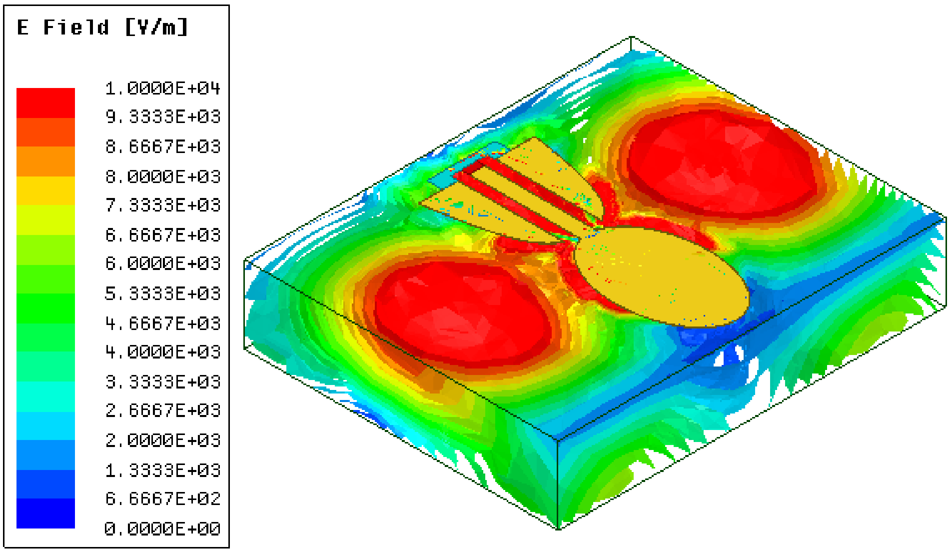

Figure 6.11: Simulated electric field distribution at 300 GHz inside InP substrate for elliptical disk monopole antenna.

The elliptical disk monopole was shown to have a limited bandwidth of approximately 20 GHz. This can be further improved by removing the large reflector on the backside of the die and replacing it with a shaped ground that can act as a parasitic element. This approach has the potential to also achieve air-side radiation but at the expense of a worse FTBR.

The possibility of including this antenna as a feeding element of a larger quasi-horn antenna is also interesting as the gain can be highly improved, thus increasing the distance at which high throughput communications can occur.

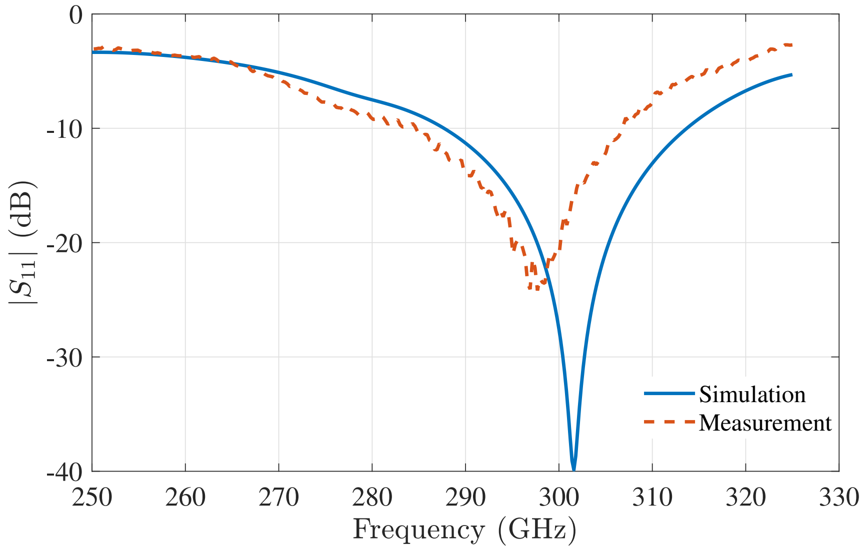

Figure 6.12: Measured and simulated S_{11} magnitude as a function of frequency for optimized elliptical disk monopole antenna.

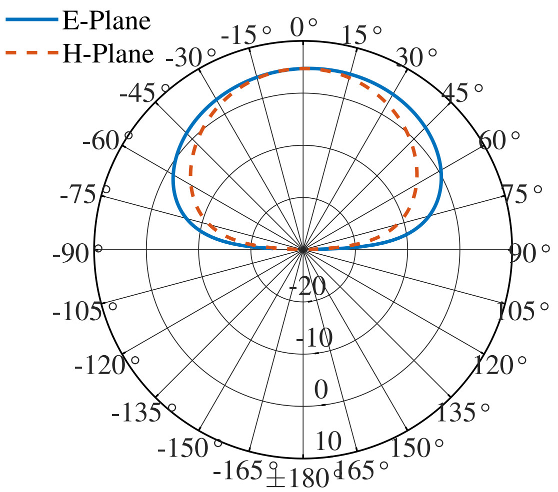

Figure 6.13: E and H-plane radiation patterns of optimized elliptical disk monopole antenna.

Chapter 7

Scalable High-Gaussicity Split-Block Diagonal Horn Antenna for Integration with Sub-THz Devices

The saturation of wireless spectrum access is leading to innovations in areas such as spectrum resource usage and massive multiple input multiple output (MIMO) systems. It is widely thought however, that the low hanging fruits of innovation for wireless communication are all but exploited with only marginal gains possible. For a real step change towards the coveted 1 Tbit/s wireless transmission, new areas of the spectrum must be utilized. This has been clearly identified in the ICT-09-2017 specific challenge of pushing spectrum access above 90 GHz towards THz. Recent breakthroughs in terahertz systems are overturning the "Terahertz gap" stigma associated with the previously difficult to access spectrum. With the emergence of viable THz communications systems on the horizon, it is crucial to add THz communications and networking to the technology roadmap for beyond the 5G timeframe and a step closer to industrial uptake. Terapod project is aiming at developing ultra-fast communication networks to replace wired connections in data centres to push one step further their operational efficiency and geometric design in a near future, as shown schematically in Fig. 7.1.

Because at higher frequencies, larger free-space path losses exist due to the smaller wavelength, the interest of using lenses and reflectors, as shown in Fig. 7.2, to enhance antenna performance arises. However, in this case, an antenna key parameter has to be met which is gaussicity [75]. This ensures that when designing systems for quasi-optical processing, the designer is presented with a predictable beam as it is the case of gaussian beams. Typically, the corrugated horn is the choice of election to achieve a high gaussian beam coupling efficiency. [76,77]. Despite the fact that this type of horn antenna has been extensively studied as an efficient Gaussian beam launcher, when frequency increases this approach becomes intricate due to the available fabrication processes. At sub-THz frequencies the corrugations are too small for achieving an acceptable yield with traditional CNC milling machine processes.

In this chapter we show how to obtain a high gaussicity from a split-block diagonal horn by

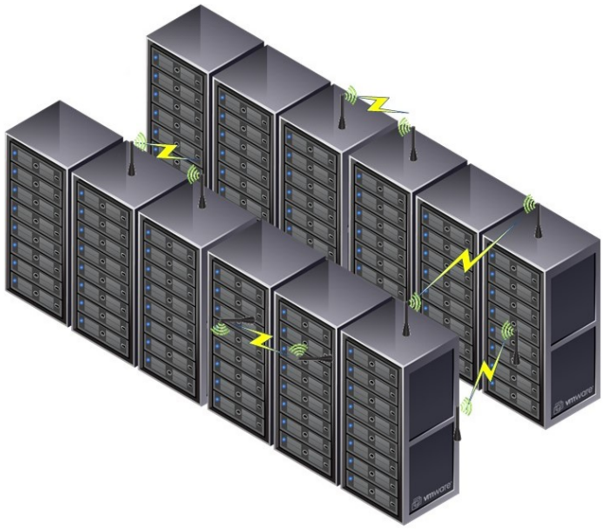

Figure 7.1: Terapod project concept with wireless connections between racks in data centre.

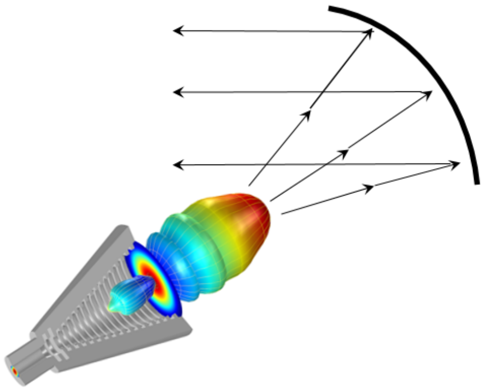

Figure 7.2: Schematic of quasi-optical processing of corrugated horn beam using reflector plate.

employing a spline profile instead of typical linear profiles. It is shown how an heuristic approach based on a Particle Swarm Optimizer (PSO) can be employed to determine the optimal spline dimensions relative to the diagonal horn aperture. Moreover, because of this normalization to the horn aperture we show how a scalable empirical model can be built, similar to the one verified in [12, pp. 756-759] for conical horns. With this model we describe how the antenna can be scaled in both gain and in frequency, while maintaining broadband gaussicity. A comparison can be seen in Table 7.1, in which it can be seen that the work developed in this chapter surpasses the state-of-the-art. Remarkably it even surpasses the spline profiling of a conical horn reported in [78] which is known for also being an effective gaussian beam launcher. Additionally, the reported performance is attained in the whole WR-3 frequency band rather than only in portions of the operating bandwidths as is the case of other works of the state-of-the-art.

Table 7.1: Comparison table with worst sidelobe level and cross polarization discrimination (XPD).

Reference	Worst Sidelobe Level (dB)	Worst XPD (dB)
[78]	−40	36.86
[11]	−30	24
This Work	−36	40

7.1 Linearly Profiled Diagonal Horn

The split-block technique appeared as an alternative to the conventional fabrication methods. The diagonal horn is a case in which the fabrication technique fits this category. The antenna is fabricated in two halves in which a milling tool passes through a metal block. The two machined blocks are joined together afterwards.

A better understanding of this technique can be seen in Fig. 7.3. Johansson and Whyborn proposed a diagonal horn and its fabrication technique, as well as its integration in an array, and extensively studied the fields at the aperture of the diagonal horn antenna [79]. Considering the schematic representation of the aperture of the diagonal horn in Fig. 7.4, Johansson describes the electric field on the aperture plane as

$$\vec{E}_{ap} = E_0 \left[\hat{x}\cos\tfrac{\pi y}{2a} + \hat{y}\cos\tfrac{\pi x}{2a}\right] e^{jk\delta} \quad \text{for } |x| < a,\ |y| < a \tag{7.1}$$

where

$$k\delta = \frac{2\pi}{\lambda}\left[\frac{2a^2 - x^2 - y^2}{2L}\right] \tag{7.2}$$

Shifting the reference to the η and ξ coordinates (diagonal axes between x and y), one obtains the E-field as

$$\begin{aligned} E_\eta &= \hat{\eta}\cdot\vec{E}_{ap} = \sqrt{2}E_0 \cos\tfrac{\pi\xi}{2\sqrt{2}a}\cos\tfrac{\pi\eta}{2\sqrt{2}a}\, e^{jk\delta} = \tfrac{E_0}{\sqrt{2}}\left[\cos\tfrac{\pi y}{2a} + \cos\tfrac{\pi x}{2a}\right] e^{jk\delta} \\ E_\xi &= \hat{\xi}\cdot\vec{E}_{ap} = \sqrt{2}E_0 \sin\tfrac{\pi\xi}{2\sin 2a}\sin\tfrac{\pi\eta}{2\sqrt{2}a}\, e^{jk\delta} = \tfrac{E_0}{\sqrt{2}}\left[\cos\tfrac{\pi y}{2a} - \cos\tfrac{\pi x}{2a}\right] e^{jk\delta} \end{aligned} \tag{7.3}$$

in which it can be seen that the co-polarized fields (η-directed) are symmetric on the $\eta\xi$ coordinate system. Moreover, the ξ-directed (cross-polarized) fields are anti-symmetric therefore no boresight cross polarization exists in theory.

Looking at equations (7.1) and (7.3) one can easily understand that the electric field at the horn aperture is a combination of two orthogonal TE_{10} modes with equally distributed power. These modes need to be excited from a waveguide coming into the diagonal horn antenna. Therefore, a rectangular waveguide fundamental TE_{10} must be converted to the horn modes previously described in this section. Mode conversion and mixing takes place because of the tapered transition between the waveguide and the diagonal horn as illustrated in Fig. 7.5.

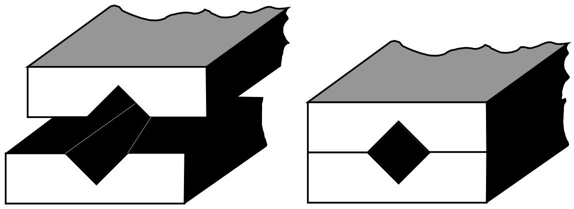

Figure 7.3: Split-block fabrication technique illustration [79].

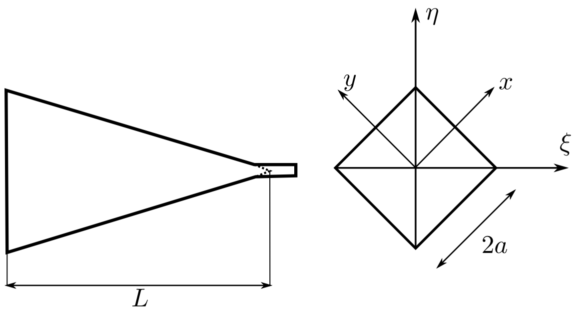

Figure 7.4: Schematic representation of diagonal horn geometry [79].

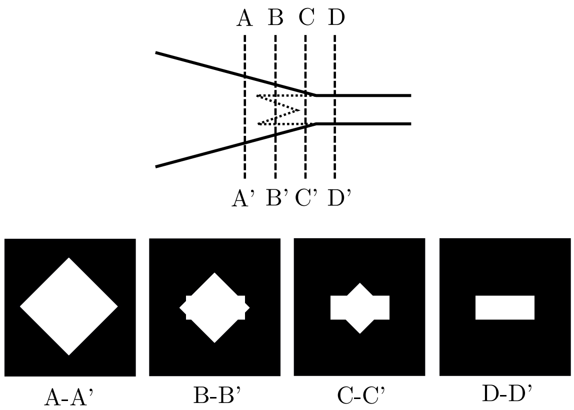

Figure 7.5: Rectangular waveguide-fed diagonal horn cross-sections [79].

Johansson and Whyborn decomposed the horn aperture fields using Gaussian-Hermite modes [79]. They concluded that not only the cross-polarized radiated power is approximately 10 % of the total power, but also the theoretical gaussicity of a linearly profiled diagonal horn is approximately 84 %, which is less than the typical 98 % of corrugated horns or 96.3 % of potter horns [75]. Such a low gaussicity and high cross-polarization component, leads us to discard this approach and try to obtain a different profile that is able to achieve better mode mixing from the waveguide to the horn modes, resulting in higher gaussicities and reduced cross-polarization. Such is described in the next section.

7.2 Spline Profiled Diagonal Horn

The smoothed-walled variable profile horn appeared as a viable alternative to the diagonal horn, in which the cutting tool does not follow a continuous profile when passing through the split-block. Instead, cutting depth variations are present which were proven to achieve high gaussicities [11, 78]. In [11] a spline-profiled diagonal horn was proposed and gaussicities of approximately 97 % were obtained at the centre frequency, through an optimization process. However, the cross-polarization discrimination (XPD) is still large. Furthermore, the high gaussicity occurs in a small fractional bandwidth. In the state-of-the-art a horn scalability analysis for achieving higher gains at different frequencies was not accomplished. In [11] the authors obtained a high gaussicity incidentally by optimizing for cross polarization and sidelobe level. In this section it is shown how optimizing for gaussicity alone can lead to not only broadband gaussicity but also better cross polarization discrimination and sidelobe levels.

7.2.1 Preliminary Antenna Design

The design of the split-block diagonal horn antenna is made taking into consideration the schematic model of Fig. 7.6, in which a top view of the split-block is shown. The spline depths y_i, where i is the index of the point of the spline are given by $y_i = k_i \cdot d$. The dimension d corresponds to the diagonal horn aperture and l to the horn length. The H-wall of the waveguide is given by $b = 0.4318$ mm for the case of the WR-3 interface considered in this work.

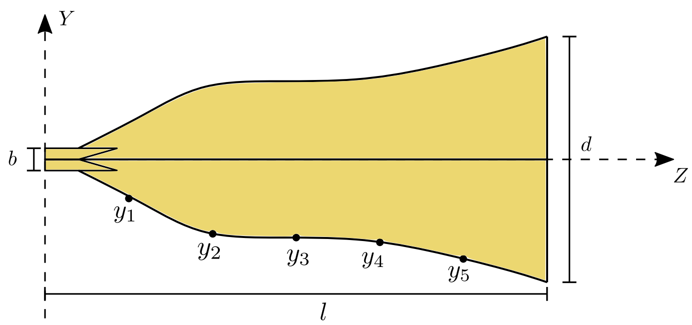

Figure 7.6: Preliminary antenna model (top view of one of the two split-blocks).

Since the waveguide interface has fixed dimensions, the PSO algorithm can act in variables d, l and k_i, which in turn will define variables y_i. For simulation time reduction, a fixed horn length of $l = 10$ mm was considered. The remaining variables k_i and d were used as the search space of the algorithm. Due to fabrication limitations, for spline depths that are not continuously decreasing, the solutions are discarded by the PSO. The boundaries of the search space are described in Table 7.2.

The remaining PSO parameters, namely the cognitive coefficient $c1 = 1.6$, the social coefficient $c2 = 1.6$ and the inertia coefficient $\omega = 0.3$, are set considering the recommendations of [47]. The number of particles (candidate solutions) is defined as $N = 100$, since according to [47] this will lead to a reduced number of iterations and potentiate a better search of the solution space.

Table 7.2: Solution space boundaries considered for the PSO algorithm.

Variable	Lower Bound	Upper Bound
k_1	0.03	0.2
k_2	0.08	0.25
k_3	0.18	0.3
k_4	0.2	0.4
k_5	0.3	0.5
d	5 mm	8 mm

The maximum number of iterations is set to 100, but a stopping condition is defined if the best objective function OF value suffers no change in 5 consecutive iterations.

The OF value calculation is obtained by considering the geometric mean of the gaussicities η_{g1}, η_{g2} and η_{g3} at 220, 275 and 330 GHz, respectively, written as

$$OF = \sqrt[3]{\eta_{g1} \cdot \eta_{g2} \cdot \eta_{g3}} \tag{7.4}$$

where the three gaussicities are used so that acceptable Gaussian beam launching capabilities are obtained in the full WR-3 band. The PSO algorithm is modified so that it can maximize the value of the objective function, instead of minimizing it.

Each gaussicity is calculated, as reported in [75], by the formula

$$\eta_g\,(\%) = 100 \times \frac{\left| \iint\limits_A \vec{E} \cdot \vec{g}^*\, dA \right|^2}{\iint\limits_A \vec{E} \cdot \vec{E}^*\, dA \cdot \iint\limits_A \vec{g} \cdot \vec{g}^*\, dA} \tag{7.5}$$

in which A represents the area over the horn aperture and $\vec{E}$ the electric field at the aperture. The fitting Gaussian curve, $\vec{g}$, is given by

$$\vec{g}(x,y) = e^{-\left(\frac{\sqrt{x^2+y^2}}{w}\right)^2} \hat{u} \tag{7.6}$$

where x and y correspond to the coordinates of the horn aperture. The co-polarization unit vector is denoted as $\hat{u}$ and w represents the Gaussian beam waist radius, which equivalently corresponds to the standard deviation and is the parameter enabling the fitting of the Gaussian curve to the calculated E-field. The standard deviation was calculated by taking into account the full width at half-maximum, $FWHM$, of the co-polarized E-field magnitude along the X and Y axes at the horn aperture. The radius w is then calculated as

$$w = \sqrt{\sigma_X \cdot \sigma_Y} \tag{7.7}$$

and relating the standard deviation in terms of the $FWHM$, yields

$$\sigma_{X,Y} = \frac{FWHM_{X,Y}^2}{4\ln(2)} \tag{7.8}$$

This method for calculating the gaussicity is checked by simulating the diagonal horn reported in [79] and comparing the calculated gaussicity of 83.7 % with the reported theoretical of 84.3 %. Since the values are in close agreement, the method is considered valid.

After running the PSO algorithm, the convergence plot of Fig. 7.7 is obtained, in which it can be seen that after 22 iterations, the objective function value settles around $OF \approx 93$. The variables which correspond to the optimal solution are $k_1 = 0.140$, $k_2 = 0.186$, $k_3 = 0.192$, $k_4 = 0.240$, $k_5 = 0.367$ and $d = 7.410\,\text{mm}$. The input reflection coefficient, S_{11}, the E- and H-plane co-polarization radiation patterns are shown in Figs. 7.8 and 7.9, respectively. No cross-polarization is considered, since symmetry boundaries were used to reduce simulation time, even though it will be considered in the final design. The calculated gaussicities of this optimized horn antenna are $\eta_{g1} = 91.13\,\%$ at 220 GHz, $\eta_{g2} = 93.12\,\%$ at 270 GHz and $\eta_{g3} = 93.84\,\%$ at 330 GHz. A peak gain of 20 dBi is obtained at 275 GHz. However, if more or less gain is required, the scaling of the proposed antenna is necessary. Such analysis is presented in the next section.

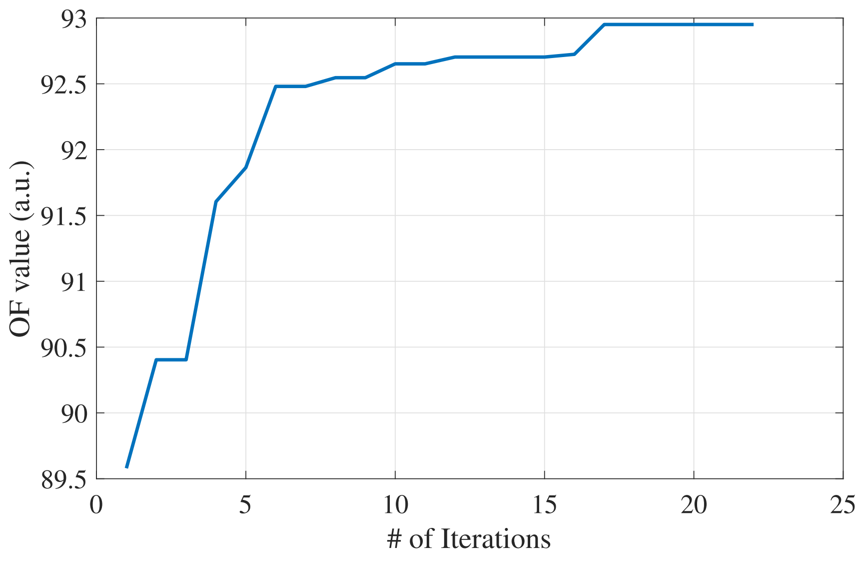

Figure 7.7: PSO convergence evolution with number of iterations.

7.2.2 Scalability Analysis

The scaling of the proposed horn antenna allows for a more flexible design depending on the needs in terms of gaussicity and gain. This analysis is done by sweeping the horn length, l, and its aperture, d. The horn length, l is swept from 3λ to 40λ, so that the analysis is valid when lower or higher gains are needed, respectively. Due to the fact that the field in the horn aperture is similar

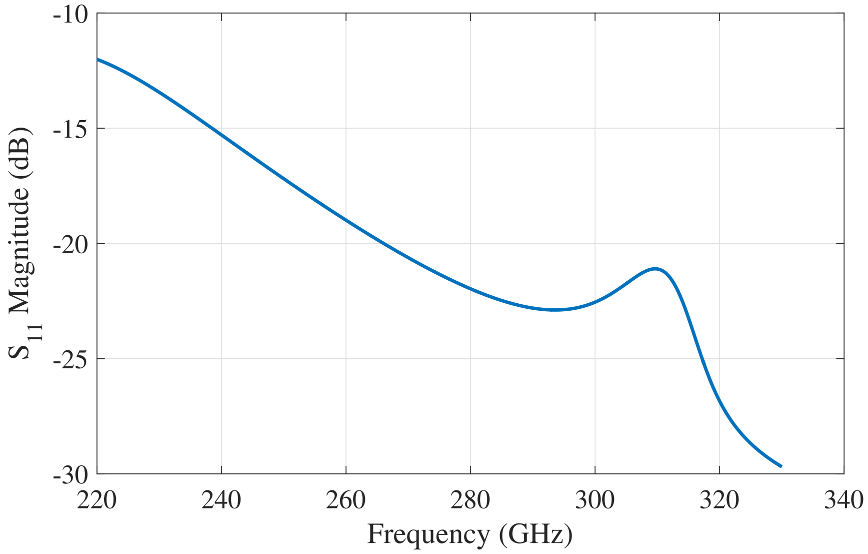

Figure 7.8: S_{11} magnitude as a function of frequency for preliminary horn design.

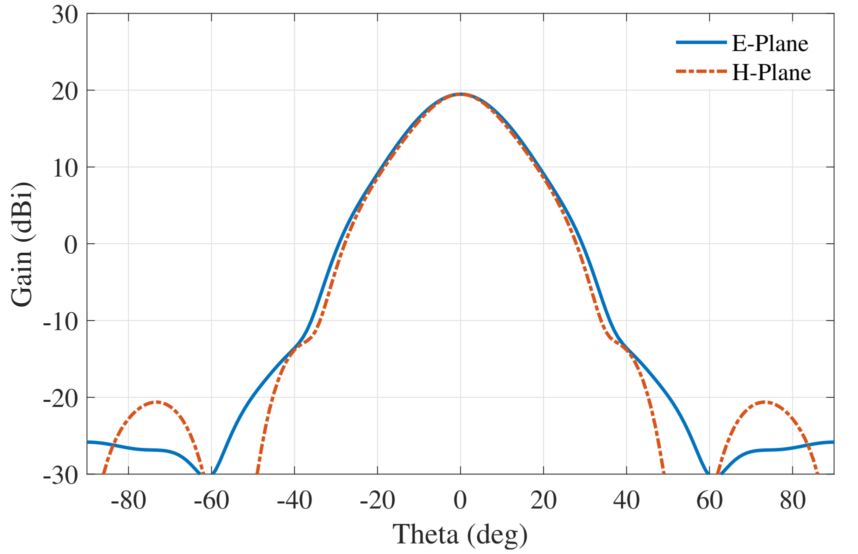

Figure 7.9: Antenna gain in E- and H-Plane as a function of theta scan angle for preliminary horn design.

to the field of a conical horn (TE_{11}), the fitting functions used were analogous to the ones used in the analysis of conical horns made in [12, pp. 756-759].

The first step of the scalability analysis is to determine the horn aperture that corresponds to the optimal gaussicity as a function of the horn length and wavelength considered for the gaussicity calculation. A square root function is used for curve fitting, which results in an optimal horn aperture given by the fitting function

$$d = \sqrt{5.15 \cdot l \cdot \lambda} \tag{7.9}$$

which is plotted in Fig. 7.10, alongside with the simulation data.

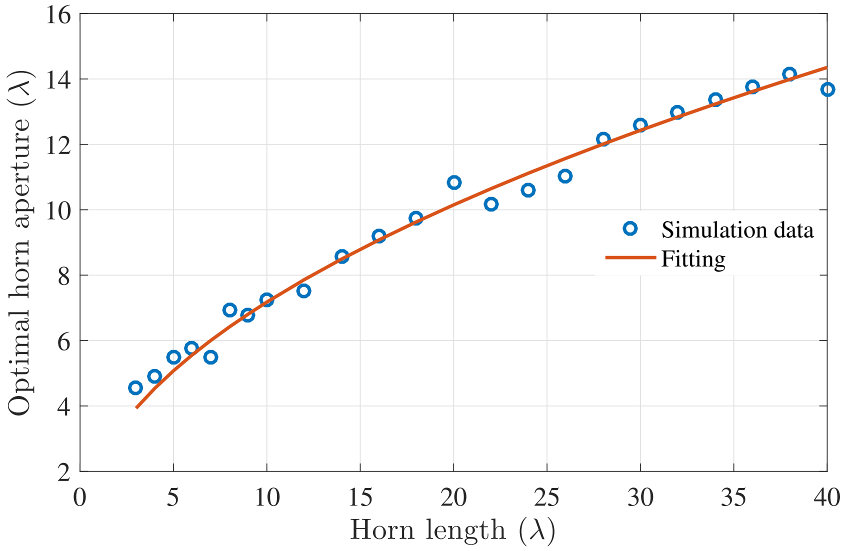

Figure 7.10: Optimal horn aperture as a function of horn length.

The scaling process under analysis is meant to allow the control of the gain of the antenna. Therefore, we analyse the gain of the proposed horn as a function of its length. Despite the fact that in [12, pp. 756-759] the analysis for conical horns is made in terms of the aperture, the length is used in this analysis because the optimal aperture is already being considered and its relation with the horn length is known. The gain in dBi of the horn as a function of its length was fitted to simulated data using

$$G\,(\mathrm{dBi}) = 10\log_{10}\left(9.486 \cdot \frac{l}{\lambda}\right) \tag{7.10}$$

The fitting function and the simulated data are plotted in Fig. 7.11.

The length and aperture scalability of the proposed horn also has an impact on the maximum gaussicity it can provide. Since the aperture E-field of a diagonal horn resembles the TE_{11} mode of a conical horn, mode coupling has to occur, so that mode conversion exists from the rectangular waveguide TE_{10} mode to the desired Gaussian mode. This mode conversion occurs with the waves propagating through the spline-profiled horn, which allows us to intuitively infer that reduced horn lengths will result in lower gaussicities, as the modes will have less chances to couple. It is verified that the maximum gaussicity tends to a limit, which can be explained by the fact that full mode conversion takes place after a specific horn length and increasing it further will not result in more mode conversion to take place. Therefore an exponential fitting curve is used, which can be written as

$$\eta_g = 0.96 - 0.09 \cdot e^{-0.12\frac{l}{\lambda}} \tag{7.11}$$

The fitting curve and the corresponding simulation data are shown in Fig. 7.12.

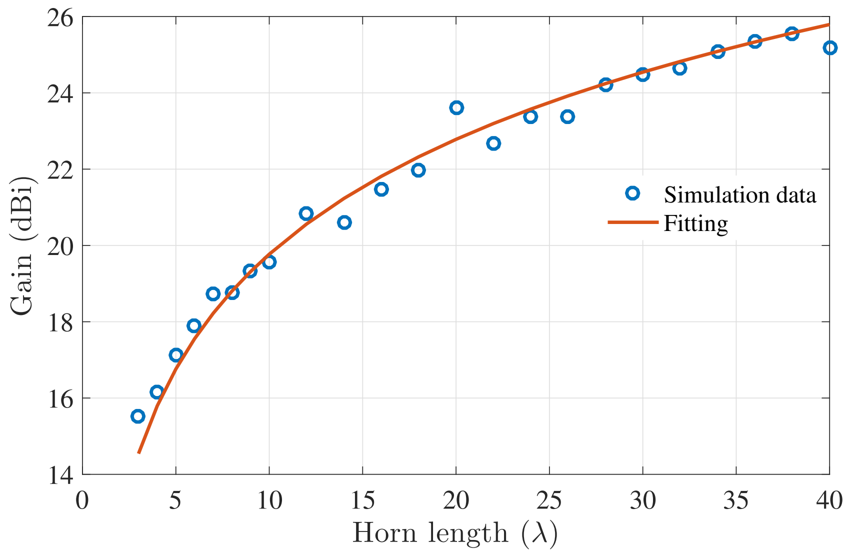

Figure 7.11: Horn gain as a function of horn length, considering optimal horn aperture.

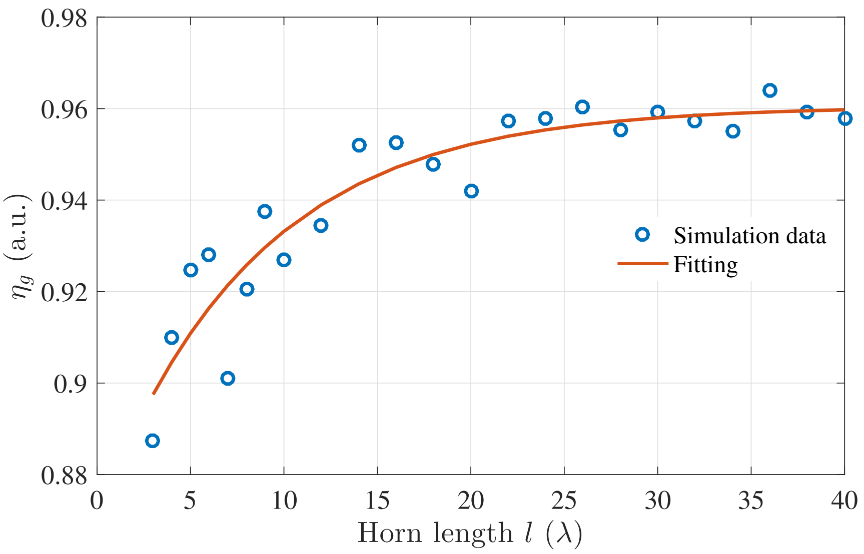

Figure 7.12: Gaussicity as a function of horn length, considering optimal horn aperture.

Due to the fact that the horn aperture is optimal for a specific wavelength and horn length, the gaussicity and gain will vary with frequency. Since the optimal aperture is considered to obtain peak gaussicity at a specific frequency, it is expected that this parameter will decrease for higher and lower frequencies. The scaling process that was derived is employed for the design of a spline-profiled horn, with optimal gaussicity at 275 GHz, in the next subsection.

7.2.3 Final Design

The requirements of the horn were set having in mind a final application where the antenna is to be integrated with WR-3 connected Schottky barrier diodes and are: a gain of at least 25 dBi and a gaussicity as high as possible in the entire WR-3 band.

Considering the scalable model derived in subsection 7.2.2, it is possible to infer that the gain increases with increasing frequency. Therefore the 25 dBi gain restriction must be fulfilled at 220 GHz, the lowest frequency of the WR-3 band. Plugging these values into equation (7.10), a horn length of $l \approx 45$ mm is obtained. Given the horn length, the aperture that results in maximum gaussicity at the centre frequency of 275 GHz can be calculated. Additionally, the use of equation (7.9) gives an horn aperture of $d \approx 15.9$ mm.

For computing cross-polarization patterns and better approximate the real behaviour of the physical antenna to be fabricated, a simulation of the full antenna model has to be performed. A finite conductivity of $\sigma = 2 \times 10^7$ S/m is considered for the waveguide and horn walls which corresponds to the gold alloy that will be used in the manufacturing process.

After simulation of the horn antenna, the input reflection coefficient is obtained as shown in Fig. 7.13. In the WR-3 band the S_{11} magnitude stays below -15 dB which allows us to state that the antenna is suitable for operation.

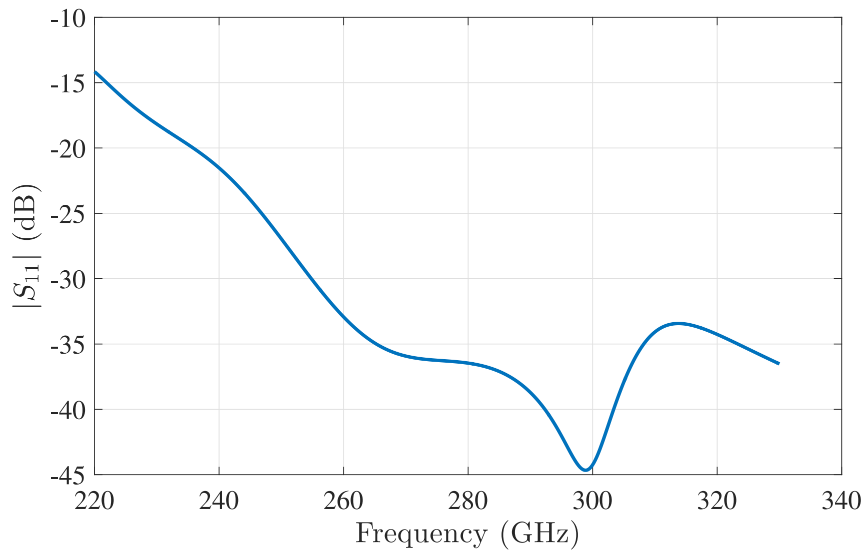

Figure 7.13: $|S_{11}|$ as a function of frequency for the full model simulation.

The co- and cross-polarization radiation patterns are shown in Figs. 7.14, 7.15 and 7.16. The XPD can be seen to be greater than 40 dB at all frequencies in the theta scan range where most of the radiation takes place. Nonetheless, it degrades for angles farther away from the desired radiation direction. These results show the advantage of using the gaussicity of the horn as the objective function to adjust its spline profile compared to when multiple optimization goals such as low side-lobes and reduced cross-polarization are used [11]. In Table 7.3 the gains, gaussicities and phase centre offset from the horn aperture to the inside of the horn are shown. The gaussicity peaks at the centre frequency as expected. Nonetheless, the phase centre which was not optimized also shifts significantly within the operating bandwidth. The gains are not only in compliance with the design requirements but also agree with the ones that can be obtained from the model derived in subsection 7.2.2. The gaussicity peaks at the centre frequency of 275 GHz and retains a high value in the WR-3 band. A full design of one of the split-blocks is shown in Fig. 7.17 where the mounting flange and screws are also visible.

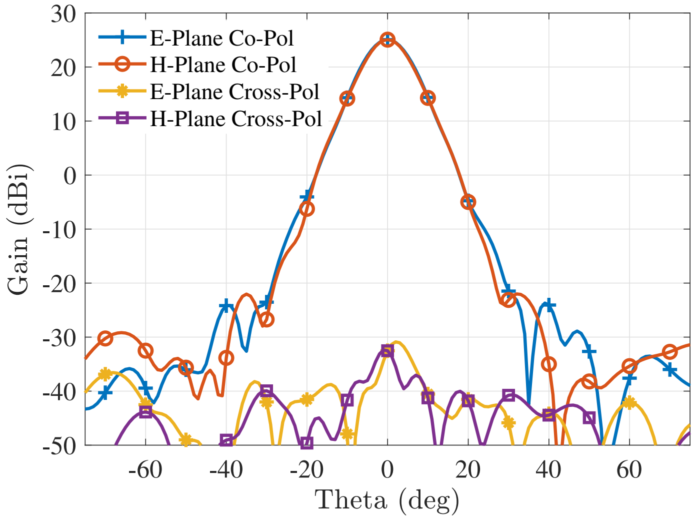

Figure 7.14: Simulated E-plane and H-plane co- and cross-polarization radiation patterns at 220 GHz.

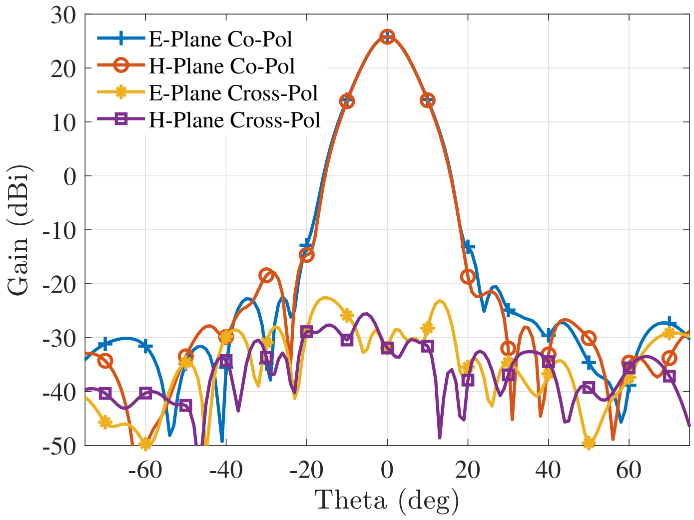

Figure 7.15: Simulated E-plane and H-plane co- and cross-polarization radiation patterns at 275 GHz.

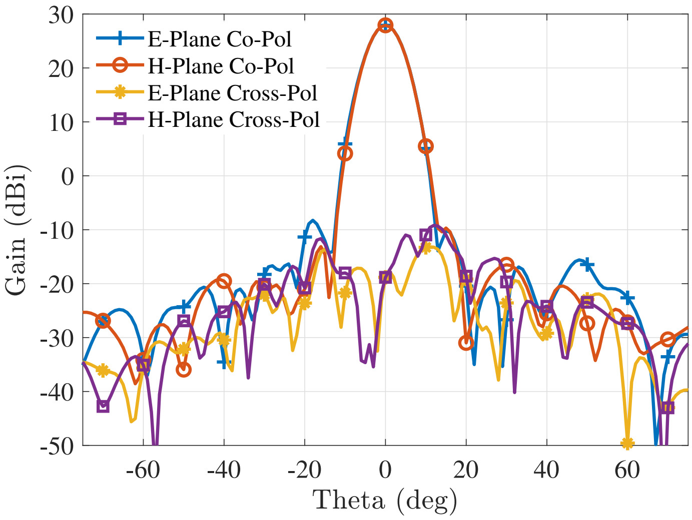

Figure 7.16: Simulated E-plane and H-plane co- and cross-polarization radiation patterns at 330 GHz.

Table 7.3: Field parameters for the start, centre and end frequencies of WR-3 band.

Parameter	220 GHz	275 GHz	330 GHz
η_g	91.4 %	95.9 %	91.1 %
Gain	25.1 dBi	25.8 dBi	27.9 dBi
PC_{offset}	20.9 mm	19.4 mm	15.8 mm

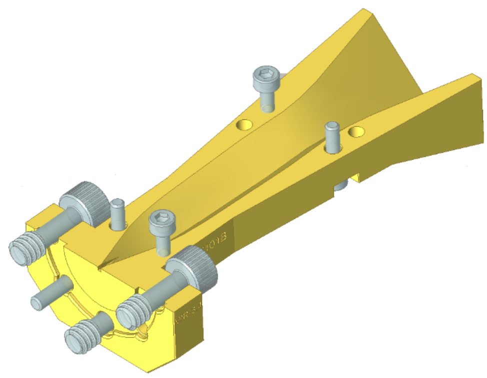

Figure 7.17: 3D model ready for fabrication of the proposed horn.

7.3 Summary

In this chapter, a spline-profiled horn was presented, for which a full scalability analysis was performed and validated through FEM simulations in HFSS. It was proven that by using the gaussicities in the operating frequencies as the objective function for optimizing the horn geometry, better XPD and SLL can be obtained, compared to when multiple optimization goals are used. It was proven that the design of a horn antenna with this profile can be done resorting simply to two closed-form expressions which is a significant advance in the state-of-the-art related to spline profiled horns.

Significant phase centre shifts were observed which may lead to defocusing problems when using this antenna with reflectors and lenses. In the future this problem has to be addressed, along with the possibility of including a second polarization for diversity and/or capacity gains.

Chapter 8

Design of an Anechoic Chamber for W-Band and mmWave

The term 5G refers to a variety of technologies that intend to create ultra-fast wireless connectivity aiming at 20 Gbps, extremely low latency, and significant improvement in users' perceived quality of service (QoS), compared to 4G Long Term Evolution (LTE) networks. 5G networks achieve these higher data rates by using higher frequencies, in or near the millimetre wave band from 30 to 300 GHz. These high frequencies, open up a wide spectrum for higher bandwidth channels that accommodate extremely high speeds. However, these changes imply significantly more base stations than needed when using lower frequencies because these type of waves tend to be quite short and easily obstructed by even small objects. In order to solve the problem, 5G will therefore necessitate a different architecture, using multiple smaller, low-power microcell base stations with Massive MIMO (multiple input, multiple output) antennas which are able to send and receive more data simultaneously, connecting more users at the same time to the network while maintaining high throughput.

Moreover, this change in frequency band also has implications in the process of antenna design since the antennas have very small dimensions when compared with antennas that use lower frequencies. At the same time, the radiation pattern measurement process, based on room-sized anechoic chambers is not adequate for these frequency bands due to large free space losses, resulting in lower measurement signal-to-noise ratio (SNR). In that sense it is necessary to re-design an anechoic chamber to measure the radiation pattern of this type of antennas. In this chapter the design of an anechoic chamber suitable for measurements at high frequencies, while maintaining low free-space losses is described. Additionally the quiet-zone assessment based on ray-tracing and geometrical optics simulations is also analysed.

8.1 Ray-Tracing Geometrical and Physical Optics Approximations

When an electrically large environment is being simulated, precise full-wave simulation methods such as Method of Moments (MoM), Finite Element Method (FEM) or Finite Differences on

Time Domain (FDTD) result in abnormally large matrices that consume large amounts of memory which are usually beyond consumer grade equipment [80]. Additionally the processing power is not enough for providing solutions in useful time using the aforementioned methods. Therefore, a different simulation method is required for electrically large structures.

The most suitable option for reducing simulation complexity and time is the usage of geometrical and physical optics approximations. Geometrical optics (GO) consists in launching rays from the transmitter to the geometry under simulation and calculating the reflected and transmitted rays using the well known Snell law and oblique incidence equations [81, pp. 352-360]. According to [80] the reflected field from a geometry can be understood as in Fig. 8.1, from where we can write the compact relation

$$\vec{E}^r = \begin{bmatrix} E_{\parallel}^r \\ E_{\perp}^r \end{bmatrix} = \begin{bmatrix} R_{\parallel\parallel} & R_{\parallel\perp} \\ R_{\perp\parallel} & R_{\perp\perp} \end{bmatrix} \begin{bmatrix} E_{\parallel}^i \\ E_{\perp}^i \end{bmatrix} \tag{8.1}$$

where we can see that the reflected field is basically a matrix multiplication of the scattering matrix with the incident field vector.

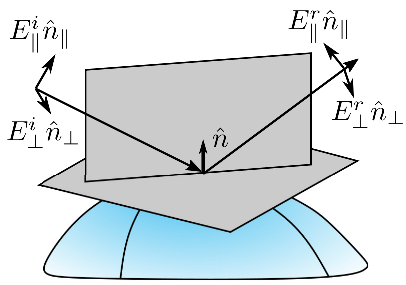

Figure 8.1: Reflected and incident rays at geometry interface. Adapted from [80].

Despite the low computational complexity of geometrical optics simulation methods, there are phenomena such as diffraction and creeping waves which can not be accounted for. Therefore, the physical optics (PO) approximation was created, which can be seen as an intermediate between geometrical optics and full wave simulation methods [82, pp. 11-13]. The physical optics approximation uses ray optics to find the field distributions on the geometry surfaces which are later used to calculate the transmitted and scattered fields. Furthermore, simulators such as Ansys Savant enable the integration of physical optics with uniform theory of diffraction (UTD) and creeping wave calculations. Altogether, these form a computationally efficient but accurate simulation method for electrically large structures at high frequencies, when others can not be used either due to computational requirements or simulation inaccuracy on the edges of simulated geometries. Such is important for the design of anechoic chambers at high frequencies where the available absorber pyramid sizes are typically electrically large.

8.2 Anechoic Chamber Design Considerations

In the design of wireless communication systems, it is a crucial issue to choose an antenna that meets the system requirements in terms of radiation pattern, directivity, bandwidth and polarization. To perform the study of antennas an echo free environment is required and for that purpose anechoic chambers are used.

Traditionally, indoor and outdoor measurements methods were used for this kind of study. The outdoor measurements take place in an open test area, which is weather dependent, suffering abundant reflections, interferences and scattering of EM field within the testing zone. On the contrary, indoor measurements are more accurate and require less space. For this type of measurements, a controlled RF quiet or echo free environment is commonly used, the anechoic chambers being filled with absorber materials. It was in 1953 that the first commercialization of microwave absorbers started, and in the same year the first anechoic chamber appeared under investigation being used for antenna measurements [83]. Before this, absorbers and anechoic chambers were mainly used for military purposes.

An anechoic chamber or anti-echo chamber can be defined as a chamber developed to reduce unwanted reflected energy, by the use of absorber materials providing a “virtual” free-space testing chamber. This special room is used to perform a variety of antenna measurements, electromagnetic interference (EMI) measurements, and electromagnetic compatibility (EMC) measurements, while providing minimal interference from external sources.

The attenuation of external, undesired signals that enter the chamber is achieved by having the outside of the chamber shielded by metal, reflecting the electromagnetic signals. If by some small gaps of the chamber signals enter inside it, absorbing materials in the inner walls, door, floor or ceiling, are used to greatly attenuate these signals.

At millimetre wave frequencies the external sources are rare, therefore the shielding of the chamber is optional. However, due to the high frequencies under consideration, the structures inside the chamber are electrically large, including the absorbers, which significantly impairs the design process as full-wave simulation methods are impossible. Furthermore, the connectivity between the network analyser and the source and antenna-under-test has to be carefully considered, due to the high cost and losses of coaxial cables. In this sense, the design of a chamber for such frequency bands, has to be optimized in order to be just the right size for the desired quiet zone. With this objective in mind the characteristics of the absorbers are of paramount importance, which are required to be known of measured before hand. This is discussed in the next section.

8.3 Radio Wave Absorber Characterization

Radio wave absorbers are the building blocks of anechoic chambers. Their geometry and materials are engineered to provide the absorption of radio waves that try to enter or exit the anechoic chamber. There are several common types of absorbers such as pyramidal, wedge, walkway foam absorbers and ferrite tiles. The performance of the selected absorber is determined by the reflection coefficient ρ, which is the relation between the magnitude of reflected E_r and incident E_i electric-fields of plane waves, given by:

$$\Gamma = \frac{E_r}{E_i} \tag{8.2}$$

Alternatively, the absorber performance can also be described by reflectivity R in decibels, given by:

$$R = 20\log(\Gamma) \tag{8.3}$$

The smaller the value of R (dB), the better the absorber performance. The reflections from absorbing material represent constructive or destructive interference at the receiving antenna, typically the antenna under test, hence the reason why they should be minimized.

The main type of absorbers are:

- Urethane Pyramidal Absorber
- Twisted urethane pyramids
- Wedge Absorber
- Ferrite Tiles and Grids
- Hybrid Absorber

The absorbers used in this chamber are the Emerson & Cuming WAVASORB VHP-8 which offer a guaranteed reflectivity of $-55\,\text{dB}$ for a perpendicularly incident plane wave in the frequency range of $40-110\,\text{GHz}$. They are available in tiles of 9×9 pyramids, each with a height of approximately $18\,\text{cm}$ and a base of $6.6\,\text{cm}\times6.6\,\text{cm}$. However, no other data such as permittivity, loss tangent and permeability is provided by the manufacturer. Therefore, before employing these absorbers in an EM simulation, their electrical properties have to be determined.

A technique has been widely used for the characterization of lossy dielectric materials, which consists of an open waveguide radiating to an half-space made of the dielectric under test [84–86]. The method is based on measuring the reflection coefficient of with the reference plane set in the waveguide aperture, and comparing it to the theoretical calculations obtained from modal solutions at the waveguide aperture. However, for mathematical simplicity, the waveguide is usually assumed to have an infinite plane at the aperture plane. According to [87], the waveguide flange can have a significant impact on such methods and effectively introduce measurement errors due to discontinuities. Considering the flange shown in Fig. 8.2, it is expected that significant deviations occur from the theoretical infinite ground-plane approximation, as multiple holes and discontinuities exist for proper mechanical attachment.

To correctly approximate the behaviour that the physical system will have, a simulation setup is assembled as schematically shown in Fig. 8.3. The simulation layout of the flange is shown in Fig. 8.4 where the mounting pins are not present, since they will not be in the measurements. This

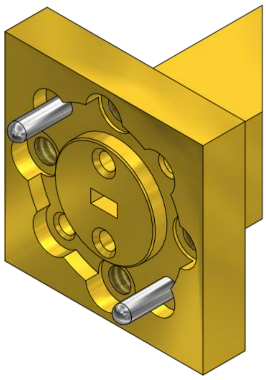

Figure 8.2: VDI waveguide flange [88].

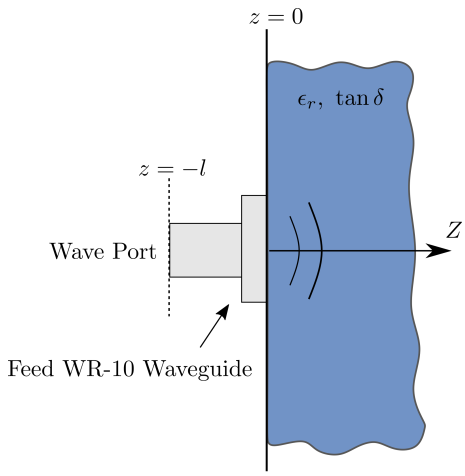

Figure 8.3: Representation of setup for absorber ε_r and tanδ characterization.

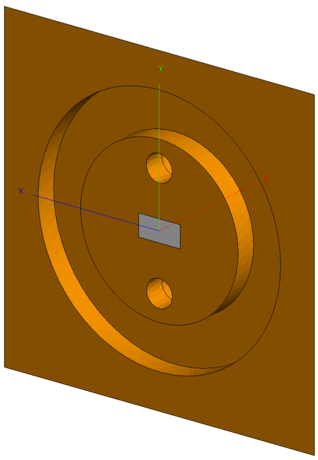

Figure 8.4: Simulation layout of WR-10 flange.

is because with these mounting pins, when the flange touched the absorber, small holes would be made every time and the method would be destructive.

As shown in Fig. 8.3 the reflection coefficient is obtained in simulation at a reference plane that is offset by l from the desired reference plane at the waveguide aperture, as will be the case in field measurements after calibration. To correct for this, one has to go through waveguide theory. By knowing that for a rectangular waveguide we have

$$h^2 = \left(\frac{m\pi}{a}\right)^2 + \left(\frac{n\pi}{b}\right)^2 \tag{8.4}$$

where $m = 1$ and $n = 0$ are the modal indexes for the mode in which we are operating (TE_{10}). For WR-10 the waveguide width $a = 2.54\,\text{mm}$ and its height $b = 1.27\,\text{mm}$. From this point we can calculate the propagation constant of the waveguide γ as

$$\gamma = \sqrt{h^2 - \omega^2 \mu \varepsilon} \tag{8.5}$$

where ω is the angular frequency, μ and ε are the magnetic permeability and electric permittivity of the waveguide filling medium, which is air in this case. Since the wave at $z = -l$ has to propagate to the aperture and back, we can obtain the reflection coefficient of the aperture as

$$\Gamma_{ap} = \frac{\Gamma}{e^{-2\gamma l}} \tag{8.6}$$

where Γ is the reflection coefficient before the de-embedding process.

To obtain the dielectric properties of the absorbers the aperture reflection coefficient must be measured using a VNA, which is represented as Γ_m. Using this reflection coefficient, the values of ε_r and $\tan\delta$ are estimated from the infinite ground plane approximation by using Ganchev's method reported in [85]. The absorbers are assumed to be non-magnetic and therefore $\mu_r = 1$. Afterwards the retrieved dielectric properties are fed into a Quasi-Newton algorithm, as the initial solution, whose objective function is simply

$$F = \left|\hat{\Gamma} - \Gamma_m\right| \tag{8.7}$$

using ε_r and $\tan\delta$ as the adjust variables set in the simulation model of Fig. 8.4, on which a full 3D MoM simulation is run and the estimate of the reflection coefficient $\hat{\Gamma}$ computed. A flowchart representation of the inverse problem resolution by iterative techniques is shown in Fig. 8.5. To obtain the electrical properties of the absorber, the accuracy was set so that when $F \leq 0.001$ the algorithm is considered to be converged.

An example of the measurement setup can be seen in Fig. 8.6. By employing the aforementioned methodology the absorbing material properties are obtained and shown in Table. 8.1.

Table 8.1: WAVASORB VHP-8 electrical properties at W-band.

Frequency	75 GHz	95 GHz	115 GHz
ε_r	1.55	1.47	1.29
$\tan\delta$	0.177	0.254	0.227

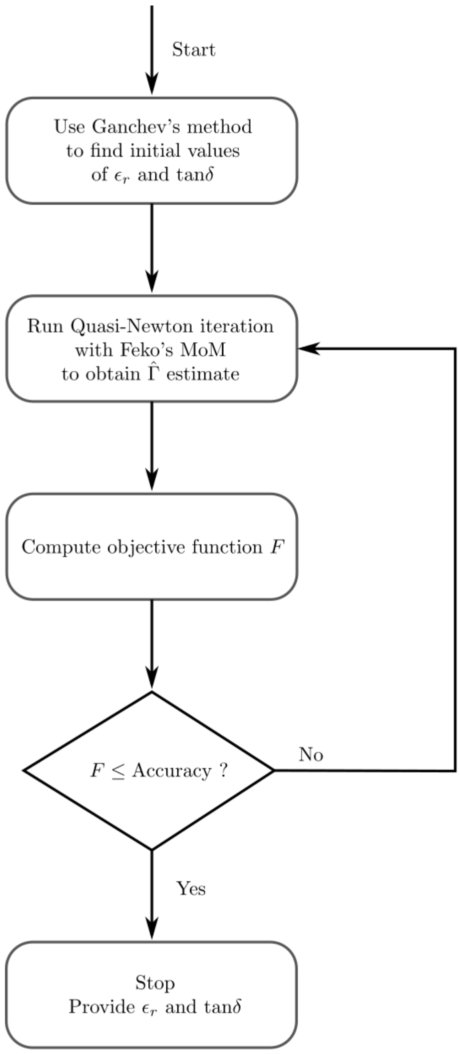

Figure 8.5: Flowchart for obtaining ε_r and tanδ.

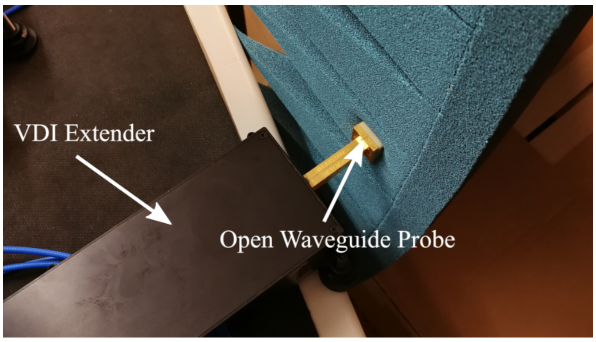

Figure 8.6: Open waveguide measurement setup of RF absorbers.

8.4 Chamber Design

Since a plane wave is required at the antenna test zone, the phase variation of the incident wave must be within a specified range. This allows one to define the chamber dimensions that result in a quasi-plane wave to be incident in the antenna test aperture.

According to [89, pp. 14-9] the curvature of the incident phase front can result in decreased resolution of the antenna measurement process. Considering Fig. 8.7, it is possible to relate the phase differences from the spherical wave to the plane of incidence with ΔR. As given in [89, pp. 14-8] we have

$$R^2 + \frac{D^2}{4} = (R + \Delta R)^2 \tag{8.8}$$

which, if ΔR^2 is neglected due to its small value, results in

$$\Delta R = \frac{D^2}{8R} \tag{8.9}$$

Converting the distance of equation (8.9) to a phase difference yields

$$\Delta\phi = \frac{2\pi}{\lambda}\Delta R = \frac{\pi D^2}{4\lambda R} \tag{8.10}$$

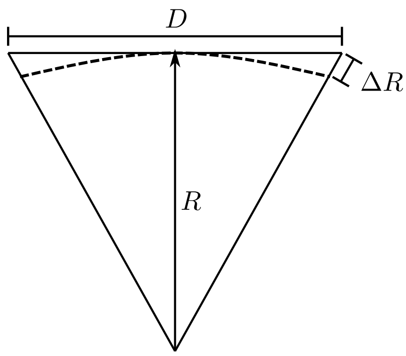

Figure 8.7: Spherical to plane wave front deviation.

The far-field condition is assumed when the phase difference of the radiated spherical wave to a plane wave is less than $\pi/8\,\mathrm{rad}$ [89], which equivalently can be represented as $R \geq 2D^2/\lambda$. However, in [89, pp. 14-10] the authors also show that in the case where the antenna separation is $R = 2D^2/\lambda$ the nulls of the measured antenna under test (AUT) radiation pattern deviate significantly from the values that would be obtained in an ideal infinite range. Therefore, to improve the performance of the chamber under design, the criterion of $R \geq 4D^2/\lambda$ is employed, which better approximates the infinite range condition, with a phase difference of $\Delta\phi \leq \pi/16\,\mathrm{rad}$.

To obtain a test aperture diameter of $D = 8\lambda = 32\,\mathrm{mm}$ at $75\,\mathrm{GHz}$, which ensures that even moderately large antennas can be tested, the minimum distance of the aperture to the phase centre of the source antenna can be obtained as

$$R = \frac{4D^2}{\lambda} \approx 1\,\mathrm{m} \tag{8.11}$$

Since the absorber tiles are $60\,\mathrm{cm} \times 60\,\mathrm{cm}$ in size, we can use a two tile length chamber, *i.e.*, make the chamber length to be $L = 1.2\,\mathrm{m}$. According to [90], to have an incidence angle of less than 60°

in the main specular point, the chamber width should be at least $W = L/2 = 60\,\mathrm{cm}$, which in this case will be only one absorber tile. Equivalently, the chamber height is also selected to be equal to the width $H = W = 60\,\mathrm{cm}$.

Given these conditions, the chamber is designed to have the required width and length, as shown schematically in Fig. 8.8. In the next section the quiet zone of the designed chamber is assessed using PO/UTD simulation in Ansys Savant.

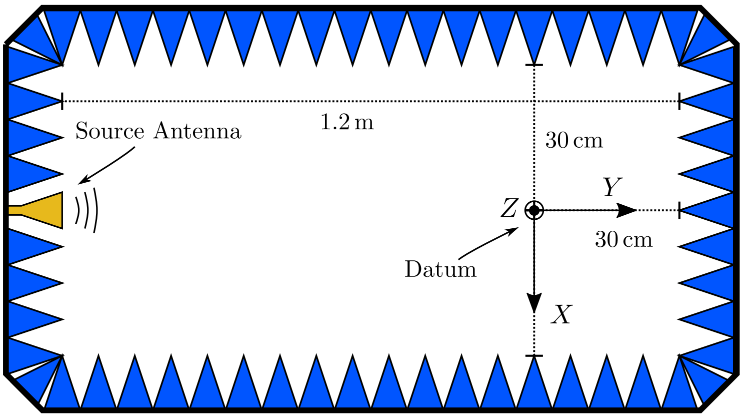

Figure 8.8: Chamber design schematic cross section.

8.5 Quiet Zone Simulation Assessment

The testing zone of an anechoic chamber must meet a set of requirements for antenna measurements to be feasible. Namely, the incident field phase should be as constant as possible, so that plane wave assumption is valid. This was addressed in the previous section, which led to the specification of the chamber dimensions. Furthermore, the taper of the field amplitude in the test aperture must be below a specified level, which depends on the measurement error one can tolerate. The reflections coming from the absorbing pyramids result in ripple occurring along the test aperture. This in turn has a direct relation to the amplitude of the field reflected by the absorbers in the chamber [89, pp. 14-48]. The zone in which all of these requirements are met is called the quiet zone.

The model shown in Fig. 8.9 is assembled in Ansys Savant for simulation. The incident and reflected fields are output by the PO/UTD simulator in the 3D volume in yellow with $10\,\mathrm{cm} \times 10\,\mathrm{cm} \times 10\,\mathrm{cm}$ centred on the datum point. This volume allows an acceptable simulation time whilst representing enough space for evaluating the quiet zone location. A limit of two bounces for the rays is defined, which ensures reduced memory usage and enough accuracy [91].

As stated before, three conditions have to be met so that a specific volume is suitable for antenna testing. Such assessment is done by post-processing in MATLAB the resultant fields obtained by the simulator. The phase stability requirement is settled as in section 8.4, where only the set of points in which $\Delta\phi \leq \pi/16\,\mathrm{rad}$ is considered. The field amplitude must be constant along the plane of incidence, so that deviations from the measured and ideal infinite range pattern

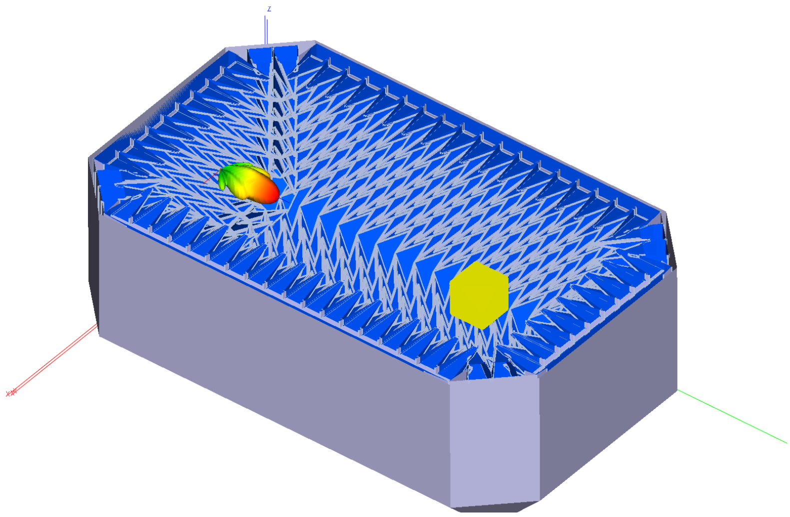

Figure 8.9: Simulation model used in Ansys Savant for PO/UTD simulation (top part of the chamber removed for visualization purposes).

are minimized. As reported in [89], a field amplitude tapper of less than 0.25 dB produces typical gain deviations of less than 0.1 dB which is satisfactory, therefore this is used as our quantitative requirement. Likewise, the reflections that occur on the absorbers, produce a ripple in the field incident in the test zone, which in turn also results in excessive deviations of the measured radiation pattern. An incident field peak-to-peak ripple of less than 0.2 dB is set, which results in reflected fields being 40 dB below the incident fields [89].

Two simulations for two different source antennas were carried out for three frequencies in W-band, namely 75, 95 and 115 GHz. The first source antenna being simulated is a 20 dBi horn [92]. The resulting quiet zone, considering the requirements defined earlier, is plotted in Fig. 8.10, where the origin corresponds to the datum point. As it is shown, there is no quiet zone at 75 nor at 95 GHz. Additionally, at 115 GHz only some points exist where the quiet zone restrictions are met. This allows one to discard this horn as a source antenna and conclude that due to its wide beamwidth, the amplitude ripple level is too high. Hence, a second horn antenna with 25 dBi [93] is tested and the resulting quiet zone is shown in Fig. 8.11. In this case, a cylindrically shaped quiet zone is obtained at negative Y offset from the datum. The cylinder has a diameter of approximately 30 mm and a height of 50 mm from the datum in direction to the negative part of the Y axis. Since at 95 and 115 GHz the quiet zones span the whole Y axis, we can infer that 75 GHz is the frequency which defines the quiet zone limitation. The cylinder diameter is expected to have such value, as rewriting equation (8.11) for a wavelength λ corresponding to 75 GHz in terms of D considering $R = 0.9\,\mathrm{m}$ yields

$$D = \sqrt{\frac{R\lambda}{4}} = 30\,\mathrm{cm} \tag{8.12}$$

which is approximately the value obtained by simulation.

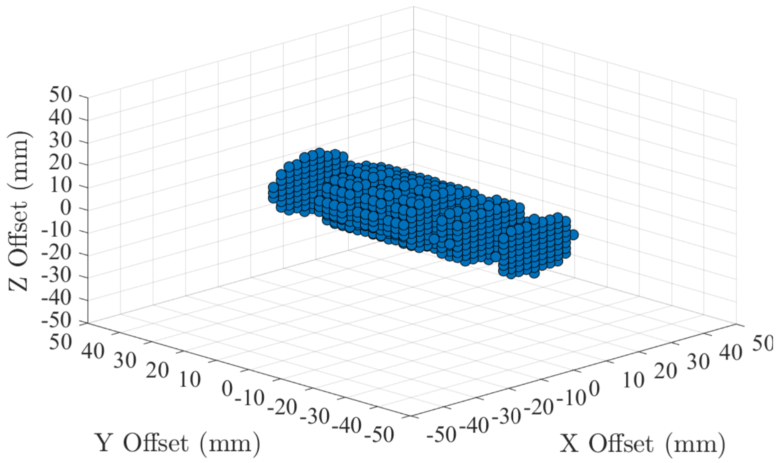

Figure 8.10: Simulated quiet zone for 20 dBi source antenna at 115 GHz.

Given that with a source antenna with a gain of 25 dBi a satisfactory quiet zone can be obtained, the chamber is assembled for fabrication as shown in Fig. 8.12.

8.6 Summary

In this chapter a full design of an electrically large anechoic chamber was presented. A method to retrieve the electrical properties of dielectric materials was also reported, for the case in which waveguide flanges' geometries are complex and other methods, such as the case in which infinite ground-plane is used, start to introduce significant errors. It was verified that the usage of PO/UTD simulation can produce results close to the theoretical expectations and that it can be easily used for evaluating different source antennas, when electrically large absorbers are used. This opens new ground for the design of anechoic chambers at high frequencies as in the case of millimetre wave, which ultimately can be designed in a much more cost efficient manner.

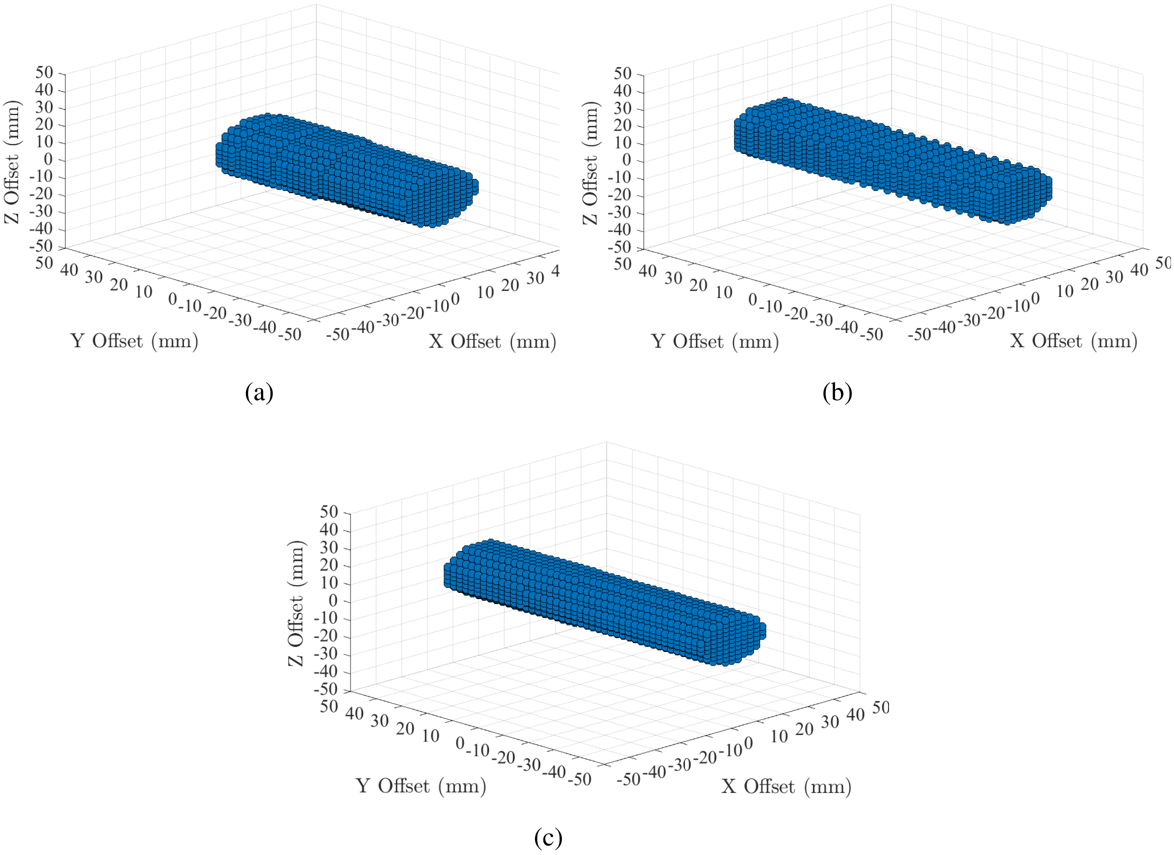

Figure 8.11: Simulated quiet zone for 25 dBi source antenna at (a) 75, (b) 95 and (c) 115 GHz.

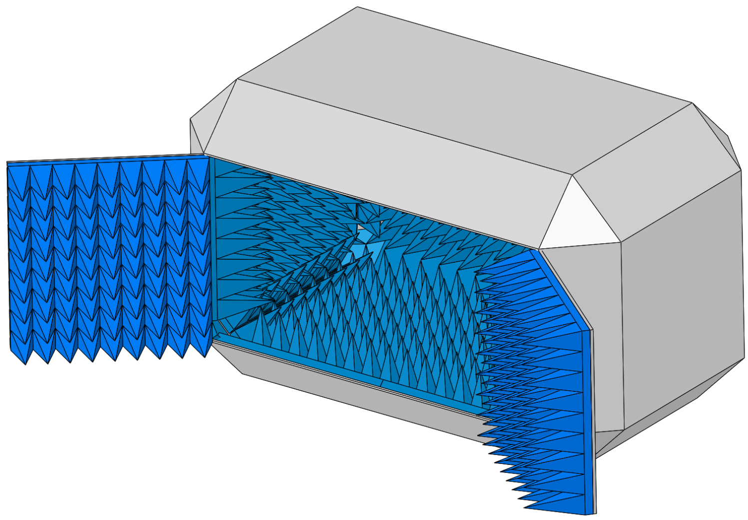

Figure 8.12: Anechoic chamber with doors for access to AUT.

Chapter 9

Conclusions and Future Work

9.1 Conclusions

In this thesis a set of antennas developed with focus on integration with active devices, ranging from S-band to sub-THz frequencies, were presented. Various connection types were analysed, depending on frequency range and antenna type, including eWLB packaging, land-side die attach flip-chip and waveguide. An anechoic chamber was also designed using physical optics to measure antennas from 75 GHz upward to millimetre waves. This work paved new ground for future generation communications and showed the importance of focusing not only on the design of the antennas alone but also their final application and installation which usually results in performance differences.

Chapter 3 described a monopole miniaturized antenna-in-package for Bluetooth Low Energy applications in which a high miniaturization factor was obtained in both the radiating element and ground-plane. This resulted in the smallest antenna-in-package when compared to the state-of-the-art for S-band, to the extent of the author's knowledge.

Chapter 4 showed a patch antenna for 5G NR communications in Ka-band ($24.25-27.5$ GHz). The antenna is easily manufactured in flip-chip land-side die attach technology for future applications in mobile market. It was shown how a dual-polarized antenna can be obtained with high isolation for being able to support polarization diversity MIMO. It has been proven that differential feeding reinforces antenna fundamental modes and cancels common-mode interferences of adjacent modes.

Chapter 5 demonstrated the design of a series-fed patch array for automotive radar applications in W-band ($75-79$ GHz). A remarkable performance with low sidelobe levels and no beam squint in the full operating bandwidth was obtained by feeding the array differentially enforcing field symmetry. The final installation of the developed antenna was also analysed when placed in the front bumper of a vehicle, which was proven to have an impact on its performance.

Chapter 6 described the design of an on-chip elliptical monopole antenna for integration with RTD based oscillators. Due to the fact that high permittivity substrates such as indium phosphide needed to be used, we showed how ground-plane shaping and substrate thinning and dicing can be used to achieve air-side radiation with a high efficiency without the usage of lenses. This is a great advance for future sixth generation and beyond sub-THz communications as cheap communication devices, that can serve both as transmitters and receivers, can be easily integrated in mobile device technologies.

Chapter 7 showed the design of a spline profiled horn antenna that is capable of achieving broadband gaussian beams suitable for quasi-optical processing. This is needed for directivity enhancement and beam shaping to improve flexibility in the design of high bit-rate wireless communication systems in data centers. We described a process based in heuristics to optimize and scale the antenna in both gain and operating frequency whilst maintaining high gaussian coupling efficiencies.

In Chapter 8 the design of an anechoic chamber was reported for frequencies above 75 GHz. A method based on physical optics was employed to determine the chamber quiet-zone and optimize absorber count and ultimately cost efficiency. A new approach based on feeding back measurement data into the simulation of complex open waveguide flanges was also analysed, for the quick characterization of the electric properties of lossy dielectrics.

The objectives of this thesis were achieved as we were able to provide contributions the state-of-the-art in key points for the development of new communication solutions at four bands of interest. With this work and further development of the presented designs, advances in IoT, mobile, automotive and very high throughput communications are now possible.

9.2 Future Work

Despite the success of the presented antenna topologies, in the design of packaged antennas, a limitation was identified from the beginning. The integrated circuits and their proximity to the radiating structures can greatly influence the electromagnetic behaviour of the antenna due to their metallizations and doped substrates. However, simulating all the ICs with the antenna is impossible as very large amounts of memory and processing power are needed due to the heterogeneity of the simulation model. Therefore, a simplified simulation method capable of considering the ICs close to the antenna must be developed.

Considering the antennas for 5G NR communications in Ka-band it is important to develop the proposed topology in even cheaper packaging technologies such as eWLB, since flip-chip is still expensive even for consumer grade products. However, due to limited layer count and fixed material properties, this might be extremely complex. The same approach must be followed for the integration in a system-in-package of the W-band series feed array reported in chapter 5. This can be even more intricate because of the higher frequencies involved.

On-chip antennas for sub-THz frequencies are typically designed resorting to lenses so that air-side radiation can be obtained. In our case we showed that proper dicing and thinning of the substrate together with adequate antenna design can also achieve air-side radiation. Nonetheless, wafer substrate thinning is a complex and expensive procedure. Because of this, other approaches such as benzocyclobutene (BCB) substrates in which artificial magnetic conductors can be designed below the monopole to achieve air-side radiation and avoid radiation from going into the InP substrate, should be considered.

Despite the performance described in chapter 7 of a spline profiled horn antenna at sub-THz frequencies, a significant problem rose regarding the antenna phase centre. The phase centre of the antenna is shifting considerably as frequency increases from the bottom to the upper part of the WR-3 band. Another approach may be taken in which the phase centre stability is also included in the optimization process of the spline profile. Additionally, adding a second data stream in an orthogonal polarization is attractive as it can theoretically double the data-rate that one can achieve with this antenna in a MIMO configuration.

References

[1] K. Chen, L. Chua, W. K. Choi, S. G. Chow, and S. W. Yoon, "28nm CPI (Chip/Package Interactions) in Large Size eWLB (Embedded Wafer Level BGA) Fan-Out Wafer Level Packages," in *2017 IEEE 67th Electronic Components and Technology Conference (ECTC)*, pp. 581–586, May 2017.

[2] L. S. H. Lee, L. I. S. Kang, Y. T. Kwon, T. H. Kim, J. H. Kim, E. J. Lee, and J. K. Lee, "FOWLP technology as wafer level system in packaging (SiP) solution," in *2017 International Conference on Electronics Packaging (ICEP)*, pp. 491–493, April 2017.

[3] Y. H. Chou, P. C. Pan, C. Y. Huang, M. F. Jhong, and C. C. Wang, "The Comparison of Package Design and Electrical Analysis in Mobile Application," in *2017 IEEE 67th Electronic Components and Technology Conference (ECTC)*, pp. 1855–1860, May 2017.

[4] K. Chang, "Bluetooth: a viable solution for IoT? [Industry Perspectives]," *IEEE Wireless Communications*, vol. 21, pp. 6–7, December 2014.

[5] T. Tjelta, S. Temple, and R. W. Mohr, "Euro-5G–Supporting the European 5G Initiative," 2015.

[6] J. Du, K. So, Y. Ra, S. Jung, J. Kim, S. Y. Kim, S. Woo, H. Kim, Y. Ho, and W. Paik, "Dual-polarized patch array antenna package for 5G communication systems," in *2017 11th European Conference on Antennas and Propagation (EUCAP)*, pp. 3493–3496, March 2017.

[7] Y. Lu, B. Fang, H. Mi, and K. Chen, "Mm-Wave Antenna in Package (AiP) Design Applied to 5th Generation (5G) Cellular User Equipment Using Unbalanced Substrate," in *2018 IEEE 68th Electronic Components and Technology Conference (ECTC)*, pp. 208–213, May 2018.

[8] T. Tjelta, S. Temple, and R. W. Mohr, "Euro-5g–Supporting the European 5G Initiative," 2015.

[9] A. Bisognin, D. Titz, F. Ferrero, C. Luxey, G. Jacquemod, R. Pilard, F. Gianesello, D. Gloria, and P. Brachat, "Differential feeding technique for mm-wave series-fed antenna-array," *Electronics Letters*, vol. 49, pp. 918–919, July 2013.

[10] K. H. Alharbi, A. Khalid, A. Ofiare, J. Wang, and E. Wasige, "Diced and grounded broadband bow-tie antenna with tuning stub for resonant tunnelling diode terahertz oscillators," in *IET Colloquium on Millimetre-Wave and Terahertz Engineering Technology 2016*, pp. 1–4, March 2016.

[11] H. J. Gibson, B. Thomas, L. Rolo, M. C. Wiedner, A. E. Maestrini, and P. de Maagt, "A novel spline-profile diagonal horn suitable for integration into thz split-block components," *IEEE Transactions on Terahertz Science and Technology*, vol. 7, pp. 657–663, Nov 2017.

[12] C. Balanis, *Antenna Theory: Analysis and Design*. Wiley, 2016.

[13] "IEEE Standard for Definitions of Terms for Antennas," *IEEE Std 145-2013 (Revision of IEEE Std 145-1993)*, pp. 1–50, March 2014.

[14] K. Fujimoto and H. Morishita., *Modern Small Antennas*. Cambridge University Press, 2014.

[15] H. A. Wheeler, "Fundamental Limitations of Small Antennas," *Proceedings of the IRE*, vol. 35, pp. 1479–1484, Dec 1947.

[16] J. S. McLean, "A re-examination of the fundamental limits on the radiation Q of electrically small antennas," *IEEE Transactions on Antennas and Propagation*, vol. 44, pp. 672–676, May 1996.

[17] S. R. Best, "Low Q electrically small linear and elliptical polarized spherical dipole antennas," *IEEE Transactions on Antennas and Propagation*, vol. 53, pp. 1047–1053, March 2005.

[18] C. Hsu and H. Song, "Design, Fabrication, and Characterization of a Dual-Band Electrically Small Meander-line Monopole Antenna for Wireless Communications," *International Journal of Electromagnetics and Applications*, vol. 3, no. 2, pp. 27–34, 1926.

[19] J. Jeon, K. Jang, S. Kahng, and C. Park, "Design of a miniaturized UHF-band Zigbee antenna applicable to the M2M/IoT communication," in *2014 IEEE Antennas and Propagation Society International Symposium (APSURSI)*, pp. 382–383, July 2014.

[20] H. Liu, Y. Cheng, and M. Yan, "Electrically Small Loop Antenna Standing on Compact Ground in Wireless Sensor Package," *IEEE Antennas and Wireless Propagation Letters*, vol. 15, pp. 76–79, 2016.

[21] L. Lizzi, F. Ferrero, P. Monin, C. Danchesi, and S. Boudaud, "Design of miniature antennas for IoT applications," in *2016 IEEE Sixth International Conference on Communications and Electronics (ICCE)*, pp. 234–237, July 2016.

[22] P. Vainikainen, J. Ollikainen, O. Kivekas, and K. Kelander, "Resonator-based analysis of the combination of mobile handset antenna and chassis," *IEEE Transactions on Antennas and Propagation*, vol. 50, pp. 1433–1444, Oct 2002.

[23] L. Qu, H. Piao, Y. Qu, H. Kim, and H. Kim, "Dual-resonance-based wideband antenna for integrated module applications," *Electronics Letters*, vol. 54, no. 8, pp. 474–476, 2018.

[24] K.-L. Wong and C.-H. Chang, "Surface-mountable EMC monopole chip antenna for WLAN operation," *IEEE Transactions on Antennas and Propagation*, vol. 54, pp. 1100–1104, April 2006.

[25] H.-W. Liu, T.-Y. Chen, C.-F. Yang, S.-T. Lin, S.-S. Tasi, C.-W. Chiu, and C.-L. Hu, "A miniature chip antenna without empty space on PCB for 2.4GHz ISM band applications," in *2008 IEEE Antennas and Propagation Society International Symposium*, pp. 1–4, July 2008.

[26] C. H. Lee, T. C. Tang, and K. H. Lin, "Stacked package loop antenna for WLAN based on IPD manufacturing technology," in *Proceedings of the 2012 IEEE International Symposium on Antennas and Propagation*, pp. 1–2, July 2012.

[27] Insight SiP, *High Performance Bluetooth 5 Ready, NFC & ANT Low Energy Module with MCU & Antenna*, October 2017.

[28] M. Jeangeorges, R. Staraj, C. Luxey, P. L. Thuc, C. E. Hassani, and P. Ciais, "Antenna miniaturization and integration in a 2.4 GHz system in package," in *Proceedings of the Fourth European Conference on Antennas and Propagation*, pp. 1–4, April 2010.

[29] NORDIC Semiconductor, *nRF52832 Product Specification v1.4*, 2017. Rev. 1.4.

[30] T. Endo, Y. Sunahara, S. Satoh, and T. Katagi, "Resonant frequency and radiation efficiency of meander line antennas," *Electronics and Communications in Japan (Part II: Electronics)*, vol. 83, no. 1, pp. 52–58, 2000.

[31] Z. Hu, P. H. Cole, and L. Zhang, "A method for calculating the resonant frequency of meander-line dipole antenna," in *2009 4th IEEE Conference on Industrial Electronics and Applications*, pp. 1783–1786, May 2009.

[32] M. A. Othman, T. M. Abuelfadl, and A. M. E. Safwat, "Dual-band inductively-loaded miniaturized antenna," in *Proceedings of the 2012 IEEE International Symposium on Antennas and Propagation*, pp. 1–2, July 2012.

[33] H. Oraizi and B. Rezaei, "Dual-Banding and Miniaturization of Planar Triangular Monopole Antenna by Inductive and Dielectric Loadings," *IEEE Antennas and Wireless Propagation Letters*, vol. 12, pp. 1594–1597, 2013.

[34] Y. Yu, Y. Wang, and R. Wang, "Miniaturized printed antenna with dual inductor-loaded monopoles for mobile terminals," in *2016 IEEE MTT-S International Wireless Symposium (IWS)*, pp. 1–3, March 2016.

[35] W. Choi, H. W. Son, C. Shin, J.-H. Bae, and G. Choi, "RFID tag antenna with a meandered dipole and inductively coupled feed," in *2006 IEEE Antennas and Propagation Society International Symposium*, pp. 619–622, July 2006.

[36] J. Oh and K. Sarabandi, "Low Profile, Miniaturized, Inductively Coupled Capacitively Loaded Monopole Antenna," *IEEE Transactions on Antennas and Propagation*, vol. 60, pp. 1206–1213, March 2012.

[37] A. E. Abdulhadi and R. Abhari, "Design and Experimental Evaluation of Miniaturized Monopole UHF RFID Tag Antennas," *IEEE Antennas and Wireless Propagation Letters*, vol. 11, pp. 248–251, 2012.

[38] G. Guo, L. Wu, Y. Zhang, and J. Mao, "Stacked patch array in LTCC for 28 GHz antenna-in-package applications," in *2017 IEEE Electrical Design of Advanced Packaging and Systems Symposium (EDAPS)*, pp. 1–3, Dec 2017.

[39] C. A. Balanis, *Modern antenna handbook*. John Wiley & Sons, 2011.

[40] H. Xia, T. Zhang, L. Li, and F. Zheng, "A low-cost dual-polarized 28 GHz phased array antenna for 5G communications," in *2018 International Workshop on Antenna Technology (iWAT)*, pp. 1–4, March 2018.

[41] G. Kumar and K. Ray, *Broadband Microstrip Antennas*. Artech House antennas and propagation library, Artech House, 2003.

[42] H. Nawaz and I. Tekin, "Dual Polarized, Differential Fed Microstrip Patch Antennas with very High Inter-port Isolation for Full Duplex Communication," *IEEE Transactions on Antennas and Propagation*, vol. PP, no. 99, pp. 1–1, 2017.

[43] K. M. Mak, H. W. Lai, and K. M. Luk, "A 5G Wideband Patch Antenna with Antisymmetric L-shaped Probe Feeds," *IEEE Transactions on Antennas and Propagation*, vol. PP, no. 99, pp. 1–1, 2017.

[44] B. Polyak, "Newton's method and its use in optimization," *European Journal of Operational Research*, vol. 181, pp. 1086–1096, 09 2007.

[45] D. Pozar, *Microwave Engineering, 4th Edition*. Wiley, 2011.

[46] Y. Wu, Y. Liu, and S. Li, "A Dual-Frequency Transformer for Complex Impedances With Two Unequal Sections," *IEEE Microwave and Wireless Components Letters*, vol. 19, pp. 77–79, Feb 2009.

[47] F. Marini and B. Walczak, "Particle swarm optimization (PSO). A tutorial," *Chemometrics and Intelligent Laboratory Systems*, vol. 149, pp. 153–165, 2015.

[48] Z. Tong, C. Wagner, R. Feger, A. Stelzer, and E. Kolmhofer, "A novel differential microstrip patch antenna and array at 79 GHz," in *Proc. Int. Antennas Propag. Symp.*, pp. 276–280, 2008.

[49] J. Yan, H. Wang, J. Yin, C. Yu, and W. Hong, "Planar series-fed antenna array for 77 GHz automotive radar," in *2017 Sixth Asia-Pacific Conference on Antennas and Propagation (APCAP)*, pp. 1–3, Oct 2017.

[50] J. Xu, W. Hong, H. Zhang, G. Wang, Y. Yu, and Z. H. Jiang, "An Array Antenna for Both Long- and Medium-Range 77 GHz Automotive Radar Applications," *IEEE Transactions on Antennas and Propagation*, vol. 65, pp. 7207–7216, Dec 2017.

[51] W. A. Ahmad, J. Lu, D. Kissinger, and H. Jalli Ng, "Beam squinting in wideband 60 GHz on-board series-fed differential patch arrays," in *2017 IEEE Asia Pacific Microwave Conference (APMC)*, pp. 13–16, Nov 2017.

[52] W. Wei and X. Wang, "A 77 GHz Series Fed Weighted Antenna Arrays with Suppressed Sidelobes in E-and H-Plane," *Progress In Electromagnetics Research*, vol. 72, pp. 23–28, 2018.

[53] C. Zhang, Q. Lai, and C. Gao, "Measurement of active S-parameters on array antenna using directional couplers," in *2017 IEEE Asia Pacific Microwave Conference (APMC)*, pp. 1167–1170, Nov 2017.

[54] J. E. Rayas-Sanchez and V. Gutierrez-Ayala, "A general EM-based design procedure for single-layer substrate integrated waveguide interconnects with microstrip transitions," in *2008 IEEE MTT-S International Microwave Symposium Digest*, pp. 983–986, June 2008.

[55] Z. Kordiboroujeni and J. Bornemann, "New Wideband Transition From Microstrip Line to Substrate Integrated Waveguide," *IEEE Transactions on Microwave Theory and Techniques*, vol. 62, pp. 2983–2989, Dec 2014.

[56] T. Djerafi, A. Patrovsky, K. Wu, and S. O. Tatu, "Recombinant waveguide power divider," *IEEE Transactions on Microwave Theory and Techniques*, vol. 61, pp. 3884–3891, Nov 2013.

[57] J. J. Simpson, A. Taflove, J. A. Mix, and H. Heck, "Substrate integrated waveguides optimized for ultrahigh-speed digital interconnects," *IEEE Transactions on Microwave Theory and Techniques*, vol. 54, pp. 1983–1990, May 2006.

[58] R. Simons, *Coplanar Waveguide Circuits, Components, and Systems*. Wiley Series in Microwave and Optical Engineering, Wiley, 2004.

[59] R. Kazemi, R. Sadeghzadeh, and A. Fathy, "Design of a wide band eight-way compact SIW power combiner fed by a low loss GCPWTO-SIW transition," *Progress In Electromagnetics Research C*, vol. 26, 01 2012.

[60] Keysight Technologies, *Specifying Calibration Standards and Kits for Keysight Vector Network Analyzers*, 2016. Rev. 1.0.

[61] H. Frid and B. L. G. Jonsson, "Determining Installation Errors for DOA Estimation with Four-Quadrant Monopulse Arrays by Using Installed Element Patterns," in *2018 2nd URSI Atlantic Radio Science Meeting (AT-RASC)*, pp. 1–4, May 2018.

[62] B. T. P. Madhav and T. Anilkumar, "Design and study of multiband planar wheel-like fractal antenna for vehicular communication applications," *Microwave and Optical Technology Letters*, vol. 60, no. 8, pp. 1985–1993, 2018.

[63] M. G. N. Alsath and M. Kanagasabai, "Compact UWB Monopole Antenna for Automotive Communications," *IEEE Transactions on Antennas and Propagation*, vol. 63, pp. 4204–4208, Sep. 2015.

[64] Z. Liu and C. Wang, "An efficient iterative MoM-PO hybrid method for analysis of an onboard wire antenna array on a large-scale platform above an infinite ground," *IEEE Antennas and Propagation Magazine*, vol. 55, pp. 69–78, Dec 2013.

[65] T. Nagatsuma, G. Ducournau, and C. C. Renaud, "Advances in terahertz communications accelerated by photonics," *Nature Photonics*, vol. 10, no. 6, p. 371, 2016.

[66] J. A. Hejase, P. R. Paladhi, and P. P. Chahal, "Terahertz Characterization of Dielectric Substrates for Component Design and Nondestructive Evaluation of Packages," *IEEE Transactions on Components, Packaging and Manufacturing Technology*, vol. 1, pp. 1685–1694, Nov 2011.

[67] E. R. Brown, C. D. Parker, and E. Yablonovitch, "Radiation properties of a planar antenna on a photonic-crystal substrate," *J. Opt. Soc. Am. B*, vol. 10, pp. 404–407, Feb 1993.

[68] S. H. Choi, M. Kim, K. J. Lee, and J. S. You, "A terahertz wire-array antenna integrated on a 75 um InP substrate," in *2015 IEEE International Symposium on Antennas and Propagation USNC/URSI National Radio Science Meeting*, pp. 2103–2104, July 2015.

[69] K. M. Lee, I. J. Lee, S. Jeon, M. Kim, and J. S. You, "300 GHz InP rectangular cavity antenna," in *2015 IEEE International Symposium on Antennas and Propagation USNC/URSI National Radio Science Meeting*, pp. 2105–2106, July 2015.

[70] M. Kim, S. H. Choi, S. Jeon, and I. J. Lee, "A 280-GHz Rectangular Cavity Antenna Integrated in 80um InP Substrate," *IEEE Antennas and Wireless Propagation Letters*, vol. PP, no. 99, pp. 1–1, 2016.

[71] K. H. Alharbi, A. Khalid, A. Ofiare, J. Wang, and E. Wasige, "Broadband bow-tie slot antenna with tuning stub for resonant tunnelling diode oscillators with novel configuration for substrate effects suppression," in *2016 46th European Microwave Conference (EuMC)*, pp. 421–424, Oct 2016.

[72] S. Honda, M. Ito, H. Seki, and Y. Jinbo, "A disk monopole antenna with 1:8 impedance bandwidth and omnidirectional radiation pattern," in *Proceedings of the International Symposium on Antennas and Propagation Japan*, vol. 4, pp. 1145–1145, Citeseer, 1992.

[73] Q. Wu, R. Jin, J. Geng, and M. Ding, "Compact CPW-fed quasi-circular monopole with very wide bandwidth," *Electronics Letters*, vol. 43, pp. 69–70, January 2007.

[74] Y. T. Li, J. W. Shi, C. Y. Huang, N. W. Chen, S. H. Chen, J. I. Chyi, Y. C. Wang, C. S. Yang, and C. L. Pan, "Characterization and Comparison of GaAs/AlGaAs Uni-Traveling Carrier and Separated-Transport-Recombination Photodiode Based High-Power Sub-THz Photonic Transmitters," *IEEE Journal of Quantum Electronics*, vol. 46, pp. 19–27, Jan 2010.

[75] J. F. Johansson, "A Comparison of Some Feed Types," in *Astronomical Society of the Pacific Conference Series*, vol. 75, pp. 82–89, May 1994.

[76] R. J. Wylde, "Millimetre-wave Gaussian beam-mode optics and corrugated feed horns," *IEE Proceedings H - Microwaves, Optics and Antennas*, vol. 131, pp. 258–262, August 1984.

[77] J. E. McKay, D. A. Robertson, P. J. Speirs, R. I. Hunter, R. J. Wylde, and G. M. Smith, "Compact Corrugated Feedhorns With High Gaussian Coupling Efficiency and−60 dB Sidelobes," *IEEE Transactions on Antennas and Propagation*, vol. 64, pp. 2518–2522, June 2016.

[78] D. McCarthy, J. A. M. Neil Trappe, C. O'Sullivan, M. Gradziel, S. Doherty, C. Bracken, N. Tynan, A. Polegre, and P. Huggard, "Efficient algorithms for optimising the optical performance of profiled smooth walled horns for future CMB and Far-IR missions," vol. 9153, pp. 9153 – 9153 – 8, 2014.

[79] J. F. Johansson and N. D. Whyborn, "The diagonal horn as a sub-millimeter wave antenna," *IEEE Transactions on Microwave Theory and Techniques*, vol. 40, pp. 795–800, May 1992.

[80] Q. Xu, Y. Huang, X. Zhu, L. Xing, P. Duxbury, and J. Noonan, "A Hybrid FEM-GO Approach to Simulate the NSA in an Anechoic Chamber," *Applied Computational Electromagnetics Society Journal*, vol. 32, no. 11, pp. 1035–1041, 2017.

[81] D. Cheng, *Field and wave electromagnetics*. The Addison-Wesley series in electrical engineering.

[82] P. Y. Ufimtsev, *Fundamentals of the physical theory of diffraction*. Wiley-Interscience, 2007.

[83] W. Emerson, "Electromagnetic wave absorbers and anechoic chambers through the years," *IEEE Transactions on Antennas and Propagation*, vol. 21, no. 4, pp. 484–490, 1973.

[84] M. C. Decreton and F. E. Gardiol, "Simple Nondestructive Method for the Measurement of Complex Permittivity," *IEEE Transactions on Instrumentation and Measurement*, vol. 23, pp. 434–438, Dec 1974.

[85] S. I. Ganchev, S. Bakhtiari, and R. Zoughi, "A novel numerical technique for dielectric measurement of generally lossy dielectrics," *IEEE Transactions on Instrumentation and Measurement*, vol. 41, pp. 361–365, June 1992.

[86] K. J. Bois, A. D. Benally, and R. Zoughi, “Multimode solution for the reflection properties of an open-ended rectangular waveguide radiating into a dielectric half-space: the forward and inverse problems,” *IEEE Transactions on Instrumentation and Measurement*, vol. 48, pp. 1131–1140, Dec 1999.

[87] Niu Maode, Su Yong, Yan Jinkui, Fu Chenpeng, and Xu Deming, “An improved open-ended waveguide measurement technique on parameters ε_r and μ_r of high-loss materials,” *IEEE Transactions on Instrumentation and Measurement*, vol. 47, pp. 476–481, April 1998.

[88] Virginia Diodes, Inc, *VDI Precision Waveguide Interface*, 2014. Rev. 2.7.

[89] J. Hollis and T. Lyon, *Microwave Antenna Measurements*. Scientific-Atlanta, 1972.

[90] N. M. A. Chowdhury, S. Hossain, and and, “Low cost indoor environment for antenna measurement,” in *2008 Canadian Conference on Electrical and Computer Engineering*, pp. 001353–001356, May 2008.

[91] D. Campbell, G. Gampala, C. Reddy, M. Winebrand, and J. Aubin, “Modeling and Analysis of Anechoic Chamber Using CEM Tools,” *Applied Computational Electromagnetics Society Journal*, vol. 28, no. 9, 2013.

[92] SAGE Millimeter, Inc, *WR-10 Pyramidal Horn Antenna, 20 dBi Gain*, 2016. Rev. 1.0.

[93] SAGE Millimeter, Inc, *WR-10 Pyramidal Horn Antenna, 25 dBi Gain* , 2016. Rev. 1.0.